Wetting in Porous Media: A Nuclear Magnetic Resonance Study.

Henrik Nicolay Sørgård

Thesis for the degree of Philosophiae Doctor (PhD)
University of Bergen, Norway
2020

UNIVERSITY OF BERGEN

Wetting in Porous Media: A Nuclear Magnetic Resonance Study.

Henrik Nicolay Sørgård

Thesis for the degree of Philosophiae Doctor (PhD)
at the University of Bergen

Date of defense: 30.06.2020

Year: 2020

Title: Wetting in Porous Media: A Nuclear Magnetic Resonance Study.

Name: Henrik Nicolay Sørgård

Print: Skipnes Kommunikasjon / University of Bergen

Preface

This thesis is submitted, to the Department of Chemistry at the University of Bergen, as part of the requirements for the degree of Philosophiae Doctor. The research presented in papers 1-4, was conducted at the National NMR platform (NNP) facilities at the University of Bergen in the time period 2016-2019. The project was supervised by Associate Professor John Georg Seland (main supervisor), Professor Willy Nerdal (co-supervisor) and Professor 2 Per Fotland (co-supervisor).

The research presented here is part of a larger research project named "Wetting in porous media, a multi method approach to measurement, imaging and modelling". The main focus in papers 1-4 has been to study mechanisms responsible for wettability alteration on reservoir minerals and then to study how surface wettability affects the distribution of immiscible fluids in porous media. Nuclear Magnetic Resonance (NMR) has been the main analytical tool.

The thesis consists of two parts. Chapters 1-5 contains an introduction to the field, the theoretical concepts behind the research, the applied methods and materials, the main results and the conclusions drawn from this work. The second part contains the research papers that were published as a result of the work presented in this thesis. Papers 1-4 can be found after the bibliography.

Acknowledgements

I would like to acknowledge the excellent guidance provided by John Georg Seland. His teachings, his patience and in general his supervision has been second to none. I would also like to thank my co-supervisors Willy Nerdal and Per Fotland for their professional input when needed. When I started this project I had never operated an NMR spectrometer. I would therefore like to thank the rest of the NMR group at the Department of Chemistry as well (Nils Åge, Josè, Jarl, Olav and Christian) for including me and for advices along the way. I would like to give a special thank you to Christian for the way he taught me how to operate the spectrometers.

The Department of Chemistry at the University of Bergen will always be a special place for me. Yes, it was the place i went to school for nearly a decade, but it was also the place where i met my fiancè. I was sitting in that office both when I was told that the bid on our first house was accepted and I was sitting there when Sarah Marie called to tell me that i had to come home because it was time to go to Haukeland to meet our son.

My dearest Sarah Marie, the finishing touches on this thesis has been applied during weekends and during the late hours of the night, which I know has put extra responsibility on you. Thank you so much for your continued support and patience throughout this entire process. This would have been impossible without you.

My dearest Eiliv, you are currently too young to realize that I have been working when I should have been with you. I promise that will change now. This is for you.

List of papers

1. H. N. Sørgård, C. Totland, W. Nerdal and J. G. Seland, *Crude oil adsorbates on calcite and quartz surfaces investigated by NMR spectroscopy*, The Journal of Physical Chemistry C, **121**, 38, (2017), 20892-20899.

2. H. N. Sørgård, C. Totland, W. Nerdal and J. G. Seland, *Investigating mobility of crude oil adsorbates on mineral surfaces by NMR*, Magnetic Resonance Imaging, **56**, (2019), 86-89.

3. H. N. Sørgård and J. G. Seland, *Investigating pore geometry in heterogeneous porous samples using spatially resolved* $G_0-\Delta\chi_{app}$ *and* $G_0-\Delta\nu$ *correlations*, Journal of Magnetic Resonance, **301**, (2019), 40-48.

4. H. N. Sørgård and J. G. Seland, *A fluid specific dimension of confinement as a measure of wettability in porous media*, Journal of Magnetic Resonance, **310**, (2020), 106663.

Nomenclature

This section provides explanations for the various abbreviations, units and symbols used throughout this thesis.

Abbreviations

2D	Two dimensional
3D	Three dimensional
BW	Bandwidth
CA	Contact angle
CPMG	Carr-Purcell-Meiboom-Gill
DDIF	Decay due to diffusion in the internal field
DOC	Dimension of confinement
DQSQ	Double-quantum-single-quantum
DW	Dwell time
EOR	Enhanced oil recovery
eq	Equilibrium
FD	Free diffusion
FID	Free induction decay
FOV	Field of view
FT	Fourier transform
FTIR	Fourier transform infrared spectroscopy
IR	Inversion recovery
LOC	Localization
MAS	Magic angle spinning
MAV	Motional averaging
MR	Magnetic resonance
MRI	Magnetic resonance imaging
NMR	Nuclear magnetic resonance

PFG	Pulsed field gradient
PFGSE	Pulsed field gradient spin echo
RARE	Rapid acquisition with relaxation enhancement
RF	Radio frequency
SD	Standard bore
SEM	Scanning electron microscopy
TAN	Total acid number
TGA	Thermo gravimetric analysis
TMCS	Trimethylchlorosilane
USMB	United States bureau of mines
WB	Wide bore
ZP	Zeta potential

Units

cm	Centimeter
Hz	Hertz
h	Hour
J	Joule
K	Kelvin
KHz	Kilohertz
m	Meter
μm	Micrometer
μs	Microsecond
ml	Millimeter
ms	Millisecond
ppm	Parts per million
rad	Radian
s	Second
T	Tesla

Symbols

θ	Angle of rotation
ω	Angular frequency
P	Angular momentum
$\Delta\chi_{app}$	Apparent magnetic susceptibility difference
$T_{2,app}$	Apparent transverse relaxation time
B_1	Applied magnetic field
Z_0	Center of the slice position
δ	Chemical shift
τ_c	Correlation time
d_1	Delay time
l_g	Dephasing length
D	Diffusion coefficient
l_D	Diffusion length
b	Diffusion term
Δ	Diffusion time
E	Echo intensity
t_E	Echo time
B_{eff}	Effective magnetic field
e	Eulers number
B_0	External magnetic field
T_2^*	Free induction decay time constant
S_i	Fluid specific saturation
V_i	Fluid specific volume
ν	Frequency
Ω_i	Frequency offset
B_{grad}	Gradient magnetic field
G	Gradient intensity
L_G	Gradient duration
γ	Gyromagnetic ratio
h	Planck's constant
$\hbar$	Plank's constant/2π
$S_{w,i}$	Immobile water saturation
k	k-space value
M_z	Longitudinal Magnetization
T_1	Longitudinal relaxation time
θ_{MA}	Magic angle

μ	Magnetic moment
$\Delta\chi$	Magnetic susceptibility difference
G_0	Magnetic susceptibility induced internal gradient
M	Net magnetization
N_i	Number of echo points
a	Pore size
V_p	Pore volume
ϕ	Porosity
^1H	Proton
L_P	Pulse length
ν_{ref}	Reference frequency
$S_{o,r}$	Residual oil saturation
x'	X-axis in the rotating frame
y'	Y-axis in the rotating frame
V_s	Sample volume
C	Scalar determined by initial spin ensemble
σ	Shielding constant
S	Signal amplitude
Δz	Slice thickness
Δf	Spectral frequency offset intervals
$\Delta\nu$	Spectral half width
I	Spin quantum number
l_s	Structural length
ρ	Surface relaxivity
S/V	Surface to volume ratio
t	Time
M_{xy}	Transverse magnetization
T_2	Transverse relaxation time
v_d	Variable delay
V	Volume

Contents

Preface i

Acknowledgements ii

List of papers iii

Nomenclature iv
Abbreviations . . . iv
Units . . . v
Symbols . . . vi

1 Introduction 1
1.1 Background . . . 2
1.2 Objectives . . . 7
1.3 Outline . . . 8
1.3.1 Paper 1 . . . 8
1.3.2 Paper 2 . . . 8
1.3.3 Paper 3 . . . 8
1.3.4 Paper 4 . . . 9

2 Theory 10
2.1 Petrophysical/chemical properties . . . 11
2.1.1 Porosity . . . 11
2.1.2 Saturation . . . 11
2.1.3 Wettability . . . 12
2.1.4 Wettability alteration . . . 13
2.2 Nuclear Magnetic Resonance (NMR) . . . 14
2.2.1 Fundamental NMR theory . . . 14

2.2.2 Solid state NMR and Magic Angle Spinning (MAS) . . 24
2.2.3 Magnetic Resonance Imaging (MRI) 26
2.2.4 Self-diffusion 33
2.2.5 Internal magnetic field gradients 35

3 Methods and materials 39
3.1 Materials 40
3.2 Sample preparation 41
3.2.1 Powder samples for solid state MAS NMR 41
3.2.2 Liquid state NMR samples 42
3.2.3 Porous liquid saturated samples for MRI 42
3.2.4 Model core samples 43
3.3 Displacement experiments 44
3.4 Hardware 45
3.5 NMR pulse sequences 46
3.5.1 Pulse-acquire 46
3.5.2 ^{1}H-^{1}H double-quantum single-quantum 47
3.5.3 Inversion Recovery 47
3.5.4 The spin echo and CPMG 48
3.5.5 IR-CPMG 49
3.5.6 PFGSE 49
3.5.7 Modified CPMG 50
3.5.8 Spin echo in MRI 52

4 Results and discussion 53
4.1 Molecular level investigations 54
4.1.1 Assignment of adsorbed species 54
4.1.2 Mobility of adsorbed species 56
4.2 Pore scale investigations 61
4.2.1 Pore sizes from G_0-$\Delta\chi_{app}$ correlations 62
4.2.2 The dimension of confinement 66

5 Concluding remarks 71
5.1 Conclusions 72
5.2 Suggestions for future research 73

Bibliography 74

Chapter 1

Introduction

This chapter provides a brief introduction into previous work performed in the field of wettability characterization by NMR as well as the objective and outline of this study.

1.1 Background

Porous media are ubiquitous in nature and are encountered in numerous industrial avenues including construction materials, chemical reactors and underground reservoirs containing water, oil and gas [1]. The behaviour of fluids in porous media is a very complicated topic. However, because of the wide variety of applications and the economic incentives associated with oil and gas, fluid behaviour in porous media has been a tremendously important field of research throughout the entire 20th century and continues to be so.

Wettability is defined as the relative preference of a surface to be covered by one of several immiscible fluids [2, 3, 4]. Fluid distribution of oil and water in a petroleum reservoir is therefore largely dependent of the wettability of the reservoir rock surface. This makes wettability one of the most important reservoir properties one must consider when designing a production strategy [3, 5].

Petroleum reservoirs are created when oil migrates from a source rock and is captured by a layer of impenetrable cap rock, thus draining water from the reservoir rock. This process is called primary drainage [6, 7]. As the reservoir rock was 100% water saturated prior to primary drainage, reservoir rock is presumed to be originally water-wet. However, some reservoirs are found to be oil-wet. It is generally accepted that adsorption of polar components from crude oil onto reservoir surfaces is part of the mechanism responsible for the naturally occuring change in wettability from water-wet to oil-wet [6, 8, 9, 10].

Investigations into the mechanisms responsible for changes in wetting state has typically involved Thermo Gravimetric Analysis (TGA), Contact Angle (CA) measurements and Fourier Transform Infrared (FTIR) spectroscopy. Adsorption of different acids from acid/decane crude oil models onto the positively charged calcite surfaces has been investigated by several authors. Gomari et al. investigated adsorption of fatty acids onto calcite with TGA [11] and CA measurements [12]. Wu et al. [13] investigated ageing of calcite by a model oil containing several different naphtenic acids in decane by CA and simple floatation tests. Jarrahian et al. [14] used TGA, CA and FTIR to investigate the efficiency of surfactant induced desorption of stearic acid from calcite for enhanced oil recovery (EOR) purposes in carbonates.

The effect of ion concentration in the water during adsorption/desorption of species on calcite surfaces have also been studied using Zeta Potential (ZP) measurements. Karimi et al. [15] investigated the effect of Mg^{2+} ions in the

presence and absence of cationic surfactants. Gomari et al. [16] investigated the effect of sulfate ions on the calcite ZP.

Determining the wettability in unknown samples of reservoir rock has historically, typically been determined from laboratory experiments performed on core samples from the reservoir of interest. These laboratory experiments usually involve spontaneous and forced displacement of one fluid by another. The Amott-test [2] and the USBM wettability method [4] are examples of procedures for determining wettability based on such displacement experiments.

Nuclear Magnetic Resonance (NMR) was discovered in 1946 by two independent research groups [17, 18]. Within ten years of its discovery, NMR was implemented into petrophysical laboratory investigations [19]. Since then NMR has become an integral part of laboratory petrophysical core analysis as well as in oilfield exploration in the form of NMR well-logging [1, 20, 21].

NMR is a vast field of research in itself and can be used to investigate mechanisms responsible for different wetting states as well as for determining wettability in unknown samples. Although, most wettability studies involving NMR focuses on method development toward determining wettability in samples with an unknown wetting state.

Spectroscopic methods, that are sensitive to local environments, are needed to provide structural information regarding adsorbed species. NMR is sensitive to local environments and high resolution solid state NMR can be a valuable probing tool into the chemical structure of surface species [22, 23].

Totland and Lewis [24] used solid state NMR to investigate the effect of water on the efficiency of stearic acid adsorption onto calcite and the efficiency of surfactant induced desorption of stearic acid from calcite. Their results revealed that adsorption increased by up to 100% when the calcite surface was wetted prior to contact with oil, compared to when the calcite was dry. The idea behind solid state NMR analysis of calcite particles before and after ageing in model oil and then again after desorption by surfactant addition was that relaxation times from different parts of the adsorbed species will correlate to mobility.

The first wettability study using NMR was performed by Brown and Fatt [19] in 1956. They reported a linear correlation between the longitudinal (T_1) relaxation time of water and the fraction of oil-wet sand in water saturated sand packings. Thus showing that the T_1 relaxation time of water is dependent on the wettability of the surrounding porous matrix. A linear relationship between T_1 relaxation time and fractional wettability in glass

bead systems was also found by Kumar et al. [25], Williams and Fung [26] and by Hsu et al. [27].

The wettability of a porous media determines how immiscible fluids are distributed in a pore and in the pore network. The idea of using NMR relaxation as a measure of wettability is based on the fact that both T_1 and T_2 relaxation times are affected by surface relaxation, i.e. volumes adjacent to surfaces experience enhanced relaxation. In porous samples saturated with two immiscible fluids such as oil and water, relaxation time distributions [28] can give indirect indications of wetting and non wetting fluid. In water-wet samples, water will mainly be present along pore surfaces and in small pores etc.

Howard [29] showed that the core saturation determined from the area under T_1 distributions in chalk correlated very well with results from established laboratory methods. He also proposed a wettability index [30] that correlated very good with the Ammot method.

NMR analysis of fluid saturated porous media does have its challenges due to the difference in magnetic susceptibility between the matrix and the fluid(s) occupying the pore space. Such differences in magnetic susceptibility induces internal magnetic field gradients [31]. Although T_1 and T_2 relaxation both are affected by surface relaxivity, only T_2 is affected by diffusion in the internal field. The strength of the internal gradient is proportional to the external magnetic field strength exhibited by the NMR spectrometer. Most relaxation measurements, and especially T_2 measurements have therefore been performed with low external magnetic field strengths.

Freedman et al. [32] demonstrated significant surface relaxation in mixed wet dolomite samples compared to water-wet sandstone samples. The oil surface relaxation was demonstrated through diffusion free T_2 distributions, where the distributions from the mixed wet samples included values that were significantly lower than what was determined in the water-wet samples.

Looyestijn and Hofman [33] generated a quantitative wettability index based on T_2 relaxation measurements that demonstrate a good correlation with the USBM method and is effective at all saturations.

Valori et al. [34] found that the T_1-T_2 ratio of the oil phase in samples containing water and oil, strongly correlate with the wettability of the samples. This method is applicable for downhole measurements as well as laboratory measurements. Separating the oil and water signal in the downhole application is challenging though. This problem was solved by separating the oil and water signal by 2D diffusivity and the results were then compared to the

distributions containing signal from both oil and water.

Wang et al. [35] introduced a multidimensional NMR method to characterize the heterogeneous wettability that may be present in porous media. The method was validated with computer simulations. With this method, Wang and co-workers used the concept of apparent contact angles to obtain indications of heterogeneity before the T_1-T_2 ratio and T_2-D correlations was used to probe local wettability.

A similar approach was taken by Liang et al. [36] who recently used the T_1-T_2 ratio in combination with T_2-D correlations to determine wettability in rocks and tight sands. Their T_2 component was recorded using a bipolar pulse field gradient (PFG) sequence with a Carr-Purcell-Meiboom-Gill (CPMG) acquisition to suppress the effect of the internal gradient.

Although the internal gradient may be a nuisance, it also correlates quite conveniently to the pore geometry, given a certain diffusion regime [31]. Several authors have used internal gradient based correlations to probe pore geometry. Sun and Dunn [37] investigated the pore geometry of fluid saturated porous samples through DG_0^2-T_2 correlations by adding a CPMG train to a modified version of the CPMG [38, 39] sequence. In the modified CPMG sequence, the signal attenuation is weighted by the internal gradient and the diffusion coefficient (DG_0^2) and they combined this with the T_2 weighting present in the original CPMG experiment.

Seland et al. [40] investigated the effect of surface wettability on G_0-T_2 and D-T_2 correlation maps acquired from fluid saturated glass bead packings. They separated the oil and water signal based on diffusivity. G_0-T_2 correlations were obtained from a D-G_0-T_2 pulse sequence. They found that wettability predominately effects the fast diffusing water molecules. Wettability could thus be determined based on the location of the water signal in the 2D correlation maps.

Zhang and Blümich [41] extended the G_0-T_2 method to include spatial resolution by frequency encoding on the CPMG train. By doing so they were able to distinguish between oil and water in different parts of glass bead samples.

Bratland et al. [42] characterized oil and water in a sand stone core sample using G_0-T_2 correlations. Their results were compared to results from the D-T_2 method and showed that the G_0-T_2 method better reveals how the impact from heterogeneity in pore geometry affects the individual liquids than the D-T_2 method.

Song [43] proposed the Decay due to Diffusion in the Internal Field (DDIF) method which is based on the diffusive properties on pore fluids under the influence of an external magnetic field. The DDIF method is based on a stimulated echo and provides pore size distributions in fluid saturated porous samples independent from surface relaxation. Liu et al. [44] extended the DDIF method to include a CPMG acquisition (DDIF-CPMG), thus creating a pore size - T_2 correlation experiment. The DDIF-CPMG method was applied to various porous samples saturated with oil and water by Lewis et al. [45]. They found that the DDIF section of the pulse sequence filters out the oil signal and that one can thus study the pore geometry from the water signal. Zhang et al. [46] later extended the DDIF-CPMG method by including spatial resolution through frequency encoding in the CPMG train.

In papers 1 [47] and 2 [48] presented in this thesis, high field solid state NMR was applied to powder samples in order to investigate how crude oil adsorbates attach to different mineral surfaces. High magnetic field strength allowed for increased spectral resolution, which in turn allowed for identification of different functional groups in the molecules.

In papers 3 [49] and 4 [50] presented in this thesis, spatially resolved correlations between the internal gradient and differences in magnetic susceptibility were used to calculate pore size distributions and fluid specific dimension of confinement distributions. The difference in magnetic susceptibility was calculated from the FID [51, 49] and from the spectral peak half width [52, 50], therefore spatial resolution was achieved by slice selection and not by frequency encoding. High magnetic field strength allowed sufficient chemical shift separation between oil and water.

1.2 Objectives

The work presented in this thesis is part of a larger research project named "Wetting in porous media, a multi method approach to measurement, imaging and modelling". The overall objective of this project is to investigate links between wetting properties on the molecular scale and reservoir scale flow response. The objective of this research was twofold.

1. The first two papers were meant to provide new insights into the mechanisms responsible for the naturally occurring change in wetting state that occurs during wet crude oil ageing. The main analytical tool was high field/high resolution solid state Magic Angle Spinning (MAS) NMR. Properties to investigate were chemical shift, relaxation times and diffusion measurements. Lessons learned in the work that lead to these two paper were to be implemented in the next phase.

2. The objective of papers 3 and 4 was to investigate the effect of wettability on the distribution of immiscible fluids in the pore space. Therefore a model system were to be created for NMR investigations on the pore and core sample sample scale during displacement experiments. Magnetic Resonance Imaging (MRI) techniques were to be implemented and properties to be investigated were relaxation times and internal magnetic field gradient measurements, as they both relate to pore geometry [1]. MRI techniques allow for spatial resolution which will enable investigations in and around displacement fronts. Such investigations will provide new insights into how displacing and displaced fluids behave in the pore network during displacement experiments.

1.3 Outline

This section provides highlights from the publications that resulted from the work presented in this thesis.

1.3.1 Paper 1

In paper 1, wet crude oil ageing of calcite and quartz particles was investigated with high resolution NMR. Investigated properties of adsorbed species were chemical shifts (δ), ^{1}H-^{1}H correlations, T_1 and T_2 relaxation times and spectral signal amplitude as a function of temperature.

Electrostatic adsorption of organic acids was determined on the calcite surface but not on the quartz surface. Methylsilane groups were identified on the quartz surface. Solid state NMR was found to be a useful analytical tool in the analysis of adsorbed species.

1.3.2 Paper 2

In paper 1, wet crude oil ageing of calcite and quartz particles was investigated with high resolution NMR. Investigated properties of adsorbed species were self diffusion coefficients (D), T_1-T_2 ratios and spectral signal amplitude as a function of diffusion weighting.

The samples investigated in this paper were the same as in paper 1 and the interpretations from paper 2 correlated well with the ones from paper 1.

1.3.3 Paper 3

Paper 3 demonstrates proof of concept for spatially resolved pore size distributions based on correlations between magnetic susceptibility induced internal gradients (G_0) and the difference in the apparent magnetic susceptibility ($\Delta\chi_{app}$) in water saturated porous media. G_0 distributions are also presented as a function of spectral frequency (Hz) intervals to indicate the heterogeneity of the pore space.

Spatially resolved pore size distributions show good correlations to previous methods and the heterogeneity indications show good correlation with previous computer simulations.

1.3.4 Paper 4

In paper 4 the pulse sequence developed in paper 3, was applied during displacement experiments in a more realistic model system where oil and water was present in the same pore network at the same time. The result from this application was fluid specific Dimension of Confinement (DOC) distributions (spatially resolved and non- spatially resolved). As there are two NMR active fluids under these experiments the data processing differs from the one used in paper 3. The DOC distributions were calculated from the same correlations as the pore size distributions in paper 3 (G_0-$\Delta\chi_{app}$) however, the calculations in paper 4 were fluid specific.

Fluid specific and spatially resolved DOC distributions recorded in and around displacement fronts can indicate the wetting state of an unknown quartz sand sample. Fluid specific and non spatially resolved DOC distributions can indicate the wetting state in unknown quartz sand samples at immobile water saturation and at residual oil saturation.

Chapter 2

Theory

This chapter outlines the theoretical concepts that make up the foundation for the research performed in this thesis.

2.1 Petrophysical/chemical properties

This section describes the petrophysical and petrochemical properties considered in this thesis.

2.1.1 Porosity

The porosity (ϕ) of a porous medium is the medium's fluid storage capacity. The porosity is defined as

$$\phi = \frac{V_p}{V_s} \tag{2.1}$$

where V_p is the pore volume and V_s is the sample volume. ϕ is dependent on grain size and packing [53].

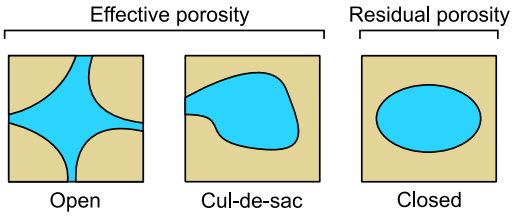

Figure 2.1: Schematic of different types of porosity. Effective porosity is the sum of the open and the cul-de-sac pores while the residual porosity comes from the closed pores. Figure inspired by Selley [54].

2.1.2 Saturation

Several immiscible fluids may be present in the same pore space. The fluid specific saturation (S_i) is defined as

$$S_i = \frac{V_i}{V_p} \tag{2.2}$$

where V_i is the volume of a specific fluid and V_p is the pore volume [53].

2.1.3 Wettability

The wettability of a surface is described by its relative preference to be covered by one of several immiscible fluids [2, 6, 7, 33]. In this thesis, the immiscible fluids of interest are oil and water.

The wetting conditions of the reservoir rock surface is one of the most important factors influencing the efficiency of oil recovery. Correctly understanding the wetting conditions of a reservoir at an early stage is therefore of tremendous importance with regards to options for field-development. Incorrect estimations of wetting conditions may result in unexpected dynamic behaviour, incorrect oil-in-place estimates and thus an incorrect economic valuation of the reservoir [33]. It is generally accepted that secondary oil recovery (water floods) is more efficient in water-wet reservoirs i.e. where water is the wetting phase and oil is located in the middle of the pores [2, 6, 7, 55, 53].

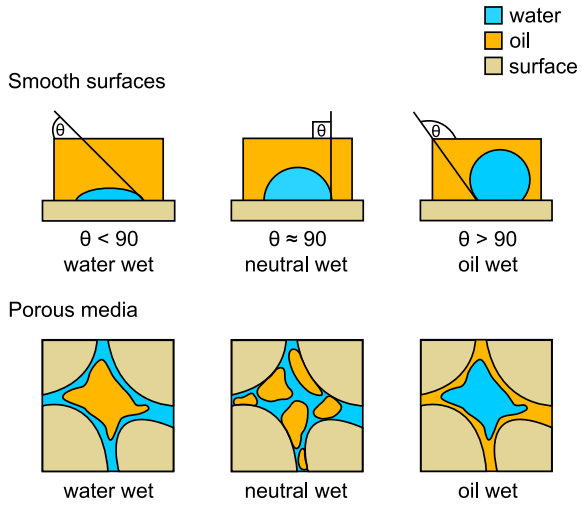

Figure 2.2: Schematic showing how the contact angle on a smooth surface of a given material affects the fluid distribution in a pore of the same material.

Wettability on flat surfaces is usually determined with contact angle measurements, where the angle created between the drop and the surface through

the densest phase determines the wettability of the surface [6]. A contact angle below 90° constitutes water-wet and a contact angle above 90° constitutes oil-wet as shown in Figure 2.2. Note that surfaces with contact angles in the vicinity of 90° can be considered neutral-wet [6, 7].

2.1.4 Wettability alteration

Oil-wet reservoirs is a result of polar components from crude oil adsorbing to the reservoir surface [6, 7, 10]. During the the creation of a petroleum reservoir, oil migrates from the source rock to the reservoir rock where it is trapped by a layer of impenetrable cap rock. This process is called the primary drainage [53]. Therefore, all reservoir rock is originally water-wet and the wettability alteration happens during and after primary drainage as the reservoir surface is gradually exposed to the crude oil [8, 9, 10, 56].

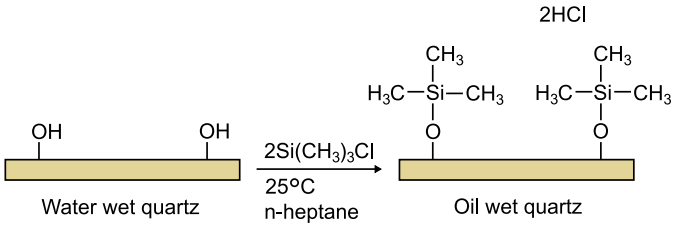

Figure 2.3: Wettability alteration of a quartz surface through a silanization process by using a trimethylclorosilane in heptane solution at ambient temperature.

An example of chemically induced wettability alteration is shown in Figure 2.3. A pure quartz surface (originally water-wet) is made oil-wet by exposing the quartz surface to a solution of trimethylclorosilane in heptane. During this process, trimetylsilane-groups adsorb to the OH-sites on the quartz surface, which alters the surface from hydrophilic to hydrophobic.

In this thesis the mechanism responsible for naturally occurring wettability alteration of minerals by crude oil is investigated on a molecular level in papers 1 and 2. The work presented in paper 4 shows new magnetic resonance imaging techniques suitable for determining wettability in model core samples.

2.2 Nuclear Magnetic Resonance (NMR)

Nuclear Magnetic Resonance (NMR) was discovered in 1946 [17, 18]. Since then, the applications of this phenomenon has contributed to advancement of tremendous importance within chemistry, diagnostic medicine and other industrial avenues. NMR is the main analytical method used in the research presented in this thesis.

2.2.1 Fundamental NMR theory

Nuclei with an odd number of protons and or neutrons will spin around their own axis causing them to possess spin angular momentum (P).

$$P = \sqrt{I(I+1)}\hbar \tag{2.3}$$

where I is the spin quantum number and $\hbar = h/2\pi$ where h is Planck's constant ($h = 6.6256 \cdot 10^{-34} Js$). The spin angular momentum is proportional to the magnetic moment (μ)

$$\mu = \gamma P \tag{2.4}$$

where γ is the gyromagnetic ratio of the nuclei [57, 58]. From Equation 2.3 and 2.4 it follows that

$$\mu = \gamma\sqrt{I(I+1)}\hbar \tag{2.5}$$

which shows that nuclei with spin quantum number $I = 0$ has no magnetic moment and cannot be detected using NMR spectroscopy. A single magnetic moment is depicted in Figure 2.4 A. If a macroscopic sample containing nuclei with spin quantum number $I \neq 0$ experience no external disturbance (i.e. no external magnetic field) the magnetic moments will orient themselves in random directions and thus cancel each other as shown in Figure 2.4 B [57, 59, 60].

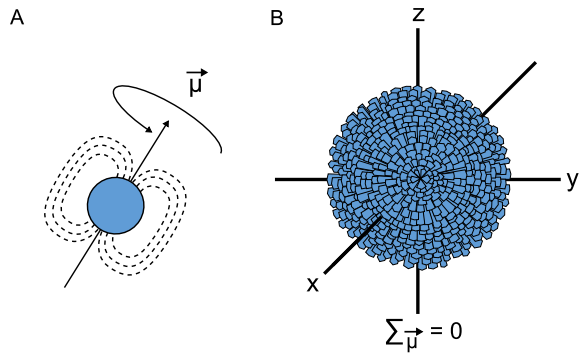

Figure 2.4: Nucleus with spin angular momentum expressed as a magnetic moment in the absence of an external magnetic field (A). Example showing how the nuclei in a macroscopic sample are randomly arranged in absence of an external magnetic field. Thus, their magnetic moments cancel each other and the resulting net magnetization is zero (B). Figure inspired by Hanson [59].

When a nucleus with spin $I \neq 0$ and a magnetic moment $\vec{\mu}$ experiences an external magnetic field ($\vec{B_0}$), $\vec{\mu}$ will precess around $\vec{B_0}$ with a frequency $\vec{\omega}$ (Figure 2.5 A). The time dependence of $\vec{\mu}$ is given by

$$\frac{d\vec{\mu}}{dt} = \vec{\mu} \times \gamma \vec{B_0} \tag{2.6}$$

where γ is the gyromagnetic ratio of the nucleus in question [59, 60]. When expressing the net magnetization in vector form one can express the vector movement in a coordinate system in two different ways. Equation 2.6 refers to the laboratory frame of reference, where the magnetic moment precesses in a stationary coordinate system.

In the rotating frame of reference however, the xy-plane of the coordinate system is rotating with a frequency $\vec{\omega}$ that makes the magnetic moment appear stationary [57, 58, 60]. In figures that represent the rotating frame of reference, the transverse axes are marked x' and y'. In the rotating frame of reference the time dependence of $\vec{\mu}$ is given by

$$\frac{d\vec{\mu}}{dt} = \vec{\mu} \times (\gamma \vec{B_0} + \vec{\omega}) \tag{2.7}$$

meaning that for the magnetic moment to appear stationary, the xy plane must rotate with a frequency $\vec{\omega} = -\gamma\vec{B}_0$. When $\vec{\omega} = -\gamma\vec{B}_0$, $\frac{d\mu}{dt}$ is constant and $\vec{\mu}$ is stationary [60].

$$\vec{\omega}_L = -\gamma\vec{B}_0 \tag{2.8}$$

This frequency is named the larmor frequency and it is also the frequency of which $\vec{\mu}$ is rotating with in the laboratory frame of reference. In this thesis the observed nucleus is ^{1}H ($\gamma = 267.522 \times 10^6\, rad\, s^{-1}\, T^{-1}$) and at 11.7 T the Larmor frequency of protons is approximately 500 MHz [61].

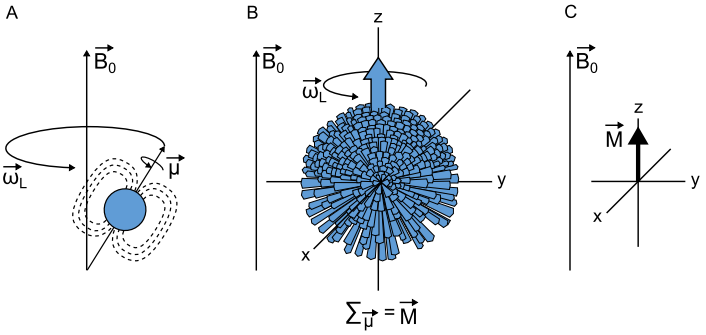

Figure 2.5: Schematic showing how nuclei with spin $I = 1/2$ in the presence of an external magnetic field will precess in an external magnetic field (A). Nuclei with positive γ have counter clockwise precession and vice versa. Schematic showing how the sum of the precessing nuclei in a macroscopic sample, in the presence of an external magnetic field, forms the net magnetization vector $\vec{M}$ (B). The net magnetization vector depicted alone (C). Figure inspired by Hanson [59].

As seen in Figure 2.4 B, the nuclei (magnetic moments) in a macroscopic sample are randomly oriented in the absence of an external magnetic field ($\vec{B}_0$). The thermal equilibrium of such a system represents no net magnetization ($\sum \vec{\mu} = 0$). I.e. if the magnetic moments are expressed as components in the x, y and z directions there is no surplus in any direction. As described above, the introduction of the external magnetic field ($\vec{B}_0$) causes precession around $\vec{B}_0$ (see Figure 2.5 A. In addition to precession, the introduction of $\vec{B}_0$

also affects the net magnetization. The net magnetization from all precessing magnetic moments are no longer zero ($\sum \vec{\mu} \neq 0$) [57, 58].

The thermal equilibrium state of a macroscopic sample in an external magnetic field does not disperse the precessing magnetic moments in random directions. In fact the distribution of precessing magnetic moments are slightly skewed towards magnetic north (Figure 2.5 B). This produces a longitudinal net magnetization $\vec{M}$. The creation of $\vec{M}$ is gradual and it is caused by longitudinal (T_1) relaxation [59], which will be explained below. The net magnetization ($\vec{M}$) is the starting point of all NMR experiments.

At thermal equilibrium the net magnetization is aligned parallel to $\vec{B}_0$ or the z-axis if a coordinate system is presented (see Figure 2.5 C). The net magnetization (M) is very small compared to the external magnetic field (B_0) and cannot be detected along the z-direction. To obtain a detectable signal, the thermal equilibrium must be disturbed so that the net magnetization is oriented into the xy-plane [57, 60].

Radio frequency (RF) pulses are used to generate xy-magnetization. Coherent rotation of the net magnetization into the xy-plane requires an additional oscillating magnetic field ($\vec{B}_1$) applied perpendicular to the external magnetic field ($\vec{B}_0$). $\vec{B}_1$ is the magnetic part of the RF-field and can be expressed as two vectors rotating with the Larmor frequency but in opposite directions (Figure 2.6). Only one of the two vectors are resonant and thus affecting the spin system, which one depends on the gyromagnetic ratio of the nuclei in question [60]. The blue vector is resonant if gamma is positive, while the red vector is resonant if gamma is negative.

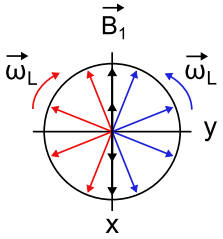

Figure 2.6: Oscillating $\vec{B}_1$ field along the x-axis expressed as two vectors rotating with the Larmor frequency, one in the clockwise direction (red) and one in the counter clockwise direction (blue).

A resonant B_1 field appears stationary in the rotating frame of reference and the time dependence of a single magnetic moment ($\vec{\mu}$) as well as the net magnetization ($\vec{M}$) can be expressed as

$$\frac{d\vec{\mu}}{dt} = \vec{\mu} \times \gamma\vec{B_1} \tag{2.9}$$

and

$$\frac{d\vec{M}}{dt} = \vec{M} \times \gamma\vec{B_1} \tag{2.10}$$

respectively [60]. In both instances it corresponds to a rotation of the vector in question about $\vec{B_1}$ with an angular frequency of $\vec{\omega_1} = \gamma\vec{B_1}$. The angle of rotation is given by

$$\theta = \gamma B_1 L_P \tag{2.11}$$

where L_P is the duration of the RF-pulse. The duration of a 180° pulse is twice as long as a 90° pulse of the same power [61].

Once the RF-pulse is turned off, the system reverts back towards thermal equilibrium. This process is known as relaxation and is governed by two different relaxation mechanisms described by the Bloch equations [62], where T_1 and T_2 are the longitudinal and transverse relaxation times respectively.

$$\frac{dM_{x'}}{dt} = -\frac{M_{x'}}{T_2} \tag{2.12}$$

$$\frac{dM_{y'}}{dt} = -\frac{M_{y'}}{T_2} \tag{2.13}$$

$$\frac{dM_z}{dt} = -\frac{M_0 - M_z}{T_1} \tag{2.14}$$

Transverse relaxation is the loss of polarization in the xy-plane that occurs once the RF-pulse is turned off (se Figure 2.7 A). The magnetization in the xy-plane (M_{xy}) can be defined as

$$M_{xy} = M_x + iM_y. \tag{2.15}$$

In liquid samples, loss of polarization in the xy-plane is caused by inter nuclei interactions and by inhomogeneities in the magnetic field (ΔB_0). Magnetic field inhomogeneities results in different Larmor frequencies across

the sample and will cause an additional decay term for the transverse magnetization [1].

$$\frac{1}{T_2*} = \frac{1}{T_2} + \gamma \Delta B_0 \tag{2.16}$$

T_2^* is the time constant of the signal decay in the xy-plane including contributions from both inter nuclei interactions and magnetic field inhomogeneities. T_2 is the time constant of the decay in $\vec{M}_{xy}$ caused solely by inter nuclei interactions.

When analysing liquid samples in modern high field spectrometers one can assume that $\Delta B_0 \approx 0$, meaning that $T_2 \approx T_2*$. When using permanent magnets at lower magnetic field strengths, this is not the case. However, the signal decay caused exclusively by inter nuclei interactions can still be recorded by implementing a Carr-Purcell-Meiboom-Gill (CPMG) pulse sequence [38, 39]. In the CPMG pulse sequence, the signal decay caused by magnetic field inhomogeneities is regenerated by 180° pulses creating an echo train. The signal loss from one echo to the next is then solely caused by inter nuclei interactions and the echo maxima decay can be expressed as

$$\frac{M_{xy}(t)}{M_{xy}(0)} = e^{-\frac{t}{T_2}}. \tag{2.17}$$

Once the B_1 field from the RF-pulse is turned off the polarization of the net magnetization begins to revert back towards magnetic north (along the z-axis parallel to B_0). This process is known as longitudinal (T_1) relaxation (see Figure 2.7 A) [57, 58, 60, 61]. In liquids, the recovery of $\vec{M}_z$ can be described as

$$\frac{M_z(t)}{M_z(eq)} = 1 - Ce^{-\frac{t}{T_1}}, \tag{2.18}$$

where $M_z(eq)$ is the net magnetization at thermal equilibrium and T_1 is the time constant of the the recovery process. C is a scalar determined by the starting conditions of the spin ensemble, i.e, the pulse sequence. All T_1 measurements in this thesis are recoded with inversion recovery sequences, where $C = 2$.

When analysing non-liquid samples, e.g., samples containing fluid filled porous media, relaxation in general and especially transverse relaxation becomes more complicated. In the case of transverse relaxation the apparent

transverse relaxation time ($T_{2,app}$) recorded with a CPMG acquisition, where the $\gamma\Delta B_0$ term is refocused, can be expressed as

$$\frac{1}{T_{2,app}} = \frac{1}{T_2} + \rho_2\frac{S}{V} + b \tag{2.19}$$

where ρ_2 is the surface relaxivity term associated with transverse relaxation, $\frac{S}{V}$ is the surface to volume ratio of the pores and b is the diffusion term [63]. The diffusion term b is introduced as a result of internal magnetic field gradients caused by the difference in magnetic susceptibility between the pore matrix and the fluid/fluids occupying the pore space. This is further discussed in section 2.2.4. The M_{xy} magnetization in porous samples as a function of time is given by the following expression.

$$\frac{M_{xy}(t)}{M_{xy}(0)} = e^{-(\frac{1}{T_{2,app}}+\rho_2\frac{S}{V}+b)} \tag{2.20}$$

Longitudinal relaxation is also affected by the surface relaxivity associated with porous samples but not by diffusion or $\gamma\Delta B_0$ [1, 60]. The recovery of $\vec{M}_z$ in porous samples can be expressed as

$$\frac{M_z(t)}{M_z(eq)} = 1 - C(e^{-(\frac{t}{T_1}+t\rho_1\frac{S}{V})}), \tag{2.21}$$

where ρ_1 is the relaxivity term associated with longitudinal relaxation. A general growth and decay curve representing longitudinal and transverse relaxation respectively, is depicted in Figure 2.7 B.

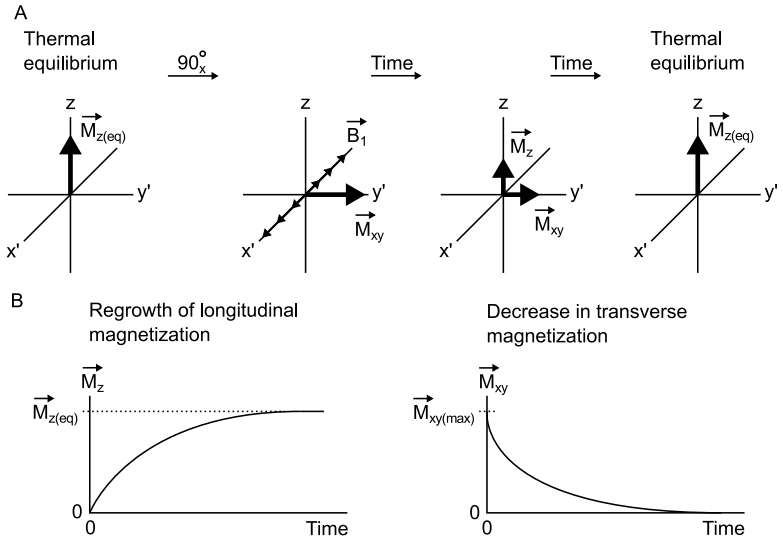

Figure 2.7: Relaxation shown in the rotating frame of reference after a 90°_{x} pulse where $\vec{B}_1$ is oscillating along the x-axis (A). The increase in longitudinal magnetization $\vec{M}_z$ and the decrease in transverse magnetization $\vec{M}_{xy}$, that occurs once the $\vec{B}_1$ field is turned off (B).

After the excitation pulse the signal must be recorded. Figure 2.8 depicts, in the laboratory frame, how the signal is recorded following a 90 degree RF-pulse. After the 90° excitation pulse the net magnetization is precessing in the xy-plane (Figure 2.8 A). The magnitude of the net magnetization is recorded as it precesses around in the xy-plane (Figure 2.8 B). After each complete precession, the the net magnetization will have decreased due to relaxation which causes its recorded path to decrease in magnitude (Figure 2.8 C). This recording of the y and x-component (real and imaginary respectively) of $\vec{M}_{xy}$ as a function of time is called the Free Induction Decay (FID) [57, 58, 60]. A Fourier transform (FT) of the FID converts the data from the time domain to the frequency domain and the resulting NMR spectra will show peaks that correspond to the resonance frequencies of the nuclei in the sample [57, 58, 60].

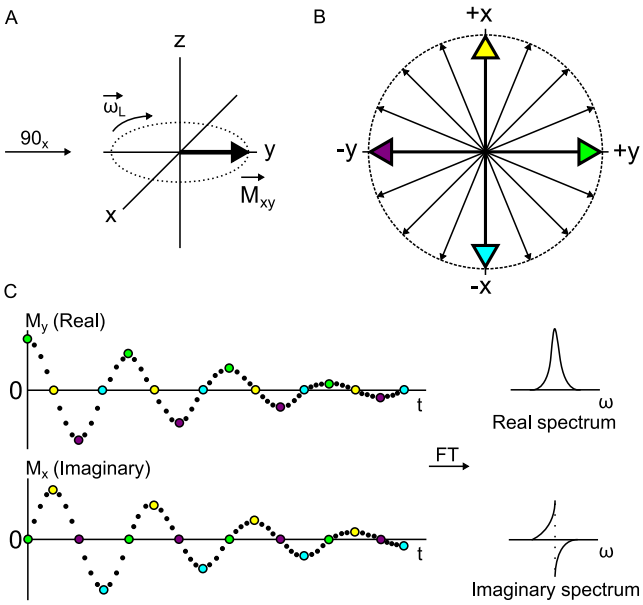

Figure 2.8: The origin of a simple NMR spectra. $\vec{M}_{xy}$ after a 90° pulse shown in the laboratory frame (A). The precession path of $\vec{M}_{xy}$ in the transverse plane shown in the laboratory frame (B). The recording of the real and the imaginary signal and the transformation from the time domain to the frequency domain by Fourier Transform (FT). The decrease in signal amplitude with time in the FID is caused by transverse relaxation (C). Note that the FID in C is only intended to schematically show the transformation from the time domain to the frequency domain and it therefore contains only one frequency and thus represents magnetically equivalent nuclei.

In diamagnetic molecules the effective magnetic field ($\vec{B}_{eff}$) experienced in nuclei is always lower than the externally applied magnetic field B_0. $\vec{B}_{eff}$ can be expressed as

$$B_{eff} = (1 - \sigma)B_0 \tag{2.22}$$

where σ is the shielding constant [57, 58]. The shielding constant depends on factors like magnetic anisotropy of neighbouring groups, substituents,

electric field effects, ring current effects and hydrogen bonding. The value of σ is nucleus specific. Nuclei in chemically different positions in a molecule experience different effective magnetic fields [57, 58].

From the Larmor equation (Equation 2.8) it is apparent that nuclei that are experiencing different magnetic fields, will also experience different Larmor frequencies. When taking B_{eff} into account, the actual signal frequencies of specific nuclei can be expressed as

$$\nu = \frac{\gamma B_0(1-\sigma)}{2\pi} \tag{2.23}$$

which means that strongly shielded nuclei (high shielding constant) will have lower frequencies and appear to the right in the frequency domain. It is also apparent from Equation 2.23 that the frequency is dependent on the externally applied field (B_0). That means that the results in the frequency domain are dependent on the field strength of ones spectrometer, which is unfortunate when researchers compare results. Therefore the chemical shift (δ) scale was was introduced, where the position of a peak is obtained by measuring its frequency offset from a reference frequency and then dividing by that reference frequency. The chemical shift is independent of B_0, its unit is parts per million (ppm) and it is expressed as

$$\delta = 10^6 \cdot \frac{(\nu - \nu_{ref})}{\nu_{ref}} \tag{2.24}$$

where ν_{ref} is the frequency of the reference compound. In most cases, proton chemical shifts range from 0 to approximately 12 [57, 58].

The splitting patterns seen in liquid state NMR are caused by nuclear spin-spin couplings. Such interactions are only possible through covalent bonds and are thus always intramolecular [61, 60].

Figure 2.8 C depicts an FID consisting of exclusively magnetically equivalent nuclei, i.e. nuclei with the same resonance frequency. Since non magnetically equivalent nuclei in real samples will have different resonance frequencies, the corresponding FID will be a sum of all of them. In addition to taking the data from the time domain to the frequency domain, the Fourier transform also separates each frequency in the FID. The Fourier transform is expressed as

$$g(\omega) = \int_{-\infty}^{\infty} f(t) e^{-i\omega t} dt \tag{2.25}$$

where $g(\omega)$ corresponds to the spectrum in the frequency domain and $f(t)$ corresponds to the spectrum in the time domain (the FID) [57, 58, 60].

2.2.2 Solid state NMR and Magic Angle Spinning (MAS)

Since its discovery, NMR was for many years considered to be suitable exclusively for liquid samples. Anisotropic nuclear interaction strongly depend on molecular orientation and are therefore averaged in liquids. This is generally not the case in solids where one encounters a rigid molecular arrangement. The lowered molecular motion in solids severely broadens the spectral linewidth. For example, the line width of liquid water is approximately 0.1 Hz while the line width of ice is approximately 100 KHz [64].

The idea of macroscopically rotating the sample (see Figure 2.9) to overcome the insufficient molecular motion in solids was introduced in 1958, where Andrew et.al. showed the linewidth of Sodium 23 spectra as a function of sample spin rate [65]. Andrew et.al. [66, 67] and Lowe [68] independently recognized that spinning can be used as a method for finding nuclear interactions in solids, which are obscured by dominant magnetic dipolar coupling [69].

The angular factor of the time dependent part of the truncated dipole-dipole interaction in rotating solids can be expressed as

$$\lambda(\theta) = \frac{1}{2}(3cos^2\theta - 1) \tag{2.26}$$

and it can be brought to zero by alligning the axis of rotation at what is called the magic angle (θ_{MA}) with respect to the external magnetic field B_0 [66, 69].

$$\theta_{MA} = cos^{-1}(\frac{1}{3})^{1/2} = 54.7^\circ \tag{2.27}$$

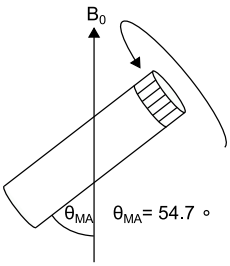

Figure 2.9: Rotor positioning used in the Magic Angle Spinning (MAS) technique.

In this thesis, solid state magic angle spinning (MAS) NMR is used for analysing adsorption onto mineral surfaces. Specifically it is used for studying the mechanisms responsible for the adsorption of polar components in crude oil onto mineral surfaces during crude oil aging. Since T_1 and T_2 relaxation times are related to the correlation time (τ_c) of molecular tumbling (see Figure 2.10, such measurements can indicate mobility of adsorbed species [70, 71]. Adsorption of polar components from crude oil onto mineral surfaces are thought to be the main driving force in wettability alteration of originally water-wet reservoirs.

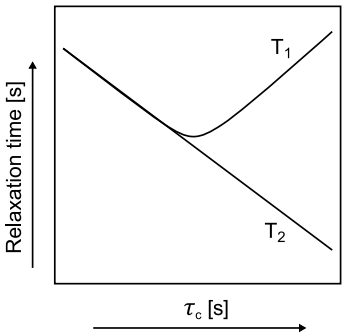

Figure 2.10: Relationship between correlation time of molecular tumbling and relaxation times T_1 and T_2. Figure inspired by [60].

2.2.3 Magnetic Resonance Imaging (MRI)

In conventional NMR spectroscopy strong efforts are made to make sure that the magnetic field is as homogeneous as possible throughout the sample. This is to ensure that the Larmor equation is fulfilled and all nuclei precess accordingly regardless of location in the sample [60].

$$\omega = \gamma B_0 \tag{2.28}$$

In Magnetic Resonance Imaging (MRI) the Larmor frequency is made spatially dependent by adding additional magnetic field gradients B_{grad} that vary the experienced magnetic field linearly across a direction in the sample.

$$B_{grad}(r) = G \cdot r \tag{2.29}$$

where $G = (\frac{\partial B_z}{\partial x}, \frac{\partial B_z}{\partial y}, \frac{\partial B_z}{\partial z})$ is the position independent magnetic field gradient and $r = (x, y, z)$ is the position [1, 60, 72]

$$\omega(r) = \gamma B_0 + \gamma G \cdot r \tag{2.30}$$

2D MRI is actually a 3D representation of data where the third dimension is the thickness of the image. Creating a 2D MRI therefore requires magnetic field gradients in three directions applied during three separate parts of the MRI pulse sequence. Gradients can only be active in one direction at the time [60, 73].

The first thing to consider when creating an MRI is the thickness of the image, i.e. the slice thickness. This part of the MRI pulse sequence is called the slice selection. Slice selection is usually achieved by applying a magnetic field gradient along the z-axis (G_z) thus creating spatially dependent Larmor frequencies along the z-axis. G_z is kept on during the excitation pulse [60, 73].

In conventional NMR, rectangular (hard) pulses, with pulse lengths in the order of microseconds and a broad range of frequencies, are used to excite all nuclei in the sample. The whole point of slice selection is to establish spatial resolution based on differences in Larmor frequency caused by the slice selection gradient G_z. Therefore, sinc or gaussian (soft) pulses are used in MRI. Soft pulses have a narrow band of frequencies and excite only nuclei with a certain range of Larmor frequencies [74, 75]. Pulse shapes and their corresponding excitation profiles following a Fourier transform is depicted in Figure 2.11.

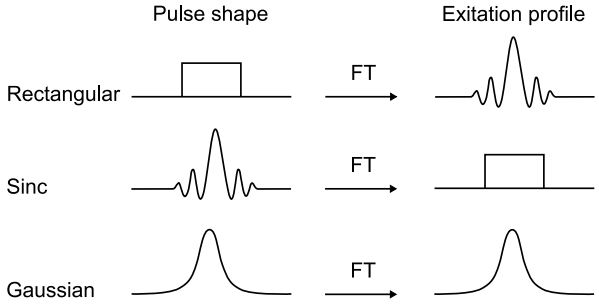

Figure 2.11: Pulse shapes and their corresponding excitation profile following a Fourier transform. Figure inspired by [74]

To change the slice thickness (see Figure 2.12) one can either alter the strength of G_z while keeping the bandwidth of the selective pulse constant or vice versa [60, 72, 73]. The relationship between slice thickness (Δz), pulse bandwidth (BW) and the strength of the z-gradient (G_z) is given by

$$\Delta z = \frac{BW}{|\gamma G_z|}. \tag{2.31}$$

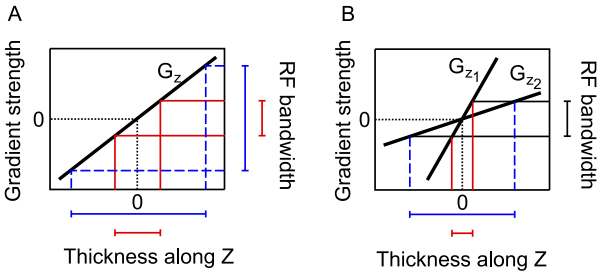

Figure 2.12: Slice thickness varied by varying the bandwidth of the RF pulse while keeping G_z constant (A). Slice thickness varied by varying the gradient strength of G_z while keeping the bandwidth of the RF pulse constant (B). Figure inspired by [73]

The center of the slice position along the z-direction (Z_0), for nuclei with a frequency offset (Ω_i) is is given by

$$Z_0(\Omega_i) = \frac{\Omega_i - \omega_{rf}}{\gamma G_z} \tag{2.32}$$

meaning that slice position can be altered (see Figure 2.13) either by altering the strength of G_z while keeping the frequency offset constant or vice versa [60, 61, 72, 73]. All slice positioning performed in this thesis is performed by varying the frequency offset of the RF pulse while keeping G_z constant.

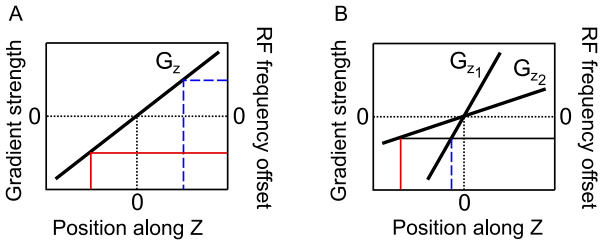

Figure 2.13: Slice position varied by varying the center frequency of the RF pulse while keeping G_z constant (A). Slice position varied by varying the gradient strength of G_z while keeping the center frequency of the RF pulse constant (B). Figure inspired by [73]

Although MRI is usually associated with an actual image (3D MRI), the use of gradients to obtain spatially resolved information in any direction is technically still MRI. The work presented in papers 3 and 4 shows how slice selection is used to obtain various parameters from chosen slices in various samples. Techniques like the ones described in papers 3 and 4 fall under the category of 1D magnetic resonance imaging.

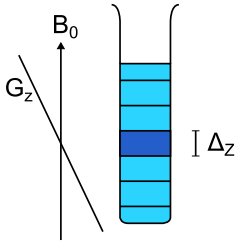

Figure 2.14: Schematic demonstration of slice selection in a test tube with a slice thickness Δz. The excited slice (dark blue) is in the iso center, meaning that the rf frequency offset must be zero.

The purpose of slice selection is to exclusively excite nuclei in the slice of interest (a specific volume element as shown in Figure 2.14). If relaxation is neglected, the NMR signal from a volume element dV is given by

$$dS(G_z, t) = \rho_z e^{i\omega_z t} dz \tag{2.33}$$

where $\omega_z = \gamma(B_0 + G_z \cdot z)$ (Equation 2.30), which gives

$$dS(G_z, t) = \rho_z e^{i(\gamma B_0 + \gamma G_z \cdot z)t} dz. \tag{2.34}$$

In the rotating frame, the γB_0 term from Equation 2.5 may be neglected (on resonance) [60]. The integrated signal can then be written as a function of time.

$$S(t) = \int \rho_z e^{i\gamma G_z \cdot zt} dz. \tag{2.35}$$

where dz represents volume integration [72]. The introduction of k-space [76] simplify Equation 2.35. The concept of k-space is defined by

$$k = \frac{\gamma}{2\pi} \int_0^t G(t) dt. \tag{2.36}$$

where k-values have units of reciprocal space, m^{-1} [60]. In Equation 2.36 G is the maximum magnetic field strength.

After G_z and the selective excitation pulse have excited the nuclei in the slice of interest, another gradient is applied in the y-direction. The purpose of this gradient is to cause a phase shift before the signal is recorded (see Figure 2.15). This process is called phase encoding and ensures spatial encoding along the y-axis. The corresponding k-space value (k_y) is expressed as

$$k_y = \frac{\gamma}{2\pi} \int_0^t G_y(t)dt = \frac{\gamma}{2\pi} \cdot G_y \cdot L_{G_y} \tag{2.37}$$

where L_{G_y} and G_y are respectively the length and intensity of the gradient along the y-direction [72].

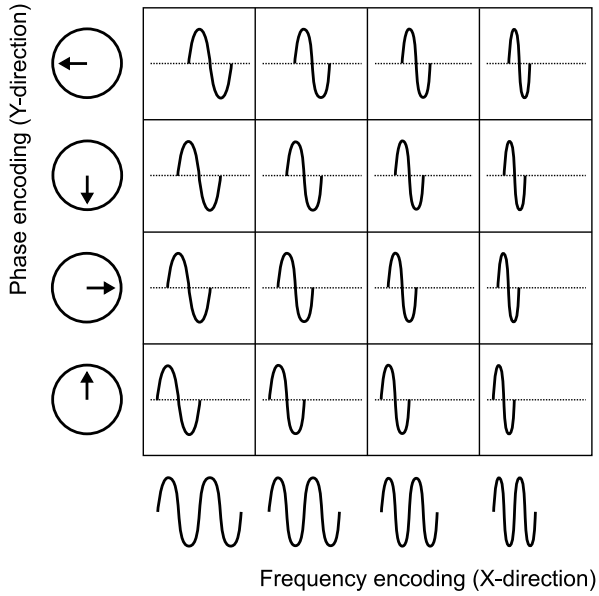

Figure 2.15: The principle of phase and frequency encoding shown in in a 4_x by 4_y image. Location along the x-direction is determined by the signal frequency. Location along the y-direction is determined by the signal phase.

For an image with a 10_y by 100_x resolution, ten phase encoding steps are needed, i.e. the sequence must be repeated 10 times with 10 different G_y values while keeping all other parameters constant. Since the resolution in the phase encoding direction is directly related to the number of times the pulse sequence must be repeated, it determines the length of the acquisition [60, 73].

After the phase encoding step, the signal is recorded while under the influence of a field gradient in the x-direction (G_x). This process is called frequency encoding. As the signal is recorded while G_x is active, the resulting frequencies from the Fourier Transform of the recorded echo coincides with positions along the x-direction (see Figure 2.15). The corresponding k-space value (k_x) can be expressed as

$$k_x = \frac{\gamma}{2\pi} \int_0^t G_x(t)dt = \frac{\gamma}{2\pi} \cdot G_x \cdot DW \cdot N_i \tag{2.38}$$

where DW is the dwell time, N_i refers to point number i in the echo and G_x is the gradient intensity along the x-direction [72].

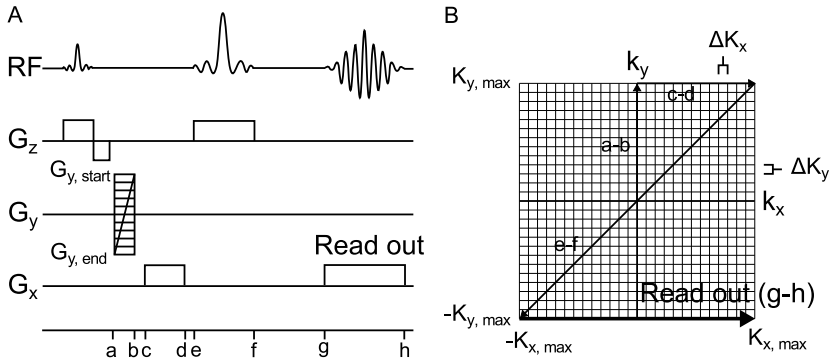

Figure 2.16: Spin echo MRI pulse sequence with slice selection in the z-direction, phase encoding in the y-direction and frequency encoding in the x-direction (A). The corresponding k-space coverage for the first phase encoding step (B). All Magnetic Resonance Images discussed in this thesis are acquired with spin echo sequences. Figure inspired by various examples shown by Callaghan [60].

As opposed to the the spatial encoding in the phase encoding direction, the spatial encoding in the frequency encoding direction is obtained from one recording. For an image with a 10_y by 100_x resolution, the sequence must only run 10 times. Frequency encoding is therefore preferred when possible, instead of phase encoding in 1D imaging [60, 73].

The k-space coverage in a general spin-echo experiment is shown in Figure 2.16. The sequence starts at $[k_x, k_y] = [0, 0]$. During the time $a - b$ the first phase encoding step moves the k-space position to $[0, k_{y,max}]$. The system is then moved to $[k_{x,max}, k_{y,max}]$ by the first x-gradient during the time $c - d$. The refocusing pulse the flips the system to position $[-k_{x,max}, -k_{y,max}]$ before the first k-space line is recorded under the influence of the frequency encoding (read out) gradient (G_x) during the time $g - h$. The relationship between k-space point separation (Δk_x and Δk_y) and the image space Field Of View (FOV) can be expressed as

$$\Delta k_i = \frac{1}{FOV_i} \tag{2.39}$$

where i is the spatial dimension in the x or y direction. The image-space resolution Δi is related to the maximum k-space value ($k_{i,max}$) as follows [1, 72].

$$\Delta i = \frac{2}{k_{i,max}} \tag{2.40}$$

As described above, an image contains data in three different directions. However, when averaged normal to the slice (z-direction), the signal (S) is given by

$$S(k_x, k_y) = \int_{-\infty}^{\infty} \int_{-\infty}^{\infty} \rho(x, y) e^{i2\pi(k_x x + k_y y)} dx dy \tag{2.41}$$

which is the two-dimensional Fourier transform of $\rho(x, y)$ (i.e. the volume density function of $\rho(x, y, z)$ when averaged to the slice). The reconstruction of $\rho(x, y)$ from $S(x, y)$ is achieved by the two-dimensional inverse Laplace transform [60].

$$\rho(x, y) = \int_{-\infty}^{\infty} \int_{-\infty}^{\infty} S(k_x, k_y) e^{-i2\pi(k_x x + k_y y)} dk_x d_k y \tag{2.42}$$

2.2.4 Self-diffusion

Self-diffusion (shown in Figure 2.17), caused by kinetic energy is the random Brownian motion of molecules in uniform or pure solutions [77, 78, 79, 80]. The self-diffusion coefficient (D) is a measure of molecular movement and can thus be used on adsorbed species as a measure of mobility. In paper 2, self-diffusion coefficients and self diffusion weighted spectra were used to predict the mobility of polar components from crude oil adsorbed onto mineral surfaces.

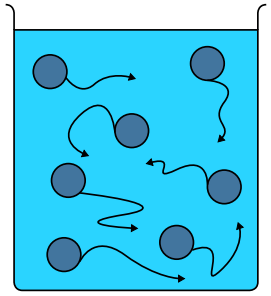

Figure 2.17: Self-diffusion or Brownian motion of molecules in a uniform solution. Figure inspired by [61].

Magnetic field gradients are also used in diffusion measurements. Self-diffusion coefficients can be determined from the Pulsed field Gradient Spin Echo (PFGSE) NMR experiment, where increased physical movement of species reduces the effectiveness of the refocusing pulse and thus decreases the signal intensity. The signal amplitude S, is given by

$$S(g, t_E) = M_0 \, e^{-\frac{t_E}{T_2}} \, e^{-\gamma^2 \delta^2 G^2 (\Delta - \frac{\delta}{3}) D} \tag{2.43}$$

where t_E is the echo time, T_2 is the transverse relaxation time, γ is the gyromagnetic ratio, δ is the length of the gradient pulses and Δ is the diffusion time. $S(g, T_E)$ can be normalized with respect to the echo intensity (E) at $G = 0$ [81, 82].

$$E(g, \Delta) = E(g, t_E) = \frac{S(g, t_E)}{S(g = 0, t_E)} = e^{-\gamma^2 \delta^2 G^2 (\Delta - \frac{\delta}{3}) D} = e^{-bD} \tag{2.44}$$

where b is the diffusion weighting factor defined by $-\gamma^2\delta^2G^2(\Delta - \frac{\delta}{3})$.

In the PFGSE sequence explained above magnetic field gradients are used to dephase and refocus the signal. The discrepancy between before and after these two gradient applications is caused by diffusion. Self diffusion under the influence of a constant internal magnetic field gradient (G_0) can also be utilized to probe pore geometry in porous media. For CPMG experiments in fluid saturated porous media under a constant G_0, the echo attenuation is given by

$$\frac{M(t_E)}{M(t_E = 0)} = e^{-t_E\rho_2\frac{S}{V} - bt_E^3} \tag{2.45}$$

where $b = \frac{1}{12}D\gamma^2G_0^2$ when assuming free diffusion [83]. Diffusion in porous media under a constant internal magnetic field gradient is further discussed under 2.2.5.

2.2.5 Internal magnetic field gradients

In conventional high field NMR spectroscopy, small volumes of liquid samples are investigated in glass tubes. Great technological efforts are made to ensure a homogeneous magnetic field throughout the sample volume. The variation in the magnetic field (ΔB_0) is proportional to the spectral half width ($\Delta\nu$) and inversely proportional to the time constant (T_2^*) of the Free Induction Decay (FID), meaning that field inhomogeneities will broaden the spectral linewidth and shorten the lifespan of the observed signal (see Figure 2.18) [1, 60].

$$\Delta\nu \approx \frac{1}{\pi T_2^*} \approx \frac{1}{T_2} + \gamma \Delta B_0 \tag{2.46}$$

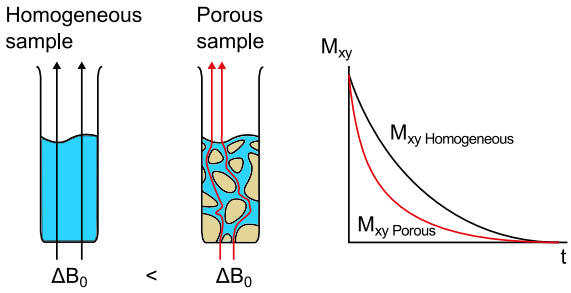

Figure 2.18: Schematic showing how the heterogeneous magnetic field in a fluid saturated porous sample affects the transverse magnetization M_{xy} over time.

When analysing liquid samples in superconducting magnets, $\Delta B_0 \approx 0$. If the liquid is confined in porous media however, this is no longer true. The apparent difference in magnetic susceptibility ($\Delta\chi_{app}$) between the liquid and the solid matrix induces internal magnetic field gradients (G_0) which distorts the magnetic field [31, 60, 84, 85].

Sun and Dunn [37] showed that the internal gradient can be measured by implementing a modified 2D CPMG sequence where the number of 180° pulses in the echo train is varied over a constant time period. By varying the number of 180° pulses over a constant time period, the echo time is varied as

well. The echo time is defined as $t_E = 2\tau' + L_{P(180)}$ where τ' is the spacing on each side of the 180° pulse and $L_{P(180)}$ is the length of the 180° pulse. The strength of G_0 depends on both the external magnetic field and the geometry of the porous media [31, 63, 83, 86].

$$G_0 \approx \frac{B_0 \Delta\chi_{app}}{a} \tag{2.47}$$

Brownian motion causes self-diffusion, which in porous media is restricted by the pore matrix. Hürlimann [83] showed that the diffusion term, involved with the echo attenuation of the transverse magnetization for a CPMG experiment with n echoes and a constant G_0, is governed by three length scales.

$$\frac{M(t_E)}{M(t_E = 0)} = e^{-t_E \rho_2 \frac{S}{V} - \frac{1}{12} D\gamma^2 G_0^2 t_E^3} \tag{2.48}$$

The dephasing length, defined as $l_g = (\frac{2\pi D}{\gamma G_0})^{\frac{1}{3}}$, is the distance molecules have to travel in order to dephase 2π radians. The diffusion length, defined as $l_D = (Dt_E)^{\frac{1}{3}}$, is the length a molecule travels due to diffusion during the echo time t_E. The final length scale is the structural length, which in porous media is defined as the pore diameter, $l_s = a$ [31, 83].

From these length scales, three diffusion regimes arise. In instances where the pore length is the shortest length scale, i.e. $l_s << l_D$ and $l_s << l_g$, the system behaves according to the Motional Averaging (MAV) regime. The MAV regime is valid for samples with small pore sizes and a low $B_0\Delta\chi_{app}$ term. Due to the small pore diameter associated with the MAV regime, molecules will hit the pore wall before complete dephasing during the echo time t_E [31, 63, 83, 85]. The experiments performed in this thesis involve an 11.7T NMR spectrometer and samples with a relatively large pore diameter. The MAV regime is therefore unlikely to be encountered.

The Localization (LOC) regime applies when the dephasing length is the shortest length scale, i.e. $l_g << l_D$ and $l_g << l_s$. The LOC regime is valid in samples where the $B_0\Delta\chi_{app}$ term is large and the dephasing length (l_g) is very short. Only molecules located at a distance of l_g or less from the pore wall will contribute to the echo and therefore the LOC regime is associated with a large echo attenuation [31, 63, 83, 85].

In the Free Diffusion (FD) regime, the diffusion length is the shortest length scale, i.e. $l_d << l_s$ and $l_D << l_g$. The FD regime determines diffusion behaviour in samples with large pores where most molecules never experience the pore walls. Internal gradient values in the FD regime are expected to

be moderate during the echo time t_E, which results in a moderate echo attenuation.

Because of the high $B_0\Delta\chi_{app}$ term associated with the 11.7 T NMR spectrometer used in the work presented in this thesis, molecules are most likely subjected to a regime somewhere between the LOC and FD regime during a spin echo acquisition. Mitchell et al. [87, 88] introduced a method for analysing CPMG data in inter-regimental systems. When working with inter-regimental systems Equation 2.48 is expressed in a general form

$$\frac{M(t_E)}{M(t_E=0)} = e^{-nt_e\rho_2\frac{S}{V}-bnt_E^k} \tag{2.49}$$

where b describes decay due to diffusion in the internal gradient and k describes the dependence of the diffusion component on the echo time [87, 88]. After analysis according to Equation 2.49 and the data collapse plot [83] the porous samples used in this thesis were found to have k values between 1 (LOC regime) and 3 (FD regime) however analysis according to the FD regime ($k = 3$) has provided reasonable results for pore size distributions [49] and wettability [50].

In the work presented in this thesis, internal gradient measurements were acquired with a modified CPMG sequence [37, 89]. Slice selective acquisition allowed for spatially resolved results in addition to results averaged over the entire sample [49, 50]. The resulting data have been processed to produce pore size distributions, sample heterogeneity plots and a fluid specific dimension of confinement. The modified CPMG sequence used in this thesis produces 32 spectra weighted on G_0 and D. The FD regime is assumed, where $k = 3$ and $b = \frac{1}{12}D\gamma^2G_0^2$.

Pore size distributions can be produced from $G_0 - \Delta\chi_{app}$ correlations (Equation 2.47) in porous samples saturates with one fluid, e.g. water. The results can then be expressed as

$$M(\tau`, t_{FID}) = \iint P(b, T_2^*)e^{-bn\tau`^3}e^{-\frac{t_{FID}}{T_2^*}}dbdT_2^*. \tag{2.50}$$

where $t_{FID} = td \cdot dw$, td is the number of points and dw is the dwell time. $G_0-\Delta\chi_{app}$ correlations can be found from $P(b, T_2^*)$, where $b = \frac{1}{12}D\gamma^2G_0^2$ and $T_2^* = \frac{2}{\gamma B_0\Delta\chi}$, after a 2D Inverse Laplace Transform (ILT).

Correlations between high internal gradient values and high absolute values of spectral frequency offset intervals (Δf) indicate homogeneity while a more full range of G_0 at all spectral frequencies indicate heterogeneity

[90, 91]. Heterogeneity plots can therefore be produced from $G_0 - \Delta f$ correlations. To create such plots one can divide the 32 $G_0^2 D$ weighted spectra into frequency intervals and calculate internal gradient distributions from each frequency interval. The results are then expressed as

$$\frac{M(t_f, \tau`)}{M(0)} = \iint P(f, b) e^{-bn\tau`^3} e^{-i\Delta t_f} df\, db. \tag{2.51}$$

A method created for determining wettability must be able to predict fluid distribution of minimum two fluids (here oil and water) while the fluids are present in the same pore space simultaneously. Pore size distributions created from $G_0 - \Delta\chi_{app}$ correlations are good indications of pore geometry in porous media saturated with one fluid. While this is useful in many other aspects, $\Delta\chi_{app}$ is calculated from the time constant (T_2^*) of the FID which only works if the FID exclusively consists of signal from one fluid. In a wettability related experiment the FID will contain signal from both water and oil.

$$\Delta\nu \approx \frac{1}{\pi T_2^*} \approx \frac{\gamma}{2\pi} B_0 \Delta\chi_{app} \tag{2.52}$$

However, if the two signals are distinguishable by chemical shift one can calculate the $\Delta\chi_{app}$ term from the spectral half width ($\Delta\nu$) according to Equation 2.52. The resulting 32 spectra in this case have two signals (oil and water), where the intensities are weighted on $G_0^2 D$. The data can then be expressed as

$$I(\tau`) = \int P(b) e^{-bn\tau`^3} db \tag{2.53}$$

where $b = \frac{1}{12} D\gamma^2 G_0^2$ (FD regime). Fluid specific G_0 distributions can be calculated from the $P(b)$ distributions and the diffusion coefficients of water and oil. Correlations between $\Delta\nu$ and G_0 can then be used to convert the G_0 distribution to a fluid specific dimension of confinement (DOC) distribution. The DOC is a fluid specific "pore size" expressed as seen below [50]. As the DOC is fluid specific (calculated from the individual oil and water signal) it is no longer a pore size, but rather a measure of the fluid confinement.

$$DOC \approx \frac{2\pi\Delta\nu}{\gamma G_0} \tag{2.54}$$

Chapter 3

Methods and materials

This chapter outlines the experimental parameters of the work presented in this thesis.

3.1 Materials

The parameters of all solid and liquid compounds used in this thesis are summarized in Tables 3.1 and 3.2.

Table 3.1: Relevant parameters for all solid compounds used in this thesis.

Solids	**Provider**	**Particle size range**	**Paper**
Calcium carbonate	Sigma-Aldrich	1-25 μm	1 and 2
NC4X quartz	The Quartz Corp	50-260 μm	1, 2 and 4
Glass beads	Thermo Scientific	5-50 μm	3
Glass beads	Duke Scientific Corp	140-165 μm	3

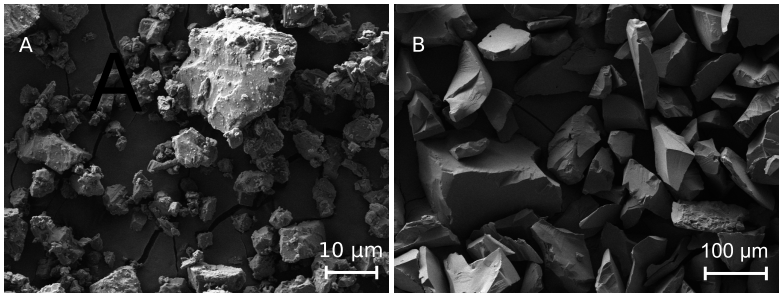

Figure 3.1: Scanning Electron Microscopy (SEM) image of calcite (A) and quartz (B) crystals.

Table 3.2: Relevant parameters for all liquid compounds used in this thesis.

Liquids	**Provider**	**Specifics**	**Paper**
Crude oil	Grane oil field	TAN =2 mg KOH g^{-1}	1 and 2
Decane	Sigma-Aldrich	-	1 and 2
Decalin	Sigma-Aldrich	-	1 and 2
Heptane	Sigma-Aldrich	-	1 and 2
Light mineral oil	Sigma-Aldrich	-	4
Trimethylchlorosilane	Sigma-Aldrich	5 % TMCS in heptane	4
Distilled water	University of Bergen	-	3 and 4

3.2 Sample preparation

Four sample types were investigated in this thesis. These four different sample types were regular liquid state samples, powder samples for MAS NMR, porous liquid saturated samples for MRI and model core samples for MRI.

3.2.1 Powder samples for solid state MAS NMR

The powder samples for magic angle spinning, analysed in papers 1 and 2, were prepared as depicted in Figure 3.2. Mineral powders were first kept in a desiccator, containing a saturated K_2SO_4 solution, for 14 days. This procedure covers the mineral powder with a thin film of water [92]. In studies of adsorption of polar components from model oils, this water film has been shown to increase adsorption by up to 100 % [11, 24]. Then the mineral powder was mixed with crude oil (Grane) at 80°C for 24 hours before the powder was separated from the supernatant oil in a centrifuge. The powder was then cleaned several times and left to dry in a fume hood for 24 hours. Lastly, the aged powder was transferred to 4 mm MAS rotors. This procedure was performed on quartz and calcite powder.

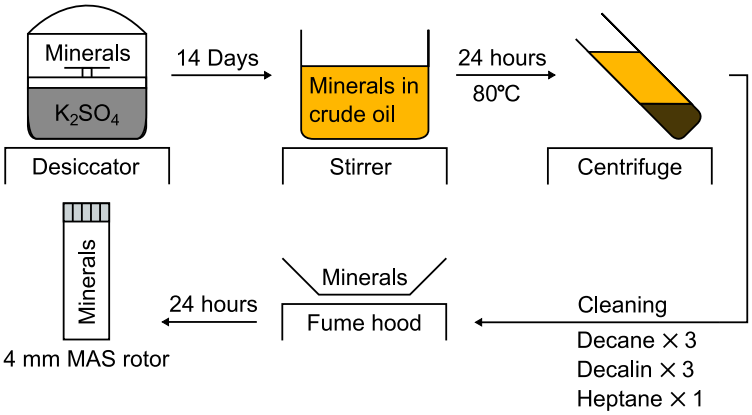

Figure 3.2: Schematic showing wet crude oil ageing of mineral powders. This procedure was used to generate samples for papers 1 and 2. Post ageing, the samples were investigated with solid state MAS NMR.

3.2.2 Liquid state NMR samples

The only liquid state samples investigated in this thesis are shown in paper 1. These samples contain oil from before and after the ageing procedure explained under subsection 3.2.1. The oil was investigated before and after ageing to look for observable differences due to adsorption. The supernatant oil was removed after the powder/oil suspension was centrifuged (see Figure 3.2). The before and after ageing oil samples were diluted 1:1 in deuterated chloroform.

3.2.3 Porous liquid saturated samples for MRI

All porous liquid saturated samples for MRI contained glass beads saturated with distilled water. These samples were used for method development in paper 3. Glass beads of two different grain size ranges (5-50 μm and 140-165 μm) were used to create samples with varying internal gradient. A layered sample containing two layers of (bottom coarse and top fine) glass beads was used to demonstrate a slice selective pulse sequence (see Figure 3.3). All liquid saturated porous samples for MRI was prepared in an MRI tube with an outer diameter of 2.5 cm and saturated with distilled water by vacuum.

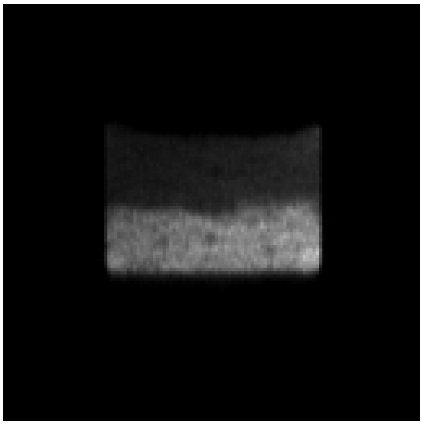

Figure 3.3: MR-image showing a layered water saturated porous sample. Top layer contains fine (5-50 μm) glass beads and the bottom layer contains coarse (140-165 μm) glass beads.

3.2.4 Model core samples

Model core samples were created to allow displacement experiments in pure quartz sand. These samples consist of sand being mechanically held in place inside a plexi-glass cell. All components on the plexi-glass cell are non-magnetic in order to allow displacement experiments to be performed inside the NMR spectrometer. The cell is equipped with filters to prevent sand from escaping into the inlet and outlet tubing. Before every displacement experiment, the quartz sand was saturated with distilled water by vacuum.

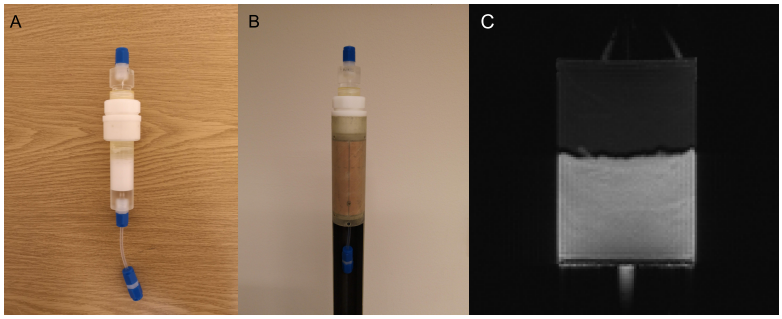

Figure 3.4: Model core sample where quartz sand is being held in place in a plexi-glass cell shown outside (A) and inside (B) a MicWB40 micro imaging probe. Example MRI from the model core sample taken half way through an oil drive (C). The plexi-glass cell has an outer diameter of 2.5 cm and the length of the model core sample is approximatelly 3.0 cm.

The model core samples were used in paper 4. Two samples were prepared, where one consisted of untreated quartz sand (water-wet) while the other consisted of treated quartz sand (oil-wet). The oil-wet surface of the treated sand was achieved through a silanization process. Pure quartz sand was submerged in a trimethylchlorosilane (TMCS) 5% in heptane solution for 20 minutes at ambient temperature. The mixture was shaken up every few minutes to ensure full adsorption. thereafter the sand was cleaned 5 times in heptane and left to dry in a fume hood. During this process thrimethylsilane adsorbs to the OH-sites on the quartz surface, thus making it hydrophobic (see Figure 2.3).

3.3 Displacement experiments

The displacement experiments performed in paper 4 was performed inside the bore of a Bruker 500 MHz WB spectrometer as shown in Figure 3.5. The samples were model core samples consisting of pure quartz sand with a particle size range of $\approx$ 50-250 μm, held in place in a plexi-glass cell.

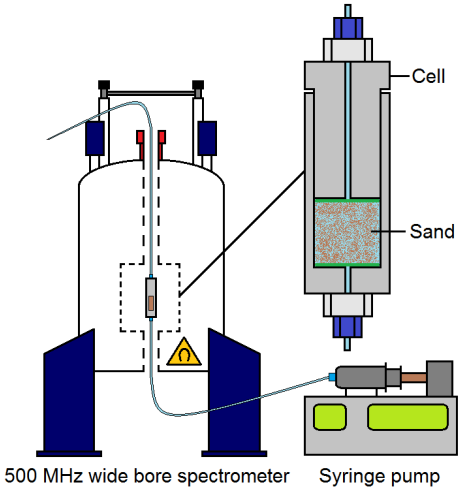

Figure 3.5: Schematic of liquid being pumped through the flow cell while it is placed inside the spectrometer.

Before every displacement experiment the samples were saturated with distilled water. The cell has a known volume and the porosity of the sample was determined by weighing the cell before and after water was introduced. During drainage and imbibition experiments, endpoint saturations such as the immobile water saturation ($S_{w,i}$) and the residual oil saturation ($S_{o,r}$) were determined to occur after 5 pore volumes of the displacing fluid had entered the sample. The flow was controlled by a Nexus 6000 syringe pump and the flow rate was set to 30 ml/hour.

3.4 Hardware

Two NMR spectrometers were used in this thesis. The primary instrument was a wide bore (WB) Bruker Ascend 500 MHz spectrometer. The Bruker 500 WB was equipped with separate probes for solid state NMR, liquid state diffusion NMR and Magnetic Resonance Imaging (MRI). The solid state MAS probe was a Bruker MAS probe with a maximum spin rate of 15 000 Hz. The diffusion probe was a commercial Bruker diffBB broadband gradient probe capable of delivering a z-gradient of up to 17 Tm^{-1}. The MRI probe was a commercial MicWB40 micro imaging probe. The micro imaging probe was used with the Bruker Micro 2.5 gradient system, which is capable of delivering gradient strengths of up to 1.5 Tm^{-1}.

The second spectrometer is a standard bore Bruker Ascend 850 MHz. The 850 SD spectrometer is exclusively set up for liquid state NMR and in this thesis it was exclusively used for liquid state NMR of oil samples before and after ageing in paper 1.

The pump used for displacement experiments was a Nexus 6000 syringe pump. The Nexus 6000 flow rate control has an accuracy of $\pm$ 0.35 % of the set rate and a reproducibility within 0.05 %.

3.5 NMR pulse sequences

NMR spectroscopy is a major analytical tool but it is also a field of study in itself. There are hundreds of NMR pulse sequences, where all are engineered to determine a certain physical or chemical property. They are all however, built on the polarization of the net magnetization caused by the external magnetic field created by the spectrometer. This section will provide explanations for all pulse sequences used in this thesis. The only nucleus studied in the work presented in this thesis is the proton (^{1}H).

3.5.1 Pulse-acquire

The simplest pulse sequence is the pulse-acquire (see Figure 3.6). In this sequence the polarization along the z-axis is transferred into the transverse plane with an additional magnetic field $\vec{B_1}$ applied perpendicular to the external magnetic field $\vec{B_0}$. For maximum transverse magnetization, $\vec{B_1}$ is turned on for the amount it takes to transfer the polarization 90° away from the z-axis. Such a disturbance from thermal equilibrium is termed a 90° pulse. Since the pulse angle is proportional to signal intensity, lower pulse angles may be appropriate in very concentrated samples.

Immediately after the pulse is turned off, the rotational path of the net magnetization in the transverse plane is recorded as the polarization reverts towards thermal equilibrium (see Figure 2.8 B and C). This generates the FID. The Fourier transform of the FID generates the 1D NMR spectrum.

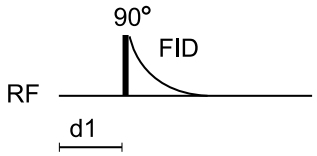

Figure 3.6: 90° pulse-acquire pulse sequence where d1 is the delay time and should be set to minimum 5 T_1.

The spectrum one obtains is actually an average of several acquisitions recorded by repeating the pulse sequence. To make sure each repetition has the same initial conditions, a delay time (d1) is incorporated into the

sequence. The polarization in the transverse plane may be depleted (M_{xy}= 0) before the the longitudinal magnetization is completely recovered ($M_z < M_{z(eq)}$) as these are two independent processes. The delay time ($d1$) is set to make sure that longitudinal relaxation is complete before the next repetition begins. The parameter $d1$ is used to ensure equal initial conditions for each repetition in most NMR pulse sequences. In this thesis the pulse-acquire sequence has been used in papers 1 and 4.

3.5.2 ^{1}H-^{1}H double-quantum single-quantum

The ^{1}H-^{1}H double-quantum single quantum sequence, shown in Figure 3.7, provides ^{1}H$-^1$H correlation spectra. In paper 1, it was used for determining the molecular structure, through spin-spin couplings, of adsorbents on quartz and calcite surfaces.

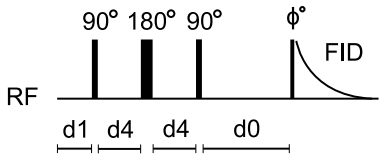

Figure 3.7: ^{1}H-^{1}H double-quantum single-quantum filtered pulse sequence.

3.5.3 Inversion Recovery

The inversion recovery (IR) sequence is used to obtain longitudinal (T_1) relaxation times (see Figure 3.8 A). In this sequence the polarization is inverted by a 180° pulse before a variable delay time (v_d) is implemented where the system relaxes with a time constant T_1^{-1}. After v_d, a 90° pulse, with the same phase as the first 180° pulse, is applied. This 90° pulse moves the polarization of the magnetization from the z-direction into the xy-plane where the FID is immediately recorded.

The time v_d is varied from very short up to enough time to ensure full relaxation via several steps within one repetition of both dimensions of the sequence. The longer the time v_d, the more longitudinal relaxation has occurred (more magnetization along positive z-direction) before the 90° pulse flips it into the xy-plane. Therefore, as v_d is increased so is the recoded

xy-magnetization and the final signal intensity. When v_d is long enough to ensure full longitudinal relaxation before the 90° pulse, the recorded signal is at a maximum (see Figure 3.8 B). The result of this sequence is NMR spectra where the individual signal intensities increases as a function of the variable time delay with the time constant T_1^{-1}.

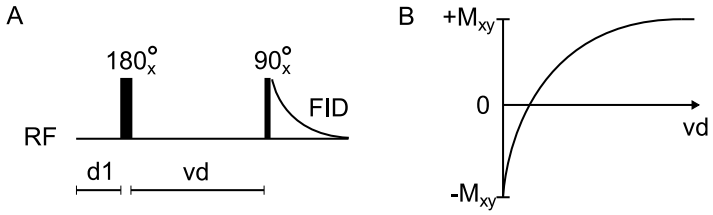

Figure 3.8: The inversion recovery pulse sequence (A) and the resulting increase in magnetization (B) as the variable delay time (v_d) is increased.

3.5.4 The spin echo and CPMG

The spin echo was introduced in 1950 [93] and is, still to this day, one of the greatest advancements in the field of nuclear magnetic resonance. In the spin echo, the signal loss associated with inhomogeneities in the external magnetic field is refocused by the 180° pulse resulting in an echo with a signal maximum occurring at $2t + L_{P(180)}$ (see Figure 3.9 A).

The Carr-Purcell-Meiboom-Gill (CPMG) pulse sequence [38, 39] is based on the spin echo and uses a series of 180° pulses to refocus the signal several times, which produces a series of echoes where the signal attenuation between echoes is solely caused by inter-nuclear relaxation. The time constant of the echo attenuation is T_2^{-1}. The attenuation comes from the fact that the echoes further out in the sequence have had more time for irreversible inter-nuclear relaxation. The time $t_{e,rec}$ is the time from excitation to the echo is recorded (see Figure 3.9 B).

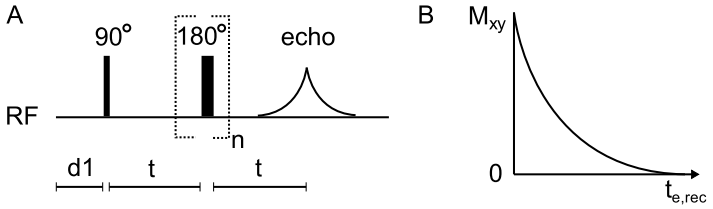

Figure 3.9: The spin echo (if n=1) and the CPMG pulse sequence (A) and the resulting decrease in magnetization in the xy plane (B) as the number (n) of 180° pulses in the echo train is increased.

3.5.5 IR-CPMG

In paper 2, correlations between T_1 and T_2 relaxation times [94] were recorded using a combined IR-CPMG sequence as shown in Figure 3.10. The variable delay time (v_d) in the IR part was logarithmically varied between 1 ms and 15 s in 32 steps (T_1 decoding) while the total number of echoes in the echo train was 10240.

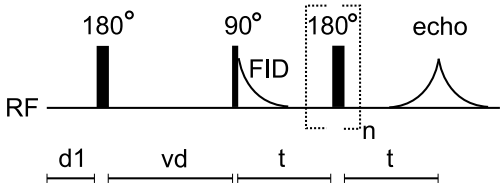

Figure 3.10: The combined IR-CPMG pulse sequence. T_1 is decoded by varying the variable delay time, while T_2 is decoded in the echo train.

3.5.6 PFGSE

The Pulsed Field Gradient Spin Echo (PFGSE) sequence [81, 95], shown in Figure 3.11, was used in paper 2 to obtain diffusion weighted spectra and self-diffusion coefficients. Between the excitation pulse and the refocusing pulse, a gradient pulse (G_z) is applied. This gradient pulse induces a phase shift that is dependent on z-position. The 180° rf-pulse then inverts the trajectory of that phase shift.

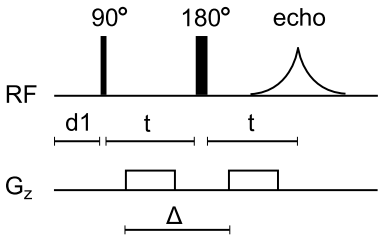

Figure 3.11: Pulsed Field Gradient Spin Echo (PFGSE) pulse sequence with gradient pulses along the z-direction.

During the diffusion time (Δ), self-diffusion causes some nuclei to change position. The second gradient pulse is of equal magnitude and length as the first one and its purpose is to refocus the phase shift induced by the first gradient pulse. However, only nuclei that has not moved, can be refocused by the second gradient pulse. Thus, signal decay increases with increased diffusion.

In paper 2, the diffusion time was set to 20 ms. The pulse length of the sine shaped gradient pulse was 0.8 ms and the gradient strength was linearly varied between 0 and 15 T m^{-1} .

3.5.7 Modified CPMG

The modified CPMG sequence [37] used in this thesis is depicted in Figure 3.12. In the modified CPMG sequence, DG_0^2 encoded signal decay is the result of varying the time available for irreversible dephasing due to diffusion in the internal gradient. This sequence was used on fluid saturated porous samples in papers 3 and 4, where internal gradients (G_0) were induced by magnetic susceptibility differences between the fluids and the solid matrix.

The conventional CPMG sequence produces an echo train where the signal decay from echo to echo is T_2^{-1} weighted. As the signal is being refocused from one recorded echo to the next, the echo intensity is a function of time lapsed since excitation. In the modified CPMG sequence however, the time from excitation to the signal is recorded is constant through the entire sequence. Instead, the time (τ) between the 180° refocusing pulses is varied by varying the number (n) 180° pulses applied over the constant time T (see Figure 3.12).

This sequence can be applied with and without spatial resolution and the resulting data can be processed according to several different methods (see Section 2.2.4).

Figure 3.12 B shows how the sequence progresses in a demonstrative example. When applied in papers 3 and 4, n 180° pulses was varied from 32 to 1 in 32 steps. The constant time T must be set so that the signal is close to zero when only one 180° pulse is applied, i.e. during the last step. In paper 3, only water saturated samples were used and a constant time T=20 ms was sufficient. In paper 4, mineral oil was introduced and T=50 ms had to be used due to the lower diffusion coefficient in oil.

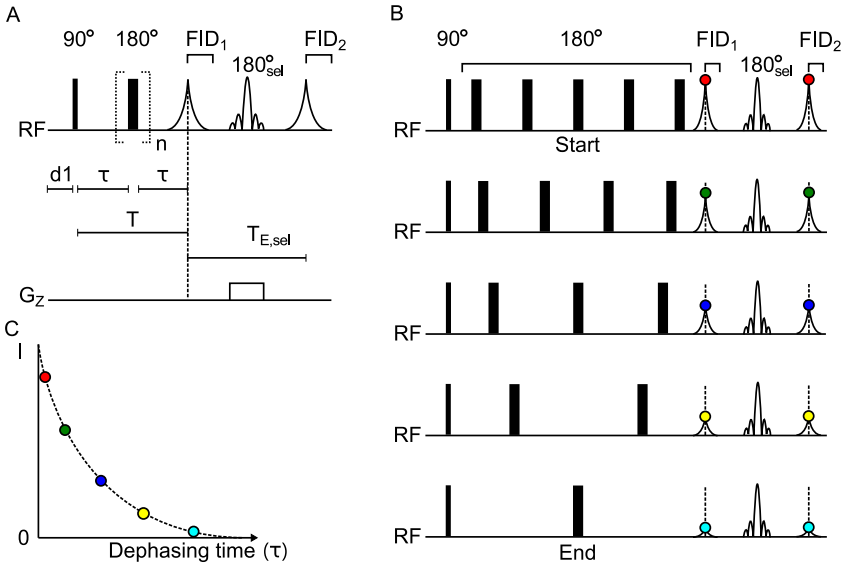

Figure 3.12: The modified CPMG pulse sequence used in this thesis. The sequence is non spatially resolved if FID_1 is recorded and spatially resolved if FID_2 is recorded (A). A demonstration with 5 steps showing how the sequence changes when n 180° pulses is varied from five to one (B). The resulting decrease in signal intensity I, as a function of the dephasing time τ (C).

The pulse lengths of the hard 90° and 180° pulses were calibrated to 44 and 88 μs respectively. The pulse length of the 180° sinc pulse used in the spatially resolved version of the sequence was 719 μs. The gradient strength during slice selection G_z and the bandwidth of the 180° sinc pulse was $1.4797{\cdot}10^{-4}T^{-1}m^{-1}$ and 6300 Hz respectively. These parameters were the same for both papers 3 and 4.

3.5.8 Spin echo in MRI

All MR-images presented in papers 3 and 4 were recorded using a Rapid Acquisition with Relaxation Enhancement (RARE) sequence. However, the rare factor was set to 1 to maximize the signal in the fluid saturated porous samples investigated in this work. With a RARE factor set to 1, the sequence is a regular spin echo with one refocusing pulse. The echo time was minimized to 2.91 ms and the repetition time was held at 1 s to ensure T_1 weighting in images where oil and water was present at the same time.

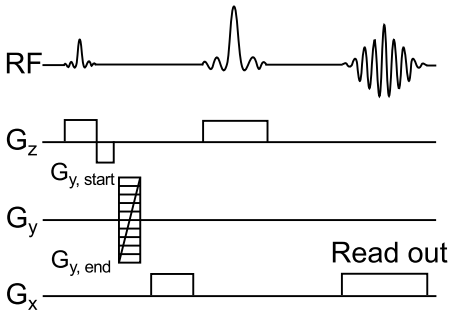

Figure 3.13: The MRI spin echo pulse sequence with axial slice selection, phase encoding in the y-direction and frequency encoding in the x-direction.

Chapter 4

Results and discussion

This chapter highlights the main results from papers 1-4.

4.1 Molecular level investigations

In papers 1 and 2, molecular level investigations were performed to probe the mechanisms responsible for the change in wetting state that occurs during crude oil ageing of calcite and quartz. The same samples were investigated in papers 1 and 2. In paper 1, assignment of adsorbed species was preformed with pulse acquire spectra and ^{1}H-^{1}H DQSQ spectra recorded at 10 KHz MAS rate. T_1 relaxation weighted spectra were recorded at 10 KHz MAS rate to investigate the mobility of individual adsorbed species. T_2 relaxation times, averaged over the entire sample were also recorded during a freeze study and the data were fitted to a three component model. This section highlights the main results. For a more detailed explanation, the reader is referred to the published papers.

4.1.1 Assignment of adsorbed species

Solid state ^{1}H NMR spectra from the calcite and quartz surfaces are shown in Figure 4.1. The spectra have been adjusted to represent the same surface area. The calcite surface (Figure 4.1 A) contains water at $\delta \approx 4.7$ ppm, methyl groups at $\delta \approx 0.9$ ppm and methylene groups at $\delta \approx 1.3$ ppm. The aliphatic region of the spectrum (δ = 0-3 ppm) is the dominate region.

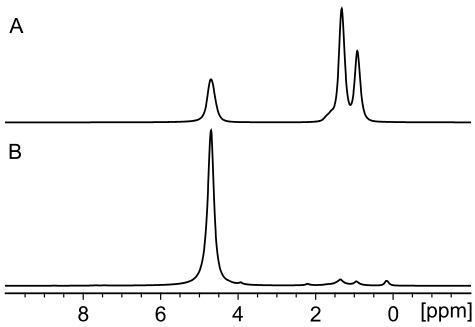

Figure 4.1: ^{1}H MAS spectra of the calcite (A) and quartz (B) surfaces after crude oil ageing recorded with a 90° pulse-acquire sequence with a MAS rate of 10 KHz. The quartz spectra is enhanced by a factor of 12.3 to compensate for the difference in surface area between the quartz and the calcite sample.

The opposite was observed for the quartz surface (Figure 4.1 B). Some methyl and methylene groups were present on the quartz surface. However, water was by far the dominate species. Note the signal occurring around $\delta \approx 0$ ppm. This is clearly present on the quartz surface and barely visible on the calcite. Its chemical shift suggests that it originates from methylsilane groups (Me-Si-R). Such species have a tendency to adsorb onto the OH-sites on quartz surfaces through a silanization process, which is a possible mechanism for altering the wetting state of quartz.

The NMR signal from the quartz surface was better resolved than the signal originating from the calcite surface. Both surfaces were coated in a layer of water before the crude oil ageing, which induces a positive surface charge on the calcite and a negative surface charge on the quartz [96].

The crude oil used in this thesis is a high acid crude (Grane) and carboxylic acids might be among the adsorbates. Electrostatic adsorption of negatively charged acid head groups onto the positively charged calcite surface would lead to a rigid anchoring of the adsorbates [24]. This rigid arrangement might increase the linewidth sufficiently to suppress the low intensity signals seen on the quartz surface, where electrostatic adsorption is unlikely to occur. Increased magnetic susceptibility in the smaller calcite particles might also contribute to line broadening in the calcite sample.

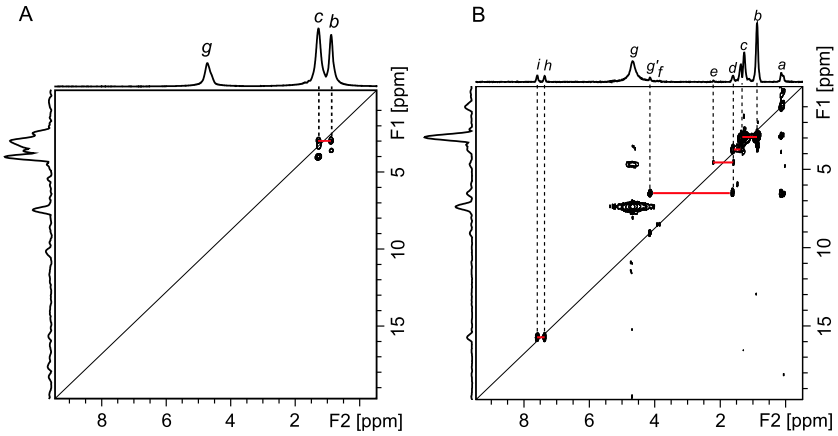

Figure 4.2: ^{1}H-^{1}H DQSQ MAS spectra of the calcite (A) and quartz (B) surfaces after crude oil ageing recorded with a mas rate of 10 KHz.

Figure 4.2 shows the ^{1}H-^{1}H DQSQ MAS spectra from both surfaces. Once again the resolution in the calcite spectrum (Figure 4.2 A) is inferior to the resolution in the quartz spectrum (Figure 4.2 B). The spectrum from the quartz surface shows a pattern that resembles carboxylic acids. Short range couplings are found between methyl (b) and methylene groups (c), between methylene groups and β-protons (d) and between β-protons and α-protons. α and β refers to position with respect to the carbonyl. Such a pattern was not seen on the calcite surface.

4.1.2 Mobility of adsorbed species

The identified species are given in Table 4.1 along with corresponding T_1 relaxation times. T_1 relaxation is most efficient when the correlation time (τ_c) is such that the rate of molecular tumbling equals the Larmor frequency. The T_1 relaxation time will therefore increase as the τ_c both increases and decreases resulting in a U-plot. A long T_1 relaxation time can therefore be an indication of both an ordered (long τ_c) and a disordered (short τ_c) environment [60, 70, 71].

Table 4.1: Identified species, ^{1}H solid state NMR chemical shifts (δ) and spin-lattice (T_1) relaxation times for a-j on calcite (*) and quartz (†) surfaces.

Peak	Species	δ^*[ppm]	T_1 *‡[s]	$\delta^\dagger$[ppm]	$T_1{}^{\dagger‡}$[s]
a	Si-Methyl	-	-	0.17	1.50
b	Methyl	0.92	3.37	0.96	0.382
c	Methylene	1.32	3.35	1.36	0.356
d	β-protons	1.62	-	1.69	-
e	α-protons	-	-	2.21	0.103
f	-	3.91	-	3.94	0.163
g'	-	-	-	4.24	-
g	Water	4.70	1.37	4.70	0.088
h	Aromatic	7.36	-	7.46	-
i	Aromatic	7.64	-	7.68	-
j	Aromatic	8.53	-	8.76	-

* Adsorbate on calcite
† Adsorbate on quartz
‡ T_1 at 298 K

T_1 relaxation times alone are therefore not sufficient in order to characterize the mobility of adsorbed species. However, T_2 relaxation times consistently decrease with an increase in τ_c [60, 71, 70]. Therefore a long T_1 value and a corresponding long T_2 value suggests an unordered environment with high mobility. Alternatively, a long T_1 value and a corresponding short T_2 value suggests an ordered environment with low mobility.

The T_2 relaxation times from a CPMG sequence that averages the signal from the entire sample were recorded and fitted to a three component model. This was performed on static samples during a freeze study to investigate the T_2 value at decreasing temperatures.

On the calcite surface the three components were determined to be surface water (component 1), acid head group adjacent species (component 2) and aliphatic tail species (component 3). The results from the T_2 measurements on the calcite surface are shown in Table 4.2 and the calcite spectra from the freeze study are shown in Figure 4.3 A.

Aliphatic tail species on the calcite surface had long T_1 values ($\approx$ 3.3 s) and long T_2 values ($>$ 1 s). This coincides with an environment with a high mobility, which corresponds well with the theory of electrostatic adsorption on the calcite surface. If the head groups are rigidly bound to the surface the aliphatic tail will have increased mobility as it is pointing away from the surface.

Table 4.2: Temperature (T), T_2 relaxation time and signal fraction (F) for component 1 (surface water), 2 (acid head-group adjacent species) and 3 (aliphatic tail species) resulting from a 3-component model fitting analysis of the CPMG results from the 2^{nd} calcite sample.

T [K]	$T_{2\ (1)}$ [ms]	$F_{(1)}$	$T_{2\ (2)}$ [ms]	$F_{(2)}$	$T_{2\ (3)}$ [ms]	$F_{(3)}$
293	2	0.74	52	0.22	2791	0.04
273	1	0.74	43	0.22	2367	0.04
263	2	0.75	46	0.22	1122	0.03
253	2	0.75	46	0.22	1448	0.03
243	1	0.78	38	0.20	1495	0.02
233	2	0.77	37	0.21	3850	0.02

The water on the calcite surface had a long T_1 relaxation time ($\approx$ 1.3 s) and a very short T_2 relaxation time ($<$ 3 ms). This suggests an ordered environment with low mobility. Figure 4.3 A shows that the water remained

liquid for temperatures down to 233 K. Freezing would result in a major signal loss as the T_2 relaxation time of ice is $\approx 5\ \mu s$ [97]. No freezing suggest that the water is exclusively close to the surface.

On the quartz surface the three components were determined to be surface water (component 1), non-surface water (component 2) and aliphatic species (component 3). The results from the T_2 measurements on the quartz surface are shown in Table 4.3 and the quartz spectra from the freeze are shown in Figure 4.3 B.

The aliphatic species on the quartz surface had similar T_1 and T_2 relaxation times ($\approx$ 400 ms). These are intermediate values and leaves us unable to predict any directional arrangement with respect to the surface.

Table 4.3: Temperature (T), T_2 relaxation time and signal fraction (F) for component 1 (surface water), 2 (non-surface water) and 3 (aliphatic species) resulting from a 3-component model fitting analysis of the CPMG results from the 2^{nd} quartz sample.

T [K]	$T_{2\ (1)}$ [ms]	$F_{(1)}$	$T_{2\ (2)}$ [ms]	$F_{(2)}$	$T_{2\ (3)}$ [ms]	$F_{(3)}$
293	12	0.14	59	0.78	369	0.08
273	16	0.17	52	0.76	423	0.07
263	12	0.10	59	0.81	394	0.09
253	8	0.08	56	0.83	377	0.09
243	5	0.44	74	0.27	313	0.29
233	5	0.39	79	0.3	332	0.31

The water on the quartz surface is present in two different environments, the surface and the non-surface environment. The water exhibits a short T_1 relaxation time and two different T_2 relaxation times. The shortest water T_2 value is $\approx$ 10 ms (surface water) and corresponds to and ordered environment. The highest water T_2 value is $\approx$ 60 ms at T $>$ 253K. The temperature is mentioned here because below 253 K the non-surface water freezes, which caused a major signal loss in figure 4.3 B. After freezing component 2 no longer describes non-surface water and must be considered an unknown.

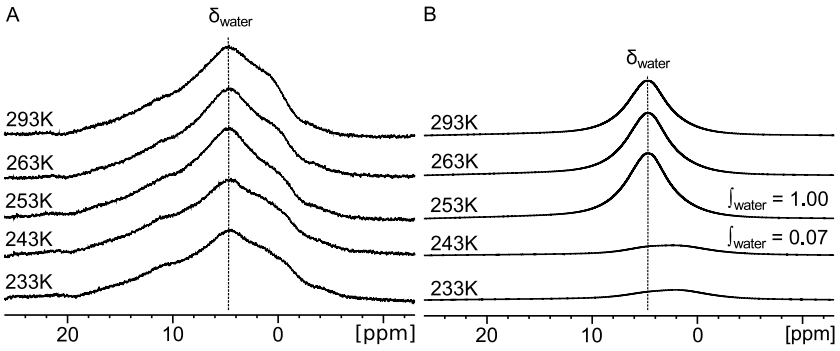

Figure 4.3: ^{1}H NMR spectra of the calcite (A) and quartz (B) surfaces after crude oil ageing at decreasing temperatures. The spectra are recorded with a 90° pulse-acquire sequence using a MAS probe, however the sample rotors were stationary (0 KHz).

Diffusion weighted spectra from the calcite and quartz surfaces are presented in Figure 4.4. Figure 4.4 A shows one diffusivity on the calcite surface suggesting all species are bound to the surface. This is consistent with the relaxation time analysis, which also suggested that adsorbed species are strongly bound to the calcite surface.

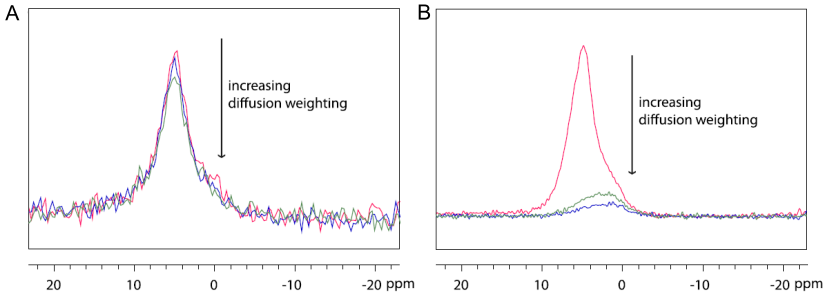

Figure 4.4: Diffusion weighted spectra from the calcite (A) and quartz (B) surfaces after crude oil ageing. The spectra were recorded with a PFGSE sequence. The MAS rotors were placed in a 5 mm NMR tube intended for liquid samples and analysed in a liquid state diffusion probe.

Figure 4.4 B shows two diffusivities on the quartz surface suggesting one rigid environment bound to the surface and one less ordered environment. This is consistent with the relaxation time analysis and the freeze study on the quartz surface, which also suggested several degrees of order on the quartz surface.

The T_1-T_2 correlation plot shown in figure 4.5 A show a single environment at T_1-$T_2 \approx 10$ on the calcite surface. Three different environments at T_1-$T_2 \approx$ 5, 200 and 300 were discovered on the quartz surface (Figure 4.5 B. This strengthens the theory of a single degree of order on the calcite surface and several environments with varying degrees of order on the quartz surface.

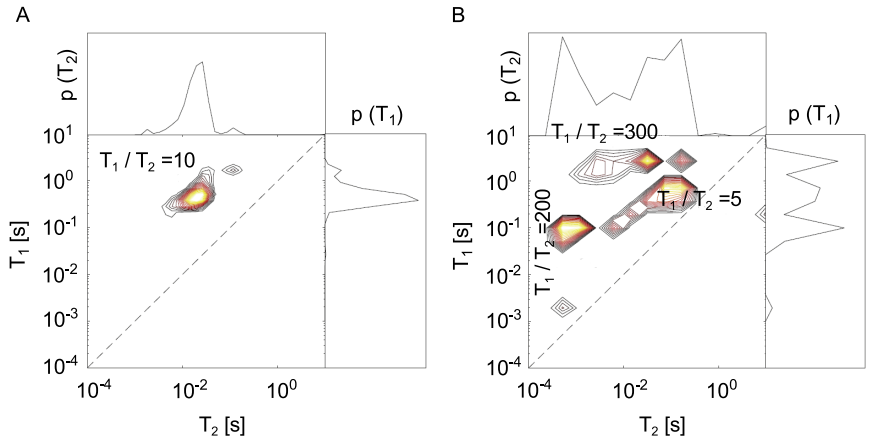

Figure 4.5: T_1-T_2 correlations from the calcite (A) and quartz (B) surfaces. Several degrees of order are observed on the quarts surface, while only one degree of order is observed on the calcite surface.

4.2 Pore scale investigations

Lessons from from papers 1 and 2 were taken into consideration when building the model systems investigated in papers 3 and 4, where the focus was shifted towards pore scale investigations. This section highlights the main results. For validation of methods and other details, the reader is referred to the published papers.

The final objective in the last two papers was to be able to predict wettability in samples with an unknown wetting state based on the fluid distribution in the pore space. The idea was to monitor fluid distribution in model core samples during displacement experiments.

Oil and water signals in porous media are often overlapping, especially at a magnetic field strength of 500 MHz. To be able to distinguish between the NMR signal from oil and water, a pure quartz sand with little or no paramagnetic impurities and an appropriate gain size was used as the rock analogy. If one is able to visualize the oil and water distribution during drainage and imbibition experiments, one might be able to predict wettability.

In paper 3, a pulse sequence able to produce spatially resolved pore size distributions on simple samples saturated with one fluid was created. In this sequence, the pore size distributions were based on correlations between internal gradients and differences in magnetic susceptibility.

In paper 4, the sequence developed in paper 3 was applied on realistic core sample models during various displacement experiments to create fluid specific dimension of confinement (DOC) distributions. The DOC term was coined to replace pore size as a fluid specific DOC only represents a fraction of the pore volume when two fluids are present in the same pore.

The spatial resolution in papers 3 and 4 was achieved through slice selection. Slice selection was chosen instead of frequency encoding because it allows for the recording of an FID. The FID is used in the data processing in papers 3 and 4.

4.2.1 Pore sizes from G_0-$\Delta\chi_{app}$ correlations

An MRI from the sample used to develop the sequence for spatially resolved pore size distributions from G_0-$\Delta\chi_{app}$ correlations is shown in Figure 4.6. The sample consists of two water saturated layers of glass beads with different grain size ranges. The same sample was also used to investigate heterogeneity based on spatially resolved correlations between G_0 and spectral frequency offset intervals (Δf).

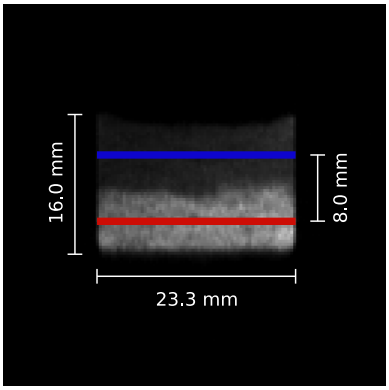

Figure 4.6: MR-image from a water saturated glass bead sample. The top layer has a grain size range of 5-50 μm while the bottom layer has a grain size range of 140 -165 μm.

When determining pore size distributions, the $\Delta\chi_{app}$ term is calculated from the FID time constant (T_2^*). Obtaining spatial resolution through frequency encoding is therefore not an option. The same goes for the $G_0 - \Delta f$ correlations where the frequency offset intervals (Δf) are taken from the spectra resulting from the Fourier transform of the FID. Therefore slice selection was the preferred method for spatial resolution even though it requires one acquisition per slice of interest. Results from all slice selective acquisitions performed in paper 3 from the sample shown in Figure 4.6 were compared to results from non spatially resolved acquisitions taken in samples consisting of the individual layers for validation. The effect of lengthening the sequence by adding a slice selective refocusing pulse in the slice selective sequence, on

the G_0 and the $\Delta\chi_{app}$ terms was investigated. It was found to be very small in the fine grained layer and negligible in the coarse grain layer.

Spatially resolved $G_0 - \Delta\chi_{app}$ correlations are shown in Figure 4.7. There is an obvious difference in the correlation in the two layers. The coarser bottom layer has a wider range in both G_0 and $\Delta\chi_{app}$ and the slope is significantly less steep than the one seen in the fine grained layer. The slope of the correlation is equal to B_0/a, where a is the pore size so the steeper slope in the fine grained sand is reasonable.

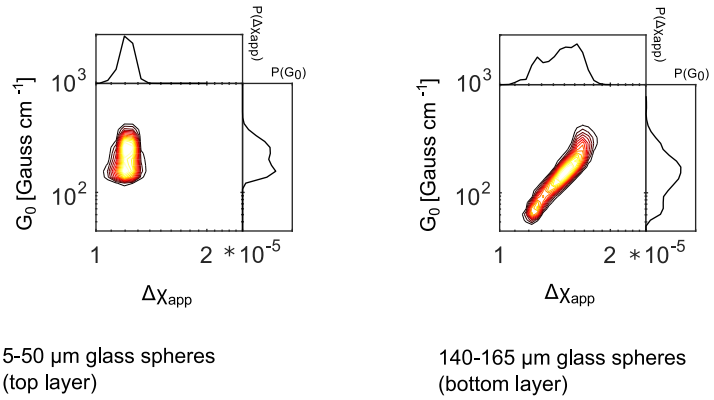

Figure 4.7: Spatially resolved correlations between internal gradient and differences in magnetic susceptibility.

The correlation slope found in Figure 4.7, is used to calculate the pore size distributions shown in Figure 4.8. The distributions clearly delineate between the two layers. The median value in the distribution from the fine grained layer (dotted line) was $\approx 20\ \mu m$, which is reasonable and in good agreement with results we obtained by using the DDIF [43] sequence in samples with the same fine grained glass beads.

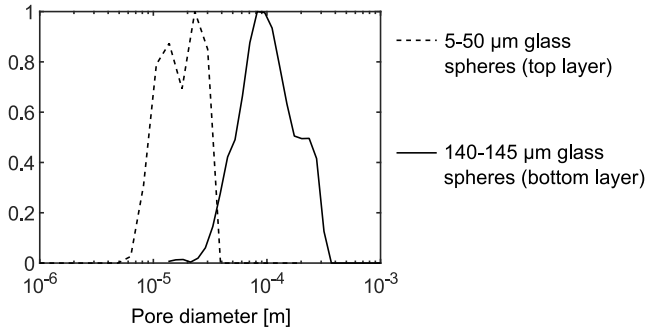

Figure 4.8: Spatially resolved pore size distributions calculated from correlations between internal gradient and differences in magnetic susceptibility.

The median value in the pore size distribution from the coarse grained layer (continuous line) was $\approx 100\ \mu m$. The highest value in the distribution obtained using the DDIF [43] sequence in the same glass beads was approximately 100 μm. This is as expected as the the largest detectable pore sizes using DDIF in water saturated samples is 100 μm. This limitation is caused by the relaxation time [43]. The median value from the DDIF method was $\approx 40\ \mu m$.

In samples with grain sizes ranging from 140 - 165 μm the median pore size value should be $\approx 70\ \mu m$ [98]. In our method we assume a constant gradient across the pore. In larger pores this will no longer be valid and the true pore size distribution in the coarse grained layer is probably somewhere between our method and the results from the DDIF method.

The spatially resolved G_0-Δf correlations from both layers are shown in Figure 4.9. The fine layer is the most heterogeneous layer and there are no apparent correlations between high absolute values of spectral frequency offset intervals and high G_0 values. The more homogeneous coarse grained layer does however exhibit a butterfly pattern where such correlations are present. These results are in agreement with previous non spatially resolved results performed by our research group [91] as well as with computer simulations performed by Burcaw and Callahan [90].

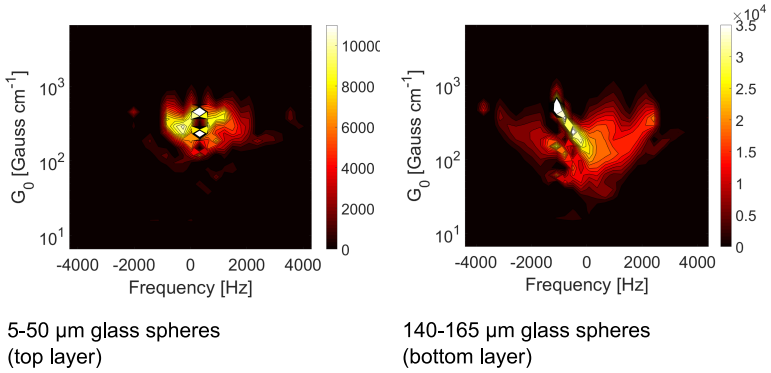

Figure 4.9: Spatially resolved correlation between internal gradient and spectral frequency offset intervals. Note the more pronounced butterfly pattern in the most homogeneous layer (bottom layer).

4.2.2 The dimension of confinement

In the work presented below two samples (one oil-wet and one water-wet) were investigated with MR-images, ^{1}H pulse acquire spectra and with fluid specific dimension of confinement (DOC) distributions. Spatially resolved fluid specific DOC distributions were used to investigate how displacement fronts differ in oil-wet and water-wet samples. Non spatially resolved DOC distribution were used to investigate the difference in fluid distribution between the oil-wet and the water-wet sample at endpoint saturations. MR-images and ^{1}H spectra acquired during displacement experiments allows us to monitor the displacement fronts and the oil and water saturation at various saturation stages during the displacement experiments in the two samples.

DOC distributions provide a length scale for the individual fluids in the sample. The DOC distributions are calculated from $G_0 - \Delta\chi_{app}$ correlations. However, the $\Delta\chi_{app}$ term is calculated from the spectral half width ($\Delta\nu$) instead of the T_2^* (from the FID) value used for the pore size distribution in the previous subsection. The reason for this is that both oil and water is present during the displacement experiments shown in this subsection. Fluid specific results can thus not be obtained from the FID. The model system developed for these displacement experiments consists of very pure quartz sand, practically without paramagnetic impurities. The oil and water peaks are thus distinguishable from each other based on their respective chemical shifts. The spatially resolved DOC distributions shown here are exclusively from the primary oil drive as those yielded the best results. Spatially resolved DOC distributions from the water drives are shown in paper 4.

Figure 4.10 show MR-images and ^{1}H spectra, acquired during the primary oil drive and the primary water drive in the water-wet (A) and the oil-wet (B) samples. The MR-images reveal that the oil drive has a more effective sweep in the oil-wet sample. This is to be expected as the oil will have surface contact in the oil-wet sample. The ^{1}H spectra also shows a higher water retention in the water-wet sample at immobile water saturation ($S_{w,i}$), after the oil drive. This is another indication of a more effective sweep in the oil-wet sample during the primary oil drive.

The MR-images from the water drives clearly show viscous fingering [99, 100] in the oil-wet sample. This is not seen in the water-wet sample where the water has surface contact. The oil retention at residual oil saturation ($S_{o,r}$) is also much higher in the oil-wet sample. This is evident from both the MR-images and the spectra.

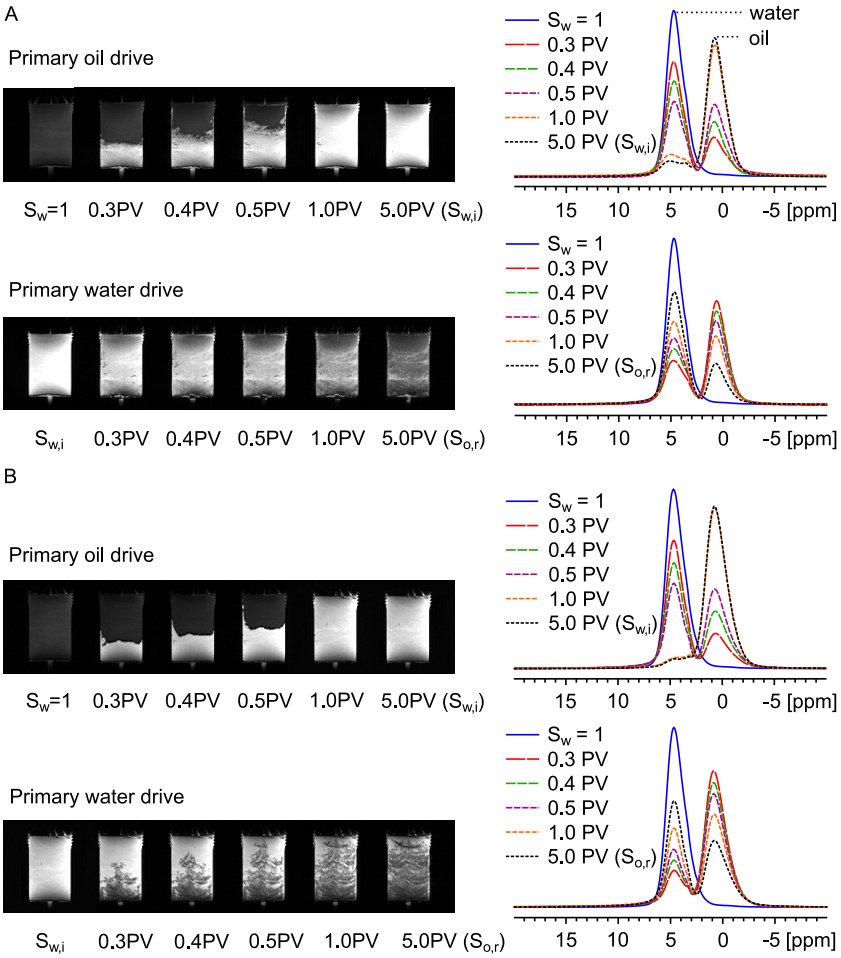

Figure 4.10: Primary oil drive and primary water drive in the water-wet (A) and the oil-wet (B) sample. The displacement fronts are visualized in the MR-images and the spectra shows how the core oil and water saturation changes during the displacement experiments. $S_w = 1$ is is shown in all spectra as a point of reference to the initial conditions where the samples were 100 % water saturated.

Figure 4.11 shows the fluid specific global DOC distributions acquired at end point saturations. Note that the DOC distributions from the water signal at 100 % water saturated samples ($S_w = 1$) are similar, which indicates comparable sample geometry. Also note that the values in the distributions are reasonable values for a pore size distribution in these samples, which they should be at $S_w = 1$.

At $S_{w.i}$ the water signal in the water-wet sample is shifted towards lower values than the water signal in the oil-wet sample. This is to be expected as water at $S_{w,i}$ should be located along surfaces and in small pores in the water-wet sample. It should be located in the middle of large pores in the oil-wet sample which refers to the high value region of the DOC distribution. The oil signal at $S_{w,i}$ is not so straight forward to interpret. It does however, show that a larger fraction of the distribution represents the lower end in the oil-wet sample. This behaviour corresponds the the one seen from the water signal at $S_{w,i}$.

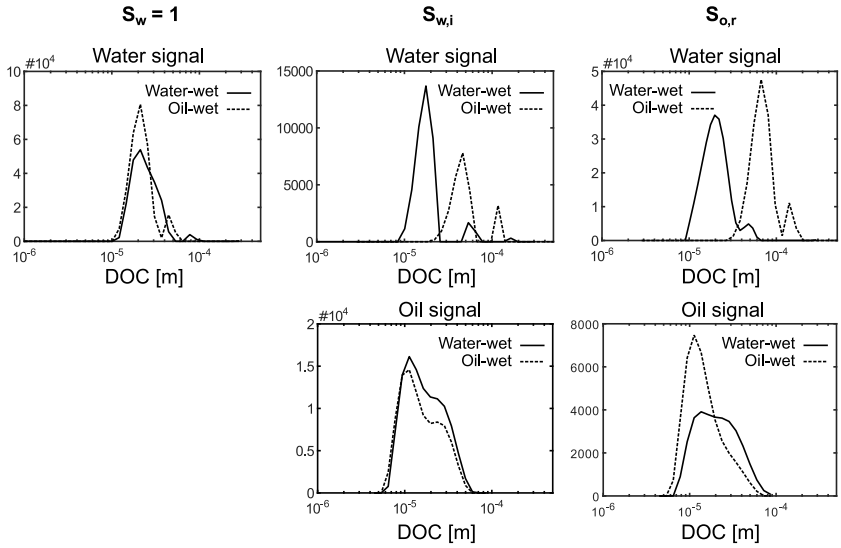

Figure 4.11: Global fluid specific DOC distributions from the water-wet and the oil-wet sample at three endpoint saturations.

At $S_{o,r}$, the water signal from the water-wet sample represents surface water and water in small pores. In the oil-wet sample the water DOC distribution occupies the region representing large pores, which is logical when comparing these results to the viscous fingering observed in Figure 4.10. During water drives in oil-wet samples the water finds paths of least resistance (large pores). At $S_{o,r}$, the oil DOC distributions show that a larger fraction of the distribution is shifted towards the region representing surface access in the oil-wet sample. The results shown in Figure 4.11 are averaged over the entire sample (global) and can on their own determine wettability in such samples.

Figure 4.12 shows the spatially resolved fluid specific DOC distributions used to investigate displacement fronts during the oil drive in the water-wet and the oil-wet sample. Four slices were placed around the front to investigate how the oil moves through the water saturated sample. The same was carried out for the consequent water drives. For those results, readers are referred to paper 4.

The axial slice positioning spans ± 6 mm with respect to the iso centre of the probe, which sums up to a range of 12 mm. Our probe produces a constant field in a 20 mm range (± 10 mm). The top slice (+ 6 mm) is the one that has been the least affected by the displacing oil and the bottom slice (- 6 mm) has been the most affected.

In the water-wet sample the oil enters the largest pores first (+ 6 mm) and as the oil progresses through the sample, the distribution becomes more and more like the one seen for immobile water saturation in Figure 4.11. In the oil-wet sample the oil had not reached the top slice due to a more effective sweep. The least affected slice (+ 2 mm) shows that the oil enters the pore network with surface access and/or with access to the small pores. As for the water-wet sample, the results from the most affected slice resembles the results from the global measurements at $S_{w,i}$ (Figure 4.11.

The fluid spesific water DOC distributions shown in Figure 4.12 was harder to interpret but it is clear that the water in the water-wet sample is more confined than the water in the oil-wet sample. The spatially resolved fluid specific DOC distributions can by themselves indicate wettability.

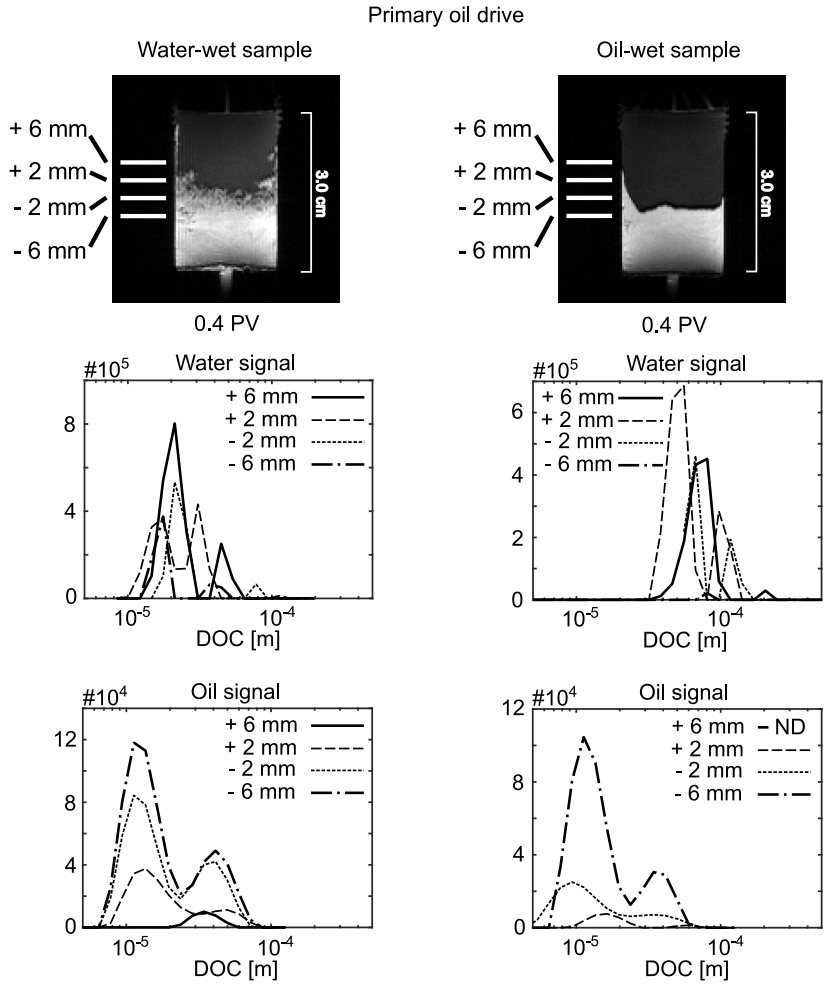

Figure 4.12: Spatially resolved fluid specific DOC distributions from the water-wet and the oil-wet sample during the primary oil drive. The data are recorded from four slices positioned around the displacement front.

Chapter 5

Concluding remarks

This chapter provides conclusions drawn from the research presented in this thesis and offers suggestions for future research.

5.1 Conclusions

High resolution solid state magic angle spinning NMR was found to be a useful analytical tool for investigating species adsorbed onto mineral surfaces. Parameters such as relaxation times, ^{1}H-^{1}H correlations, diffusion measurements and ^{1}H NMR spectra gave new insights into the naturally occurring change in the wetting state of quartz and calcite caused by a wet crude oil ageing. Electrostatic adsorption of carboxylic acids were identified as the main driving force for wettability alteration on the calcite surface. Smaller amounts of carboxylic acids were also found on the quartz surface. On the quartz surface however, the acids did not show any specific anchoring with reference to the surface. Methylsilane groups were identified with anchoring to the quartz surface.

$G_0-\Delta\chi_{app}$ correlations, where $\Delta\chi_{app}$ was calculated from T_2^*, successfully produced pore size distributions in water saturated porous samples (with and without spatial resolution). Spatial resolution was achieved through slice selection and the addition of a slice selective refocusing pulse marginally increases the time from excitation to acquisition. Potential repercussions of this on both G_0 and $\Delta\chi_{app}$ individually was investigated by comparing the results acquired with and without spatial resolution. $G_0 - \Delta f$ plots (with and without spatial resolution) were able to distinguish between two types of particles based on the grain size heterogeneity. The results showed a correlation between high G_0 values and high absolute values of Δf in the most homogeneous sample.

A highly realistic sandstone model system for displacement experiments in high field NMR was successfully developed. The model samples showed petrophysical properties similar to actual sandstone.

$G_0-\Delta\chi_{app}$ correlations, where $\Delta\chi_{app}$ was calculated from the spectral half widths in the separate oil and water peaks, successfully produced fluid specific dimension of confinement (DOC) distributions (with and without spatial resolution). Spatially resolved DOC distributions acquired around displacement fronts provide information regarding the behaviour of the displacing and displaced fluids during displacement experiments. DOC distribution acquired at immobile water saturation and residual oil saturation provide useful information regarding oil and water distribution in the pore space at endpoint saturations. The DOC distributions provided sufficient data for determining wettability in the samples investigated in this study.

The purpose of this project was to link wetting properties on the molec-

ular scale to fluid distribution in porous media at the pore and core sample scale. The firs two papers were intended to provide sufficient information to create a practical and realistic model system for investigating oil and water distribution in porous media during displacement experiments. The model system presented in paper 4 consists of the same quartz sand as the one used in papers 1 and 2. The quartz sand was deemed the most practical to work with and a realistic sand stone model was therefore deemed more feasible than a carbonate model. The silanization process performed to ensure an oil-wet model core sample was inspired by that fact that methylsilane groups were identified on the quartz surface after ageing in paper 1. Valuable lessons from papers 1 and 2 have been implemented in papers 3 and 4.

5.2 Suggestions for future research

Future research should include testing the DOC method, developed in papers 3 and 4, on actual carbonate rocks. As the DOC distributions are calculated from the spectral half widths of the oil and water peaks, it requires a relatively high magnetic field strength to separate them based on chemical shift. This might cause problems in actual sandstones due to the paramagnetic impurities present in such samples. Carbonate rock however, have much less paramagnetic impurities and it would be interesting to see if DOC distributions can provide wetting indications in actual carbonate rocks. That would require developing a core sample holder with sufficient enclosing pressure to flood such samples inside the spectrometer.

Future investigations should also include testing pore size distributions based on $G_0 - \Delta\chi_{app}$ correlations in mono-fluid saturated actual sandstone samples at a low magnetic field strength. A low magnetic field strength investigation would ensure the free diffusion regime and the paramagnetic impurities, present in sandstone, might not have devastating effects.

Bibliography

[1] J. Mitchell, T. C. Chandrasekera, D. J. Holland, L. F. Gladden, and E. J. Fordham. Magnetic resonance imaging in laboratory petrophysical core analysis. *Physics Reports*, 526:165–225, 2013.

[2] E. Amott. Observations relating to the wettability of porous rock. *Petroleum Transactions, AIME*, 216:156–162, 1959.

[3] O. R. Wagner and R. O. Leach. Improving oil displacement efficiency by wettability adjustment. *Petroleum Transactions, AIME*, 216:65–72, 1959.

[4] E. C. Donaldson, R. D. Thomas, and P. B. Lorenz. Wettability determination and its effect on recovery efficiency. *Society of Petroleum Engineers Journal*, pages 13–20, 1969.

[5] M. Muhammed and T. Babadagli. Wettability alteration: A comprehensive review of materials/methods and testing the selected ones on heavy-oil containing oil-wet systems. *Advances in Colloid and Interface Science*, 220:54–77, 2015.

[6] W. G. Anderson. Wettability literature survey - part1: Rock/oil/brine interactions and the effects of core handling on wettability. *Journal of Petroleum Technology*, pages 1125–1144, 1986.

[7] W. G. Anderson. Wettability literature survey - part2: Wettability measurement. *Journal of Petroleum Technology*, pages 1246–1262, 1986.

[8] V. A. Tabrizy, R. Denoyel, and A. Hamouda. Characterization of wettability alteration of calcite, quartz and kolinite: surface energy analysis. *Colloids and Surfaces A*, 384:98–108, 2011.

[9] E. Chukwudeme and A. Hamouda. Oil recovery from polar components (asphaltenes and sa) treated chalk rocks by low salinity water and water containing so_4^{2-} and mg^{2+} at different temperatures. *Colloids and Surfaces A*, 336:174–182, 2009.

[10] N. R. Morrow. Wettability and its effect on oil recovery. *Journal of Petroleum Technology*, 42:1476 – 1484, 1990.

[11] K. A. Rezaei Gomari, R. Denoyel, and A. A. Hamouda. Wettability of calcite and mica modified by different long-chain fatty acids (c_{18} acids). *Journal of Colloid and Interface Science*, 297(2):470–479, 2006.

[12] K. R. Gomari and A. Hamouda. Effect of fatty acids, water composition and ph on the wettability alteration of calcite surfaces. *Journal of Petroleum Science and Engineering*, 50:140–150, 2006.

[13] Y. Wu, P. J. Shuler, M. Blanco, and Y. Tang W. A. Goddard. An experimental study of wetting behaviour and surfactant eor in carbonates with model compounds. *Journal of Petroleum Science and Engineering*, 13:26–34, 2008.

[14] K. Jarrahian, O. Seedi, : Sheykhan, M. V. Sefti, and S. Ayatollahi. Wettability of carbonate rocks by surfactants: a mechanistic study. *Colloids and Surfaces A*, 410:1–10, 2012.

[15] M. Karimi, R. S. Al-Maamari, S. Ayatollahi, and N. Mehranbod. Mechanistic study of wettability alteration oil oil-wet calcite: The effect of magnesium ions in the presence and absence of cationic surfactant. *Colloids and Surfaces A*, 482:403–415, 2015.

[16] K. A. Rezaei Gomari, R. Denoyel, and A. A. Hamouda. Influence of sulfate ions on the interaction between fatty acids and calcite surface. *Colloids and Surfaces A*, 287:29–35, 2006.

[17] F. Bloch, W. W. Hansen, and M. Packard. Nuclear induction. *Physical Review*, 69:127, 1946.

[18] E. M. Purcell, Torrey, and R. V. Pound. Resonance absorbtion by nuclear magnetic moments in a solid. *Physical Review*, 69:37–38, 1946.

[19] R. J. S. Brown and I. Fatt. Measurements of fractional wettability of oil fields' rocks by the nuclear magnetic relaxation method. *Society of Petroleum Engineers*, pages 1–4, 1956.

[20] R. I. Kleinberg and J. A. Jackson. An introduction to the history of nmr well logging. *Concepts in Magnetic Resonance*, 13(6):340–342, 2001.

[21] R. I. Kleinberg. Well logging overview. *Concepts in Magneic Resonance*, 13(6):342–343, 2001.

[22] Z. R. Hinedi, S. Goldberg, A. C. Chang, and J. P. Yesinowski. A ^{31}P and ^{1}H MAS study of phosphate sorption onto calcium carbonate. *Journal of Colloid and Interface Science*, 152:141–160, 1991.

[23] J. P. Yesinowski and M. J. Mobley. ^{19}F MAS-NMR of fluoridated hydroxyapatite surfaces. *Journal of the American Chemical Society*, 105(19):6191–6193, 1983.

[24] C. Totland and R. T. Lewis. Mechanism of calcite wettability alteration by alkyl polyglucoside. *Colloids and Surfaces A*, 488:129–137, 2016.

[25] J. Kumar, I. Fatt, and D. N. Saraf. Nuclear magnetic relaxation time of water in a porous medium with heterogeneous surface wettability. *Journal of Applied Physics*, 40(10):4165–4171, 1969.

[26] C. E. Williams and B. M. Fung. he determination of wettability by hydrocarbons of small particles by deuteron $t_1\rho$ measurement. *Journal of Magnetic Resonance*, 50:71–80, 1982.

[27] W. Hsu, X. Li, and R. W. Flumerfelt. Wettability of porous media by nmr relaxation methods. *the 67th Annual Technical Conference and Exhibition of the Society of Petroleum Engineers*, pages 1027–1037, 1992.

[28] H. S. Gutowsky and G. E. Pake. A nmr technique for the analysis of pore structure: determination of continuous pore size distributions. *Journal of Colloid and Interface Science*, 122:143–153, 1988.

[29] J. J. Howard. Wettability and fluid saturations determined from nmr t_1 distributions. *Magnetic Resonance Imaging*, 12:197–200, 1994.

[30] J. J. Howard. Quantitative estimates of porous media wettability from proton nmr measurements. *Magnetic Resonance Imaging*, 16:529–533, 1998.

[31] M. D. Hürlimann, K. G. Helmer, T. M. De Swiet, P. N. Sen, and C. H. Sotak. Spinechoes in a constant gradient and in the presence of simple restriction. *Journal of Magnetic Resonance*, 113:260–264, 1995.

[32] R. Freedman, N. Heaton, M. Flaum, G.J. Hirasaki, C. Flaum, and M. Hürlimann. Wettability, saturation, and viscosity from nmr measurements. *Society of Petroleum Engineers*, 8:317–327, 2003.

[33] W. Looyestijn and J. Hofman. Wettability index determination bu nuclear magnetic resonance. *SPE Reservoir Evaluation and Engineering*, 9:146–153, 2006.

[34] A. Valori, G. Hursan, and S. Mark Ma. Laboratory and downhole wettability from nmr t_1/t_2 ratio. *Petrophysics*, 58:352–365, 2017.

[35] J. Wang, L. Xiao, G. Liao, Y. Zhang, L. Guo, C. H. Arns, and Z. Sun. Theoretical investigation of heterogeneous wettability in porous media using nmr. *Scientific Reports*, 8:13450, 2018.

[36] C. Liang, L. Xiao, C. Zhou, Y. Zhang, G. Liao, and Z. Jia. Two-dimensional nuclear magnetic resonance method for wettability determination of tight sand. *Magnetic Resonance Imaging*, 56:144–150, 2019.

[37] B. Sun and K. J. Dunn. Probing the internal field gradients of porous media. *Physical Review E*, 65:1–7, May 2002.

[38] H. Y. Carr and E. M. Purcell. Effects of diffusion on free precession in nuclear magnetic resonance experiments. *Physical Review*, 94:630, 1954.

[39] S. Meiboom and D. Gill. Modified spin-echo method for measuring nuclear relaxation times. *The Review of Scientific Instruments*, 29:688, 1958.

[40] J. G. Seland, K. E. Washburn, H. W. Anthonsen, and J. Krane. Correlations between diffusion, internal magnetic field gradients, and transverse relaxation in porous systems containing oil and water. *Physical Review E*, 70:051305, 2004.

[41] Yan Zhang and Bernhard Blümich. $g_{int}^2 d - t_2$ correlation nmr of porous media. *Journal of Magnetic Resonance*, 252:176 – 186, 2015.

[42] A. M. L. Bratland, T. Pavlin, K. Djurhuus, and J. G. Seland. Characterising oil and water in porous media using correlations between-internal magnetic gradient and transverse relaxation time. *Journal of Magnetic Resonance*, 310:106649, 2020.

[43] Y. Song. Determining pore sizes using an internal magnetic field. *Journal of Magnetic Resonance*, 143(2):397–401, 2000.

[44] H. Liu, M. N. d'Eurydice, S. Obruchkov, and P. Galvosas. Determining pore length scales and pore surface relaxivity of rock cores by internal magnetic fields modulation at 2 mhz nmr. *Journal of Magnetic Resonance*, 246:110–118, 2014.

[45] R. T. Lewis, K. Djurhuus, and J. G. Seland. Characterising oil and water in porous media using decay due to diffusion in the internal field. *Journal of Magnetic Resonance*, 259:1–9, 2015.

[46] Y. Zhang, L. Xiao, and G. Liao. Spatially resolved pore size - t_2 correlations for low field nmr. *Microporous and Mesoporous Materials*, 269:142–147, 2018.

[47] H. N. Sørgård, Christian Totland, Willy Nerdal, and J. G. Seland. Crude oil adsorbates on calcite and quartz surfaces investigated by nmr spectroscopy. *The Journal of Physical Chemistry*, 121:20892–20899, 2017.

[48] H. N. Sørgård, Christian Totland, Willy Nerdal, and J. G. Seland. Investigating mobility of crude oil adsorbates on mineral surfaces by nmr. *Magnetic Resonance Imaging*, 56:86–89, 2019.

[49] H. N. Sørgård and J. G. Seland. Investigating pore geometry in heterogeneous porous samples using spatially resolved $G_0 - \Delta\chi_{app}$ and $G_0 - \Delta\nu$ correlations. *Journal of Magnetic Resonance*, 301:40–48, 2019.

[50] H. N. Sørgård and J. G. Seland. A fluid specific dimension of confinement as a measure of wettability in porous media. *Journal of Magnetic Resonance*, 310:106663, 2020.

[51] J. Mitchell. Rapid measurements of heterogeneity in sandstones using low-field nuclear magnetic resonance. *Journal of Magnetic Resonance*, 240:52 – 60, 2014.

[52] L. E. Drain. The broadening of magnetic resonance lines due to field inhomogeneities in powdered samples. *Proceedings of the Physical Society*, 80(6):1380 – 1382, 1962.

[53] A. B. Zolotukhin and J. Ursin. *Introduction to petroleum reservoir engineering*. Norwegian Academic Press, Kristiansund, 2014.

[54] R. C. Selley. *Elements of petroleum geology (second edition)*. Academic Press, 1998.

[55] J. G. Speight. *The chemistry and technology of petroleum*. CRC-Press, Boca Raton, 2007.

[56] M. A. Fernø, M. Torsvik, S. Haugland, and A. Graue. Dynamic laboratory wettability alteration. *Energy and Fuels*, 24:3950–3958, 2010.

[57] H. Friebolin. *Basic one- and two-dimensional NMR Spectroscopy*. Wiley-VCH, Wienheim, 2011.

[58] H. Günther. *NMR spectroscopy: basic prinsiples, concepts and aplications in chemistry*. Wiley-WCH, Weinheim, 2013.

[59] L. G. Hanson. Is quantum mechanics necessary for understanding magnetic resonance? *Concepts in Magnetic Resonance Part A*, 32A:329–340, 2008.

[60] P. T. Callaghan. *Principles of nuclear magnetic resonance microscopy*. Oxford University Press, Oxford, 1991.

[61] M. H. Levitt. *Spin dynamics: Basics of nuclear magnetic resonance*. Wiley, New York, 2002.

[62] F. Bloch. Nuclear induction. *Physical Review*, 70:460–474, 1946.

[63] J. Mitchel, T. C. Chandrasekera, M. L. Johns, L. F. Gladden, and E. J. Fordham. Nuclear magnetic resonance relaxation and diffusion in the presence of internal gradients: The effect of magnetic field strength. *Physical Review E*, 81:026101, 2010.

[64] J. W. Hennel and J. Klinowski. Magic-angle spinning: A historical perspective. *Topics in Current Chemistry*, 246:1–14, 2005.

[65] E. R. Andrew, A. Bradbury, and R. G. Eades. Nuclear magnetic resonance spectra from a crystal rotated at high speed. *Nature*, 182:1659, 1958.

[66] E. R. Andrew, A. Bradbury, and R. G. Eades. Removal of dipolar broadening of nuclear magnetic resonance spectra of solids by specimen rotation. *Nature*, 183:1802–1803, 1959.

[67] E. R. Andrew, A. Bradbury, R. G. Eades, and G. J. Jenks. Fine structure of the nuclear magnetic resonance spectra of solids: Chemical shift structure of the spectrum of phosphorus pentachloride. *Nature*, 188:1096–1097, 1960.

[68] I. J. Lowe. Removal of dipolar broadening of nuclear magnetic resonance spectra of solids by specimen rotation. *Physical Review Letters*, 2:285–287, 1959.

[69] H. Kessemeier and R. E. Norberg. Pulsed nuclear magnetic resonance in rotating solids. *Physical Review*, 155:321–340, 1967.

[70] C. L. Cooper, T. Cosgrove, J. S. van Duijneveldt, M. Murray, and S. W. Prescott. The use of solvent relaxation nmr to study colloidal suspensions. *Soft Matter*, 9(30):7211–7228, 2013.

[71] K. R. Keshari and D. M. Wilson. Chemistry and biochemistry of ^{13}c hyperpolarized magnetic resonance using dynamic nuclear polarization. *Chemical Society Reviews*, 43(5):1627–1659, 2014.

[72] J. Dumez. Spatial encoding and spatial selection methods in high-resolution nmr spectroscopy. *Progress in Nuclear Magnetic Resonance Spectroscopy*, 109:101–134, 2018.

[73] M. L. Lipton. *Totally accessible MRI.* Springer, New York, 2008.

[74] S. Berger. Nmr techniques employing selective radiofrequency pulses in combination with pulsed field gradients. *Journal of Progress in Nuclear Magnetic Resonance Spectroscopy*, 30:137–156, 1997.

[75] R. Freeman. Shaped radiofrequency pulses in high resolution nmr. *Journal of Progress in Nuclear Magnetic Resonance Spectroscopy*, 32:59–106, 1998.

[76] P. Mansfield and P. K. Grannell. Nmr 'diffraction' in solids? *Journal of Physics C: Solid State Physics*, 6:L422, 1973.

[77] R. Brown. A brief account of microscopical observations made in the months of june, july and august 1827, on the particles contained in the pollen of plants; and on the general existence of active molecules in organic and inorganic bodies. *Philosophical magazime series 2*, 4:161–173, 1828.

[78] A. Einstein. Uber die von der molekularkinetischen theorie der warme geforderte bewegung von in ruhenden flussigkeiten suspendierten teilchen. *Annalen der Physik*, 17:549–560, 1905.

[79] A. Einstein. *Investigations on the theory of the Brownian movement.* Dover Publications, Inc, 1956.

[80] J. Crank. *The mathematics of diffusion.* Oxford University Press, Oxford, 1975.

[81] E. O. Stejskal and J. E. Tanner. Spin diffusion measurements: Spinechoes in the presence of a time-dependent field gradient. *The Journal of Chemical Physics*, 42:288–292, 1965.

[82] J. E. Tanner. Use of the stimulated echo in nmr diffusion studies. *The Journal of Chemical Physics*, 52(5):2523–2526, 1970.

[83] M. D. Hürlimann. Effective gradients in porous media due to susceptibility differences. *Journal of Magnetic Resonance*, 131(2):232–240, 1998.

[84] P. Le Doussal and P. N. Sen. Decay of nuclear magnetization by diffusion in a parabolic magnetic field: An exactly solvable model. *Physical Review B*, 46:3465–3485, 1992.

[85] T. M. de Swiet and P. N. Sen. Decay of nuclear magnetization by bounded diffusion in a constant field gradient. *The Journal of Chemical Physics*, 100:5597, 1994.

[86] J. Mitchel, T. C. Chandrasekera, and L. F. Gladden. Obtaining true transverse relaxation time distributions in high-field nmr measurements of saturated porous media: Removing the influence of internal gradients. *Journal of Chemical Physics*, 132:244705, 2010.

[87] J. Mitchell, T. C. Chandrasekera, and L. F. Gladden. Measurement of the true transverse nuclear magnetic resonance relaxation in the presence of field gradients. *The Journal of Chemical Physics*, 139:074205, 2013.

[88] J. Mitchell and T. C. Chandrasekera. Understanding generalized inversions of nuclear magnetic resonance transverse relaxation time in porous media. *The Journal of Chemical Physics*, 141:224201, 2014.

[89] R. T. Lewis and J. G. Seland. Characterization of pore geometry using correlations between magnetic field and internal gradient. *Microporous and Mesoporous Materials*, 269:31 – 34, 2018.

[90] Lauren M. Burcaw and Paul T. Callaghan. Correlation of the inhomogeneous field as a measure of sample heterogeneity. *Journal of Magnetic Resonance*, 216:144 – 151, 2012.

[91] J. G. Seland. Dynamic correlations between inhomogeneous magnetic fields, internal gradients, diffusion and transverse relaxation, as a probe for pore geometry and heterogeneity. *diffusion-fundamentals.org*, 22(10):1–5, 2014.

[92] A. S. Wexler and J. H. Seinfeld. Second-generation inorganic aerosol model. *Atmospheric Environment Part A*, 25(12):2731–2748, 1991.

[93] E. L. Hahn. Spin echoes. *Physical Review*, 80:580, 1950.

[94] Y. Song, L. Venkataramanan, M. D. Hürlimann, M. Flaum, P. Frulla, and C. Straley. t_1-t_2 correlation spectra obtained using a fast two-dimensional laplace inversion. *Journal of Magnetic Resonance*, 154:261–268, 2002.

[95] S. Berger. Pulsed field gradient stimulated echo methods for improved nmr diffusion measurements in heterogeneous systems. *Journal of Magnetic Resonance*, 83:252–266, 1989.

[96] L. L. Schramm, K. Mannhardt, and J. J. Novosad. Electrokinetic properties of reservoir rock particles. *Colloids and Surfaces*, 55:309–331, 1991.

[97] T. Ishizaki, M. Maruyama, Y. Furukawa, and J. Dash. Premelting of ice in porous silica glass. *Journal of Crystal Growth*, 163:455–460, 1996.

[98] G. C. Barker and A. Mehta. Vibrated powders: structure, correlations and dynamics. *Physical Review A*, 45(2):3435–3446, 1992.

[99] P. G. Saffman and G. Taylor. The penetration of a fluid into a porous medium or hele-shaw cell containing a more viscous fluid. *Proceedings of the Royal Society A*, 245:312–329, 1958.

[100] H. E. L. Rose and M. M. Britton. Magnetic resonance imaging of reaction-driven viscous fingering in a packed bed. *Mircoporous and Mesoporous Materials*, 178:64–68, 2013.

I

Paper 1

Crude oil adsorbates on calcite and quartz surfaces investigated by NMR spectroscopy

Paper 2

Investigating mobility of crude oil adsorbates on mineral surfaces by NMR

II

Magnetic Resonance Imaging 56 (2019) 86–89

Contents lists available at ScienceDirect

Magnetic Resonance Imaging

journal homepage: www.elsevier.com/locate/mri

Original contribution

Investigating mobility of crude oil adsorbates on mineral surfaces by NMR

Henrik N. Sørgård, Christian Totland, Willy Nerdal, John Georg Seland*

Department of Chemistry, University of Bergen, Allegaten 41, Bergen N-5007, Norway

ARTICLE INFO

Keywords:
Nuclear magnetic resonance
Relaxation
Diffusion
Crude oil
Adsorption

ABSTRACT

We have applied diffusion and relaxation Nuclear Magnetic Resonance experiments to investigate the translational and rotational mobility of adsorbents on quartz and calcite mineral surfaces. On both surfaces it was found that water is the dominant molecule. On the quartz surface the majority of water molecules have a relatively high degree of both rotational and translational mobility, while a minor fraction of water molecules, and all hydrocarbon molecules, have a significantly lower mobility. On the calcite surface the translational mobility is very low for all the adsorbed molecules, while there is a large diversity in rotational mobility, indicating that the hydrocarbon molecules are strongly attached to the surface, but that some part of each molecule still have a large degree of rotational mobility. Diffusion and relaxation experiments give a detailed description of both the molecular mobility of adsorbed species on these mineral surfaces, which leads to new insight with respect to aging processes on a molecular level.

1. Introduction

Synthetical wettability alteration through enhanced oil recovery methods requires a detailed understanding of the mechanisms responsible for this process. It also requires insight into the naturally occurring process of altering the originally water-wet reservoir rock toward more oil-wet. This natural phenomenon begins when oil migrates into the reservoir pore network and replaces parts of the water fraction, a process known as primary drainage. Adsorption of polar components from crude oil onto reservoir rock surfaces is considered to be an important mechanism for the naturally occurring change in wetting properties from water-wet to more oil-wet.

Adsorption of different acids from acid/decane model oils onto calcite surfaces of varying specific surface areas has previously been researched in detail [1-4]. However, in order to further understand petroleum reservoir processes, it is necessary to obtain a detailed understanding of more realistic systems. The complex composition of crude oil can make contributions to an aging process that cannot be mimicked by a model oil. In a previous study from our group [5], solid state Magic Angle Spinning (MAS) Nuclear Magnetic Resonance (NMR) spectroscopy was used to identify the molecular structure and investigate the arrangement of molecules from a high acid crude oil adsorbed onto calcite and quartz surfaces. These minerals are among the most commonly encountered in petroleum reservoirs. It is generally accepted that only a third of the petroleum in known reservoirs is economically recoverable with established technology [6]. Understanding aging processes on a molecular level will aid in designing more effective methods for enhanced oil recovery.

In the current study, we have performed static (non-spinning sample) diffusion and relaxation experiments to investigate the mobility of the adsorbents on the surface of the same samples as used in the solid state MAS experiments described above [5]. We show that the combination of solid state MAS and static diffusion/relaxation NMR experiments results in a detailed description of both the molecular structure and mobility of adsorbed species on these mineral surfaces, which leads to new insight with respect to aging processes on a molecular level.

2. Experimental

2.1. Sample preparation

Precipitated calcium carbonate crystals from the BioUltra series (≥99.0%), produced by Sigma-Aldrich, were used as the calcite model. The calcium carbonate powder has a specific surface area of 0.99 $m^2 g^{-1}$. NC4X quartz crystals, produced by The Quartz Corp, were a generous gift from Equinor ASA. The quartz sand has a specific surface area of 0.089 $m^2 g^{-1}$. The crude oil sample used for aging of both surfaces originates from a sandstone reservoir n the Norwegian continental shelf (Grane field). The oil has a density of 0.93 g cm^{-3}, an API gravity of 20, and a total acid number (TAN) of 2.0 mg KOH g^{-1}. The asphaltene content is low.

* Corresponding author.
E-mail address: john.seland@uib.no (J.G. Seland).

https://doi.org/10.1016/j.mri.2018.10.002
Received 31 August 2018; Received in revised form 30 September 2018; Accepted 6 October 2018

Details of the sample preparation can be found in Ref. [5], so only a brief description is given here. Dry powder was placed in a humidity chamber along with a saturated K_2SO_4 solution for 14 days. This condition gives a humidity of 97%, which produces a thin film of water on the surface of the powder. This surface pretreatment has previously shown to increase the efficiency of fatty acid adsorption from model oils on calcite surface by nearly 100% [7]. The powder was then placed in 50 g Grane crude oil for an aging period of 24 h(80 °C) under constant stirring. The suspension was centrifuged and the powder was separated from the supernatant. Excess crude oil was removed from the powder surface by dispersing it in decane, decaline and heptane. The powder was left to dry in a fume hood over night and then packed in a 4 mm MAS rotor. After obtaining solid state NMR data, which was presented [5], the MAS rotors were placed inside 5 mm NMR tubes, followed by diffusion and relaxation experiments.

2.2. NMR experiments

All NMR experiments were performed at 25 °C on a Bruker AVIII 500WB spectrometer, using a commercial probe from Bruker Biospin (DiffBB). Diffusion experiments were performed using the 13-interval bipolar sequence [8]. The diffusion time was 20 ms, the sine-shaped gradient pulse length was 0.8 ms, and the gradient strength was varied linearly between 0 and 16 T m^{-1} in 32 steps. Correlations between the longitudinal (T_1) and transverse (T_2) relaxation times were measured using a combined Inversion-Recovery - Carr-Purcell-Meiboom-Gills (IR-CPMG) sequence. The inversion time was varied in 32 steps between 1 ms and 15 s, and the CPMG echoes were collected with an echo time of 0.2 ms and a total of 10,240 echoes. The obtained diffusion data was analysed using Topspin 3.5 and Dynamics Center 2.2 from Bruker Biospin. The $T_1 - T_2$ correlation data was analysed using 2D-ILT software [9].

3. Results and discussion

3.1. Diffusion

NMR spectra from the quartz and calcite samples at different diffusion weighting are shown in Fig. 1. In the quartz sample (Fig. 1a) there are two signals with different diffusivities. The main signal is located at 4.7 ppm, corresponding to the chemical shift of water. A quantitative diffusion analysis reveal that the main signal has a diffusion coefficient of $1.0 \cdot 10^{-9}\,m^2\,s^{-1}$. The other minor signal is observed at higher diffusion weighting and is located at 2–3 ppm, which corresponds to the chemical shift for the aliphatic chain ($-(CH_2)_n - CH_3$) in hydrocarbons. This signal has a diffusion coefficient of $5.0 \cdot 10^{-11}\,m^2\,s^{-1}$. These diffusivities indicate a relatively high translational mobility.

In the calcite sample (Fig. 1 b) there is only one signal, and the spectra obtained at different diffusion weighting indicate a very low diffusivity. A quantitative diffusion analysis reveal that this signal has a diffusion coefficient of $3.0 \cdot 10^{-15}\,m^2\,s^{-1}$, and thus it has very low translational mobility. It should be noted that the diffusional signal decay was relatively low in this analysis, leading to a high degree of uncertainty in the diffusion coefficient, and this value should thus be considered as an upper limit.

These results correspond very well with our previously obtained solid state MAS NMR results on these samples [5], which showed that water is the dominant adsorbent on both surfaces, with fractions of respectively 0.92 and 0.75 for quartz and calcite surfaces. Furthermore, spectra obtained at decreasing temperatures revealed that a significant fraction of water on the quartz surface freezes at 243 K, indicating that these water molecules are not strongly confined to the surface [10], and thus have higher mobility (Fig. 9 in Ref. [5]). The remaining, broader signal, is located around 2–3 ppm, which is the same position as in our diffusion weighted spectra. The corresponding NMR spectra from the calcite surface at decreasing temperatures (Fig. 6 in Ref. [5]) did not show the same phase transition for any of the adsorbed molecules, indicating that all molecules are strongly confined to the surface [10], and thus a low translational mobility of all surface species.

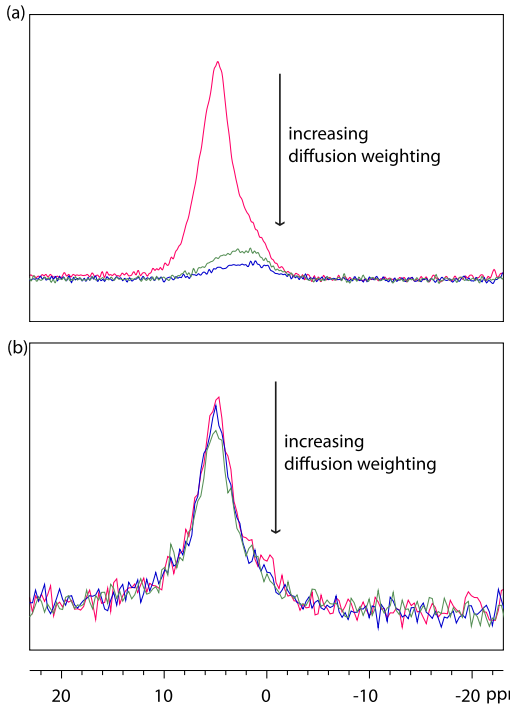

Fig. 1. NMR spectra from the quartz (a) and calcite (b) sample at different diffusion weighting. Diffusion b-factors ($s^2\,m^{-1}$): $2.67 \cdot 10^9$, $2.84 \cdot 10^{12}$, $6.75 \cdot 10^{13}$.

3.2. Relaxation

The results from the relaxation measurements were interpreted using a simplified qualitative version of Bloembergen-Purcell-Pound (BPP) theory [11]. For highly mobile liquids, where the correlation time is short, the system is in the motional narrowing limit, and the two relaxation times are very similar. T_1 becomes longer than T_2 when the mobility is very low and the correlation time becomes very long. The obtained $T_1 - T_2$ correlations are presented in Fig. 2. In the quartz sample (Fig. 2a), there is one main signal with $T_1 \approx 400$ ms and $T_2 \approx 40$ ms, resulting in $T_1/T_2 \approx 10$. This indicate a relative moderate rotational mobility for the main part of the adsorbed molecules. In the lower part of the signal $T_1/T_2 \approx 40$, indicating a lower rotational mobility for some molecules. This is in correspondence with the results from the diffusion analysis on this sample, where two fractions with different translational mobilities were detected.

In the calcite sample (Fig. 2b) the $T_1 - T_2$ correlation is very different, with a large range of both T_1 and T_2 values. Part of the signal is located relatively close to the diagonal, with $T_1 \approx 700$ ms and $T_2 \approx 150$ ms, resulting in $T_1/T_2 \approx 5$. This indicate a relatively high rotational mobility for the molecules that give rise to this signal. This observation seems not to be in agreement with the results obtained in the diffusion analysis, that indicated that all molecules have a very low translational mobility. However, it is possible that even though the

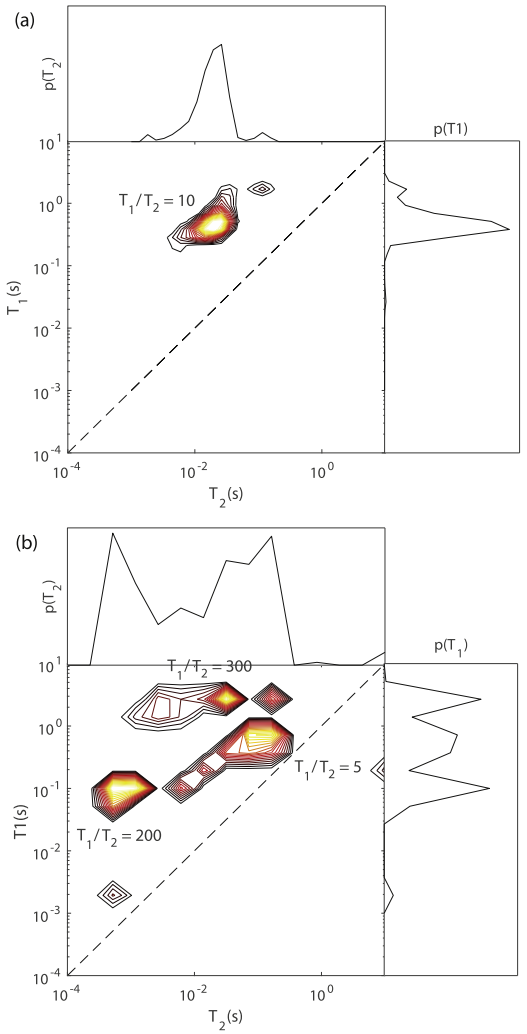

Fig. 2. $T_1 - T_2$ correlations obtained in the quartz (a) and calcite (b) samples. The dotted line indicates the diagonal where $T_1 = T_2$.

molecules have a low translational mobility, the rotational mobility can be relatively high, but this detail should be followed up in future studies. Another part of the signal is located at $T_1 \approx 100$ ms and $T_2 = 0.5$ ms, resulting in $T_1/T_2 \approx 200$. This indicate a relatively low rotational mobility for these adsorbed molecules. The last part of the signal is located at $T_1 \approx 2700$ ms and $T_2 = 10$ ms, resulting in $T_1/T_2 \approx 300$, indicating a very low rotational mobility. These two fractions of adsorbed molecules, having T_1/T_2 in the range of 200–300, correspond well with the results obtained in the diffusion analysis.

In our previous study [5], T_1 was measured in solid state MAS NMR experiments, which makes it possible to determine T_1 for the different chemical species in a chemical shift resolved spectrum. In addition, T_2-measurements were performed on static samples. In the quartz sample, it was found that water had a T_1 of around 100 ms, and the hydrocarbon signals had T_1-values in the range 100 to 1500 ms. The T_2-measurements revealed 3 components, having values of 12 ms (surface water), 60 ms (non-surface water), and 370 ms (hydrocarbons), and with relative fractions of respectively 0.14, 0.78 and 0.08. This range of T_1 and T_2-values correspond well with the values found in the same range in Fig. 2a.

For the calcite sample, it was found that water had a T_1 of around 1400 ms, and the hydrocarbon signals had a T_1-value of approximately 3400 ms. The T_2-measurements revealed 3 components, having values of 2 ms (surface water), 60 ms (acid headgroup), and 370 ms (aliphatic part of hydrocarbon chain), and with relative fractions of respectively 0.74, 0.22 and 0.04. This corresponds to the signals found above $T_1 = 1000$ ms in Fig. 2 b. However, there are also a significant amount of signal found below $T_1 = 1000$ ms, which was not observed in the solid state MAS NMR experiments. We do not know the reason for this discrepancy, but this will be a focus in future investigations of these type of samples in our research group.

3.3. Mobility of adsorbed molecules

In our previous study [5], it was concluded that on the quartz surface adsorbed hydrocarbon acid molecules are totally dissolved in a relatively thick layer of water molecules. On the calcite surface the adsorbed hydrocarbon acid molecules are electrostatically attached to the calcite surface, with the polar head group orientated toward the surface in an relatively thin inner layer of water molecules in close contact with the surface. The diffusion and relaxation data obtained in the current study supports these conclusions, but also gives an additional insight to the translational and rotational mobility of the adsorbed molecules. On the quartz surface the majority of water molecules seems to have a relatively high degree of both rotational and translational mobility, while a minor fraction of water molecules, and all hydrocarbon molecules, have a significantly lower mobility. On the calcite surface the translational mobility is very low for all the adsorbed molecules, while there is a large diversity in rotational mobility, indicating that the hydrocarbon molecules are strongly attached to the surface, but that some part of each molecule still have a large degree of rotational mobility.

4. Conclusion

We have shown that diffusion and relaxation NMR experiments gives a detailed description of the translational and rotational mobility of water and hydrocarbon molecules adsorbed on quartz and calcite mineral surfaces. The results show that the mobility of adsorbed molecules is very different on the two surfaces, indicating a significant difference in adsorption mechanisms. On the quartz surface, all molecules have a high rotational and translational mobility, indicating that molecules are relatively weakly adsorbed on this surface. On the calcite surface the translational mobility is very low for all the adsorbed molecules, while there is a broad range in rotational mobility, indicating that the hydrocarbon molecules are strongly attached to the surface, while each molecule still have a reasonably large degree of rotational mobility. Diffusion and relaxation experiments clearly give a new insight with respect to aging processes on a molecular level that may occur on these mineral surfaces.

Acknowledgments

The authors acknowledge theResearch Council of Norway for support through the Norwegian NMR Platform, (226244/F50), and Equinor ASA for funding the project “Wetting in porous media” through the AKADEMIA agreement.

References

[1] Wu Y, Shuler P J, Blanco M, Tang Y, Goddard W A. An experimental study of

wetting behavior and surfactant EOR in carbonates with model compounds. Soc Pet Eng J 2008;13(01):26–34.
[2] Gomari K R, Hamouda A. Effect of fatty acids, water composition and ph on the wettability alteration of calcite surface. J Pet Sci Eng 2006;50(2):140–50.
[3] Gomari KR, Denoyel R, Hamouda A. Wettability of calcite and mica modified by different long-chain fatty acids (c_{18} acids). J Colloid Interface Sci 2006;297(2):470–9.
[4] Totland C, Lewis R T. Mechanism of calcite wettability alteration by alkyl polyglucoside. Colloids Surf A 2016;488:129–37.
[5] Sørgård H N, Totland C, Nerdal W, Seland J G. Crude oil adsorbates on calcite and quartz surfaces investigated by NMR spectroscopy. J Phys Chem C 2017;121(38):20892–9.
[6] Hirasaki G J, Miller C A, Puerto M. Recent advances in surfactant EOR. Proc. - SPE An. Tech. Conf. Exhib. Soc. Pet. Eng.; 2008.
[7] Gomari KR, Denoyel R, Hamouda A. Wettability of calcite and mica modified by different long-chain fatty acids (C18 acids). J Colloid Interface Sci 2006;297(2):470–9.
[8] Cotts R M, Cotts R, Hoch M, Sun T, Markert J T, Markert J. Pulsed field gradient stimulated echo methods for improved NMR diffusion measurements in heterogeneous systems. J Magn Reson 1989;83(2):252–66.
[9] Callaghan P T. Provided with courtesy of Paul Callaghan. 2002.
[10] Ishizaki T, Maruyama M, Furukawa Y, Dash J G. Premelting of ice in porous silica glass. J Cryst Growth 1996;163(4):455–60.
[11] Bloembergen N, Purcell E M, Pound R V. Relaxation effects in nuclear magnetic resonance absorption. Phys Rev 1948;73(7):679–712.

Paper 3

Investigating pore geometry in heterogeneous porous samples using spatially resolved $G_0 - \Delta\chi_{app}$ and $G_0 - \Delta\nu$ correlations

III

Journal of Magnetic Resonance 301 (2019) 40–48

Contents lists available at ScienceDirect

Journal of Magnetic Resonance

journal homepage: www.elsevier.com/locate/jmr

Investigating pore geometry in heterogeneous porous samples using spatially resolved $G_0 - \Delta\chi_{app}$ and $G_0 - \Delta\nu$ correlations

Henrik Nicolay Sørgård *, John Georg Seland

University of Bergen, Department of Chemistry, Realfagsbygget, Allgaten 41, N-5007 Bergen, Norway

ARTICLE INFO

Article history:
Received 2 November 2018
Revised 21 February 2019
Accepted 28 February 2019
Available online 1 March 2019

Keywords:
NMR spectroscopy
Pore geometry

ABSTRACT

This study presents a two-dimensional NMR pulse sequence for obtaining spatially resolved correlations between magnetic susceptibility induced internal gradients (G_0), and both the apparent difference in magnetic susceptibility ($\Delta\chi_{app}$) and spectral frequency ($\Delta\nu$). $G_0 - \Delta\chi_{app}$ correlations were utilized to generate spatially resolved pore size distributions, while the $G_0 - \Delta\nu$ correlations were used to additionally evaluate sample heterogeneity. The spatially resolved measurements were performed on a water saturated heterogeneous porous sample which contains one layer of 5–50 μm glass spheres (top layer) and one layer of 140–165 μm glass spheres (bottom layer). The slice selection was validated by applying the pulse sequence on a liquid mineral oil and water sample as well as on the porous sample. The resulting spatially resolved pore size distributions show very good agreement with results from our previously published non slice selective pulse sequence in the 140–165 μm glass spheres and good agreement in the 5–50 μm glass spheres. The $G_0 - \Delta\nu$ correlations correctly indicate a slightly higher degree of heterogeneity in the 5–50 μm glass spheres compared to the 140–165 μm glass spheres.

1. Introduction

Introducing a fluid saturated porous sample to a homogeneous magnetic field B_0, can cause significant gradients to occur in the pore space. Such gradients are induced by the magnetic susceptibility difference $\Delta\chi$, between fluids and the matrix and are commonly named internal gradients G_0 [1–7]. The line broadening $\Delta\nu$, caused by the magnetic susceptibility difference in a porous sample, is related to the free induction decay (FID) time constant T_2^* [4,5,8]. In our samples it is assumed that susceptibility differences dominate T_2^*.

$$\Delta\nu \approx \frac{1}{\pi T_2^*} \approx \frac{\gamma}{2\pi} B_0 \Delta\chi_{app} \tag{1}$$

Apparent magnetic susceptibility difference $\Delta\chi_{app}$ is defined as $\Delta\chi_{app} = C\Delta\chi$, where C is a dimensionless constant which corrects for large local variations in the internal field [5,9]. As a first order approximation, the internal magnetic field B_i, is related to the internal gradient G_0 in a single pore, $\Delta\chi_{app}$ and the pore diameter a [1,3,8]. G_0 is assumed to remain constant over the length of the pore.

$$\nabla B_i \equiv G_0 \approx \frac{B_0 \Delta\chi_{app}}{a} \tag{2}$$

From examining Eq. (2) one can see that $G_0 - \Delta\chi_{app}$ correlations can probe the pore geometry. Our research group recently [8] showed that pore size distributions based on such correlations agree well with those obtained from the well established Decay due to Diffusion in the Internal Field (DDIF) [10] method. However, the DDIF and the $G_0 - \Delta\chi_{app}$ methods do not include spatial resolution which is of interest in porous media where the pore geometry varies across the sample.

Zhang et al. (2018) obtained spatially resolved pore size – T_2 correlations by expanding the DDIF method to include a Carr-Purcell-Meiboom-Gill (CPMG) train with frequency encoding on the resulting echoes in low field NMR [11]. However, the DDIF method is based on a stimulated echo created from three $\pi/2$ pulses. As internal gradients increases proportional to the external magnetic field, so does the rate of diffusion and the decoding time in the DDIF method must therefore be kept very short at high fields to maintain the correct diffusion regime. Refocusing and separating the stimulated echo of interest from the rest of the occurring echoes [12] in the DDIF method, and still remain inside the correct diffusion regime for liquids inside porous samples is therefore problematic at high magnetic field strengths. Spatial resolution through frequency encoding in the DDIF-T_2 method is thus challenging in high field NMR.

* Corresponding author.
E-mail address: Henrik.Sorgard@uib.no (H.N. Sørgård).

https://doi.org/10.1016/j.jmr.2019.02.008
1090-7807/

Sun and Dunn (2002) introduced $G_0^2D - T_2$ correlations through a modified CPMG pulse sequence where G_0^2D was decoded during the first part of the sequence by varying the echo spacing over a constant time period. Zhang and Blümich (2015) extended this sequence to incorporate spatial resolution by frequency encoding the echoes occurring in the second part of the sequence (CPMG train). Zhang and Blümich found it possible to distinguish between oil and water using 2D $G_0^2D - T_2$ maps in glass bead samples.

Through computer simulations, it has been shown [13,14] that the edges of a spectrum (high absolute values of $\Delta\nu$) correspond to more confined liquid molecules. Burcaw and Callahan [14] also showed through experimental data that $G_0 - \Delta\nu$ correlations may be used to predict the degree of heterogeneity in a porous sample.

In this paper we continue our research group's previous work [8,15] and introduce a 2D pulse sequence to obtain slice selective $G_0 - \Delta\chi_{app}$ and $G_0 - \Delta\nu$ correlations, which respectively are used to generate spatially resolved pore size distributions and degree of heterogeneity indications.

2. Materials and methods

2.1. Materials

Four different samples were investigated in this study. Sample 1 consisted of glass spheres with a diameter range of 5–50 μm (Thermo Scientific) while sample 2 consisted of glass spheres with a diameter range of 140–165 μm (Duke Scientific Corp). Sample 3 consisted of two layers with different diameter ranges horizontally divided. The bottom layer contained the 140–165 μm glass spheres and the top layer contained the 5–50 μm glass spheres. All three porous samples were saturated with distilled water. Sample 4 was a liquid sample containing a layer of light mineral oil (Sigma Aldrich) and a layer of distilled water, horizontally divided by the oil–water meniscus. The slice selective sequence (Fig. 1), referred to as sequence 1, was applied to all four samples. However, sample 4 was exclusively used for validation of the slice selection. The previously published [8] non selective pulse sequence, referred to as sequence 2, was applied to samples 1 and 2 for comparisons to the results from sequence 1. The three porous samples were prepared in glass tubes with an outer diameter of 25 mm and were 100% water saturated in a vacuum chamber.

2.2. Method

All NMR experiments were conducted on a Bruker Ascend 500 MHz vertical wide bore spectrometer with a commercial Bruker MicWB40 micro imaging probe. The pulse sequence featured in this paper (sequence 1) is shown schematically in Fig. 1 and is a slice selective version of previous work (sequence 2) published by our research group [8]. The $\frac{\pi}{2}$ and π hard pulses were calibrated to be 44 and 88 μs respectively. G_0^2D is encoded during the time T, where the number n, hard π pulses is varied from 32 to 1 in 32 steps. The decoding time T, is kept constant at 20 ms which means that the time τ' is varied from 0.2685 ms to 9.956 ms as the sequence progresses from 32 to 1 hard π pulses. The number of points (td) in the acquisitions was 2048 with a dwell time (dw) of 5 μs.

The relaxation delay was set to 10 s to ensure full longitudinal relaxation between each acquisition. In sequence 1 the second half of the echo that is refocused by the slice selective π pulse is acquired. In the non spatially resolved version (sequence 2) the second half of the echo occurring after the decoding time T, is acquired (Fig. 1). The gradient strength during the slice selective π pulse was set to $1.4797 * 10^{-4}$ T/m. The slice selective π pulse is a 3 lobe sinc pulse with pulse length = 719 μs, bandwidth = 6300 Hz and pulse power = 4.9 W. These parameters ensures slices with a thickness of 1 mm.

The slice positioning was achieved by varying the center frequency of the slice selective π pulse while keeping all other parameters constant. To probe the geometry of the 5–50 μm glass sphere layer the slice selective π pulse had an offset of −25,200 Hz. This results in a 4 mm upward displacement and this is depicted as a blue slice in Fig. 2. To probe the geometry of the 140–165 μm glass sphere layer the slice selective π pulse had an offset of +25,200 Hz, which results in a 4 mm downward displacement, depicted as a red slice in Fig. 2.

The resulting datasets from sequence 1 and 2 are matrices with FID decay throughout the rows and G_0^2D weighted decay down the columns. $\Delta\chi_{app}$ distributions were generated from 1D Inverse Laplace Transform (ILT) of the first row of the dataset and using Eq. (1). G_0 distributions were generated from 1D ILT of the first column of the datasets and the diffusion constant for water at 25 °C ($D_{H_2O} = 2.3 \cdot 10^{-5}$ cm^2/s).

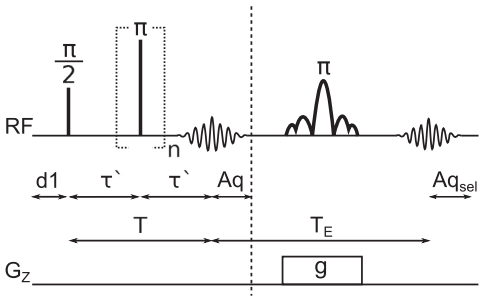

Fig. 1. Pulse sequence (sequence 1) for obtaining spatially resolved correlations between the internal gradient term G_0^2D and either magnetic susceptibility difference $\Delta\chi_{app}$ or frequency $\Delta\nu$. The non spatially resolved version (sequence 2) ends at the dotted line.

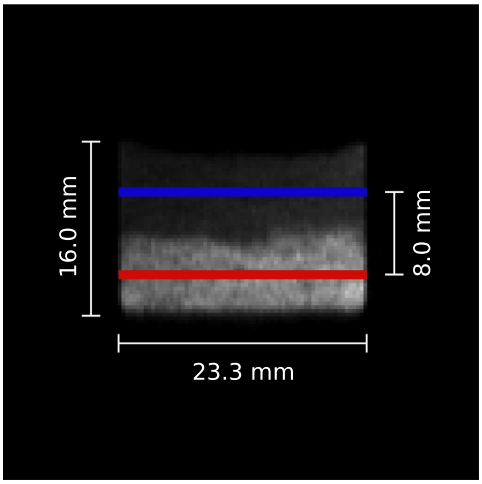

Fig. 2. Magnetic resonance image (MRI) of sample 3 demonstrating the slice position in either the 5–50 μm (blue) or the 140–165 μm (red) layer. The image was recoded in ParaVision using a spin echo acquisition where the echo time was 2.91 ms and the repetition time was 1 s. (For interpretation of the references to colour in this figure legend, the reader is referred to the web version of this article.)

The liquid dynamics in porous samples are restricted by the pore matrix. Hürlimann [1] showed that there are three length scales that are affecting the diffusion term involved with the echo attenuation of the transverse magnetization for a CPMG experiment with n echoes and a constant internal gradient G_0, (Eq. (3)).

$$\frac{M(t_E)}{M(t_E=0)} = e^{-t_E\rho_2\frac{S}{V}-\frac{1}{12}D\gamma^2G_0^2t_E^3} \tag{3}$$

The distance the molecules have to travel in order to dephase 2π radians is called the dephasing length l_g, defined as $l_g = (\frac{2\pi D}{\gamma G_0})^{\frac{1}{3}}$. The diffusion length l_D, is the length a molecule travels due to diffusion during the echo time t_E, defined as $l_D = (Dt_E)^{\frac{1}{2}}$. The final length scale is the structural length l_s, which in our case is the pore length $l_s = a$ [17,16].

If the pore length l_s is the shortest length scale i.e. $l_s \ll l_g$ and l_D, the system will be in the Motional Averaging (MAV) regime. In the MAV regime, the $\Delta\chi_{app}B_0$ term is low and the pore size is typically small. The short pore length means that the diffusing molecules will hit the walls of the pore before complete dephasing during the echo time t_E [16–18]. As the experiments featured in this paper are performed with a relatively high B_0 value and relatively large pore sizes, the MAV regime is not likely to be encountered.

If l_g is the shortest length scale i.e. $l_g \ll l_D$ and l_s, the Localization (LOC) regime applies. In the LOC regime, the $\Delta\chi_{app}B_0$ term is large and the dephasing length l_g, may be very short. Large echo attenuation is observed in such systems, as only the molecules located at a distance of l_g or less from the pore wall will contribute to the echo [16,19,17].

If the diffusion length l_D, is the shortest length scale i.e. $l_D \ll l_g$ and l_s, the system is in the Free Diffusion (FD) regime. The FD regime is valid for samples with large pores where most molecules never experience the pore walls. In this regime, one can expect a moderate internal gradient G_0, during the echo time t_E, and a small echo attenuation [16,17,20]. Because of the high $\Delta\chi_{app}B_0$ value associated with the high B_0 value in our experiments, the water molecules in all our samples are most likely subjected to a regime somewhere in the middle of the FD and the LOC regime during a spin echo acquisition.

Mitchell et al. [21,22] have developed a method for analysing CPMG data in inter-regimental systems. In this method, Eq. (3) is expressed in a general form (Eq. (4)) where b is a constant that describes decay due to diffusion in internal gradient and k describes how the diffusion exponent depends on the echo time.

$$\frac{M(nt_E)}{M(t_E=0)} = e^{-nt_E\rho_2\frac{S}{V}-bnt_E^k} \tag{4}$$

To obtain the true k value, separate CPMG measurements, where the echo time was varied from 0.2 to 3.2 ms, were performed on sample 1 and 2. The resulting diffusion decay was analysed according to Eq. (4) and the data collapse plot according to Hürlimann [1]. As seen in Fig. 3, the optimal k value was determined to be 1.95 and 2.15 for sample 1 and 2 respectively, which indicates that both samples are in between the FD ($k = 3$) and the LOC ($k = 1$) regime.

In Eq. (2), true G_0 assumes that the system occupies the FD regime [16,23]. In our analysis the FD regime was assumed, where $b = \frac{1}{12}D\gamma^2G_0^2$ and $k = 3$, even though both water saturated glass sphere environments exhibits dynamic behaviour from both the FD and LOC regime. Analysis according to the MAV and LOC regime is not performed in this paper, although influences from the LOC regime is discussed later.

To create $G_0 - \Delta\chi_{app}$ correlations the obtained data was analysed as a 2D Fredholm integral according to Eq. (5), where $t_{FID} = td \cdot dw$.

$$M(\tau', t_{FID}) = \iint P(b, T_2^*)e^{-bn\tau'^3}e^{-\frac{t_{FID}}{T_2^*}}dbdT_2^* \tag{5}$$

$G_0 - \Delta\chi_{app}$ correlations were obtained from $P(b, T_2^*)$, where $G_0 = \sqrt{\frac{12b}{D\gamma^2}}$ and $\Delta\chi = \frac{2}{\gamma B_0 T_2^*}$, after a 2D ILT of the obtained data. Pore size distributions were obtained from the measured correlations between G_0 and $\Delta\chi_{app}$ using Eq. (2). To obtain $G_0 - \Delta\nu$ correlations, the data was expressed as a combined ILT and Fourier Transform integral [14] according to Eq. (6).

$$\frac{M(t_\nu, \tau')}{M(0)} = \iint P(\nu, b)e^{-bn\tau'^3}e^{-i\Delta\nu t_\nu}d\nu db \tag{6}$$

Each of the FIDs were Fourier Transformed. The resulting spectra were divided into 32 frequency intervals and 1D ILT was performed on each interval. Assuming the FD regime, as described above, this produces a G_0 distribution for each frequency interval. By assembling all G_0 distributions, a correlation plot between G_0 and $\Delta\nu$ was obtained [15]. All ILT analysis were performed using a software package [24] based on the Schlumberger algorithm [25].

3. Results and discussion

The efficiency of the slice selection was tested by applying sequence 1 to sample 4 (water and a light mineral oil horizontally separated). Fig. 4 A shows a spectrum, acquired with a non spatially resolved one pulse experiment ($\pi/2$-pulse – acquisition) on the liquid water/oil sample, containing both peaks. When the slice selective π pulse is introduced however, only one of the peaks is visible, where each one depends on the center frequency of the slice selective π pulse (Fig. 4B and C). Fig. 4 therefore shows that the slice selection is able to distinguish between water and oil in a two phase liquid sample.

In this paper results from samples 1 and 2 (acquired with both sequence 1 and 2) are compared to results from sample 3 (acquired with sequence 1). Sequence 1 and 2 are applied to sample 1 and 2 to show the effect of introducing a slice selective π pulse while keeping the sample matrix constant and thus eliminating the uncertainty associated with possible variations in packing between samples [26]. Sequence 1 is applied to sample 3 (top layer containing the 5–50 μm glass spheres and bottom layer containing the 140–165 μm glass spheres) to show that the slice selective sequence works in a sample with a heterogeneous geometry.

Lengthening a pulse sequence by increasing the total time from excitation to acquisition may cause significant signal loss. Fig. 5 demonstrates the signal loss associated with the 20 ms decoding time T, present in sequence 1 (in sample 1, 2 and 3) and 2 (in sample 1 and 2) compared to a one pulse ($\pi/2$-pulse – acquisition) experiment. The loss of signal during sequence 1 and 2 is significant compared to the one pulse experiment and predominant in the 5–50 μm glass spheres (Fig. 5A). However, the signal loss associated with the addition of the slice selective pulse in sequence 1 is insignificant as this only increases the total length of the sequence by 770 μs compared to sequence 2.

Fig. 6 shows how the distribution of $\Delta\chi_{app}$ is affected when the length of the pulse sequence is varied from a regular one pulse ($\pi/2$-pulse – acquisition) experiment, to sequence 1 and sequence 2 for both the 5–50 μm (Fig. 6 A) and the 140–165 μm (Fig. 6 B) glass spheres.

It is apparent from Fig. 6 that the 20 ms decoding time T, present in both sequence 1 and 2, is responsible for the loss of higher value $\Delta\chi_{app}$ contributions which are present in the distributions from the one pulse ($\pi/2$-pulse - acquisition) experiment. This effect is evident for both the 5–50 μm (Fig. 6A) and the 140–165

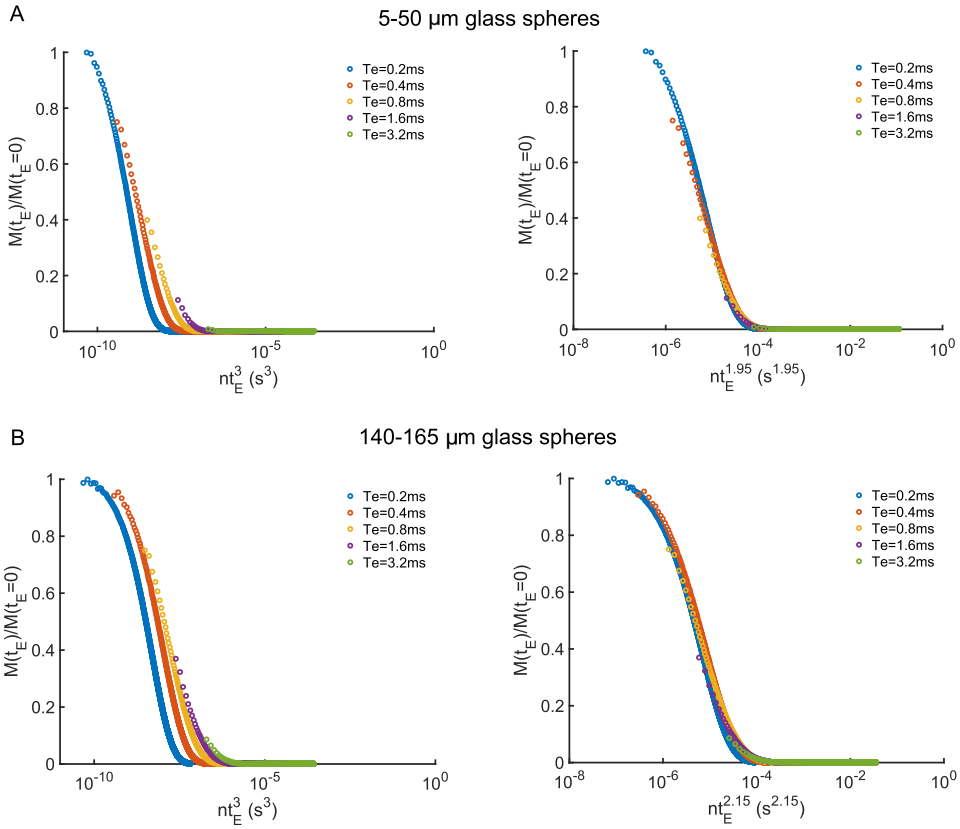

Fig. 3. Normalized diffusion decay plots from CPMG measurements where the echo time is varied from 200 µs to 3.2 ms in samples 1 (A) and 2 (B). The decay curves are plotted according to Eq. (4) with k = 3 (the free diffusion regime) and the optimal *k* value that leads to the data collapse.

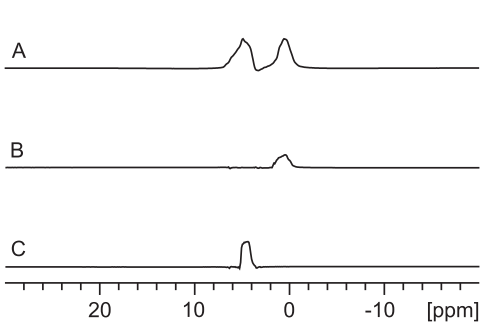

Fig. 4. Spectra, with and without slice selection recorded on a liquid sample containing water and a light mineral oil separated by a meniscus. Without slice selection the spectra contains both the water (most downfield) and the oil (most upfield) signal (A). A −25,200 Hz offset in the center frequency of the slice selective π pulse results in a slice located 4 mm above the iso centre and thus in the oil layer (B). A +25200 Hz offset in the center frequency of the slice selective π pulse results in a slice located 4 mm below the iso centre and thus in the water layer (C).

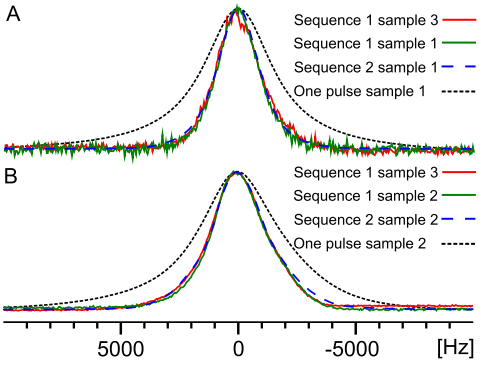

Fig. 5. Spectra from sequence 1 (in sample 1, 2 and 3) and 2 (in sample 1 and 2), obtained from row 1 in the acquired datasets (32 hard π pulses during the 20 ms decoding time T), compared to the spectrum from a regular one pulse (π/2-pulse – acquisition) experiment acquired in the water saturated 5–50 µm (A) and 140–165 µm (B) glass spheres.

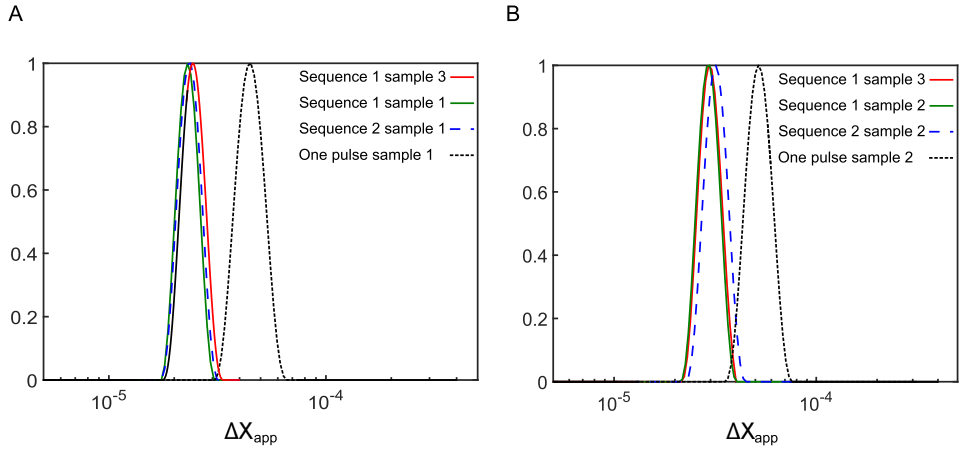

Fig. 6. $\Delta\chi_{app}$, distributions from sequence 1 (in sample 1, 2 and 3) and 2 (in sample 1 and 2), obtained from row 1 of the acquired datasets (32 hard π pulses during the 20 ms decoding time T), compared to the $\Delta\chi_{app}$ distribution from a regular one pulse ($\pi/2$-pulse – acquisition) experiment acquired in the water saturated 5–50 μm (A) and 140–165 μm (B) glass spheres. The distributions are normalized and obtained from 1D ILT of the FIDs and Eq. (1).

μm (Fig. 6B) glass spheres. However, as for the signal loss seen in the spectra shown in Fig. 5, the loss of high value $\Delta\chi_{app}$ contributions (Fig. 6) is predominant in the 5–50 μm glass spheres. Some additional loss of higher value $\Delta\chi_{app}$ contributions was expected for the marginally longer (770 μs) sequence 1, compared to sequence 2. This was seen within sample 1 and 2 for both glass sphere environments. However, the results from sample 3 show that the $\Delta\chi_{app}$ distribution from the top layer of sample 3 have marginally higher $\Delta\chi_{app}$ values than the $\Delta\chi_{app}$ distributions from sample 1 (Fig. 6A). This suggests that the packing of the 5–50 μm glass spheres in the top layer of sample 3 might be slightly different than the packing of the 5–50 μm glass spheres in sample 1. The $\Delta\chi_{app}$ distribution from the bottom layer of sample 3 (sequence 1) was however, close to identical to the one acquired with sequence 1 in sample 2, meaning that the difference in packing of the 140–165 μm glass spheres seems to be insignificant (Fig. 6B).

In Fig. 7, the internal gradient G_0 distributions for the 5–50 μm and 140–165 μm glass spheres are shown for both sequence 1 and 2. In the 5–50 μm glass spheres (Fig. 7A) higher G_0 contributions are lost in sequence 1 (in both sample 1 and 3) compared to sequence 2 (in sample 1). As G_0 is inversely proportional to pore size (Eq. (2)), this effect will cause a bias towards larger pore sizes. The G_0 distributions created from sequence 1 (red and green[1] lines in Fig. 7A) are very similar and the minor differences can be attributed to local variations in the glass sphere packing between sample 1 and 3. On the low G_0 value end, the distributions from all three acquisitions are similar.

In the high value end of the G_0 distributions obtained in the 140–165 μm glass spheres (Fig. 7B), all three G_0 distributions are similar. In the low value end however, the G_0 distribution from sequence 1 (in both sample 2 and 3) have consistently lower values. This effect will also cause a bias towards larger pore sizes.

Fig. 8 shows the $G_0 - \Delta\chi_{app}$ correlation plots from the 5–50 μm (Fig. 8A) and the 140–165 μm (Fig. 8B) glass spheres. For both glass sphere environments, there seems to be a marginal loss in the range of both $\Delta\chi_{app}$ and G_0 between sequence 1 and 2 within samples 1 and 2. This was also observed in Figs. 6 and 7 respectively. There are also small deviations in the correlation plots acquired using sequence 1 in the top layer of sample 3 and the correlation plots acquired using sequence 1 in sample 1. These small deviations are attributed to the difference in packing of the 5–50 μm glass spheres. The correlation plots acquired using sequence 1 in the bottom layer of sample 3 and the ones acquired using sequence 1 in sample 2 are almost identical, which again suggests that the difference in packing is less of a factor in the 140–165 μm glass spheres.

The correlation plots, shown in Fig. 8, can be used as an indication of difference in average pore size between samples. When comparing the correlation slopes from both glass sphere environments one can see that the slopes from the 5–50 μm glass spheres are generally steeper than their counterpart in the 140–165 μm glass spheres. This is reasonable as the $G_0 - \Delta\chi_{app}$ correlation slope is given by B_0/a (Eq. (2)), where a is the pore diameter, meaning that the slope is inversely proportional to pore size and one can thus immediately identify which sample has the coarsest grains. It is also worth mentioning that any deviation from linearity in the slope may be an additional indication of grain heterogeneity, although this must be further researched.

Fig. 9 shows the resulting pore size distributions. In Fig. 9 A the pore size distributions calculated from $G_0 - \Delta\chi_{app}$ correlations obtained from sequence 1, in both sample 1 and the top layer of sample 3, are shown and compared to results from sample 1 generated by sequence 2 and the DDIF method. In Fig. 9B the pore size distributions calculated from $G_0 - \Delta\chi_{app}$ correlations obtained from sequence 1, in both sample 2 and the bottom layer of sample 3, are shown and compared to results from sample 2 generated by sequence 2 and the DDIF method. In the DDIF method, t_e was 150 μs and the t_d was logarithmically varied from 1 ms to 15 s. A comparison to DDIF is provided for both glass sphere environments. However, the maximum detectable pore size using the DDIF method in water saturated samples is approximately 100 μm, limited by the relaxation time [10]. The 140–165 μm glass spheres might have pores larger than 100 μm so the DDIF method should therefore be most accurate in the 5–50 μm glass spheres.

When comparing the pore size distributions created from pulse sequence 1 and 2, the distributions created from sequence 1, in

[1] For interpretation of color in Fig. 7, the reader is referred to the web version of this article.

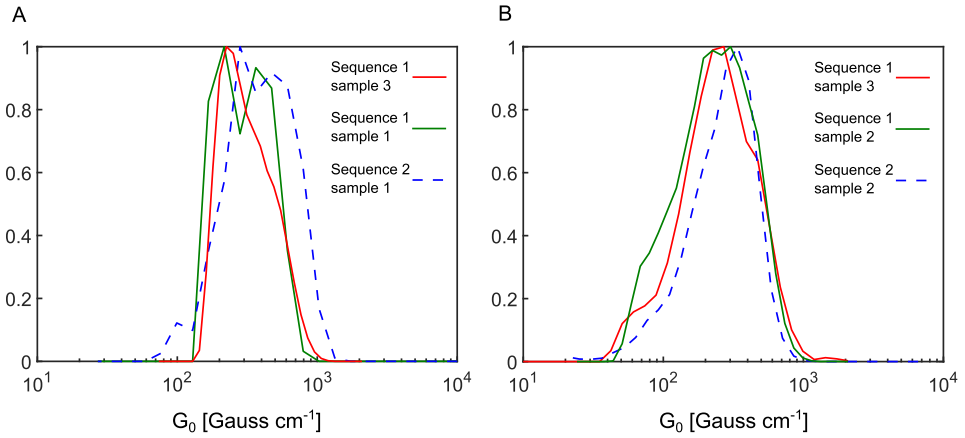

Fig. 7. Internal gradient G_0, distributions from sequence 1 (in sample 1, 2 and 3) and 2 (in sample 1 and 2), acquired in the water saturated 5–50 μm (A) and 140–165 μm (B) glass spheres. The distributions are normalized and were obtained from 1D ILT of the first column of the acquired datasets.

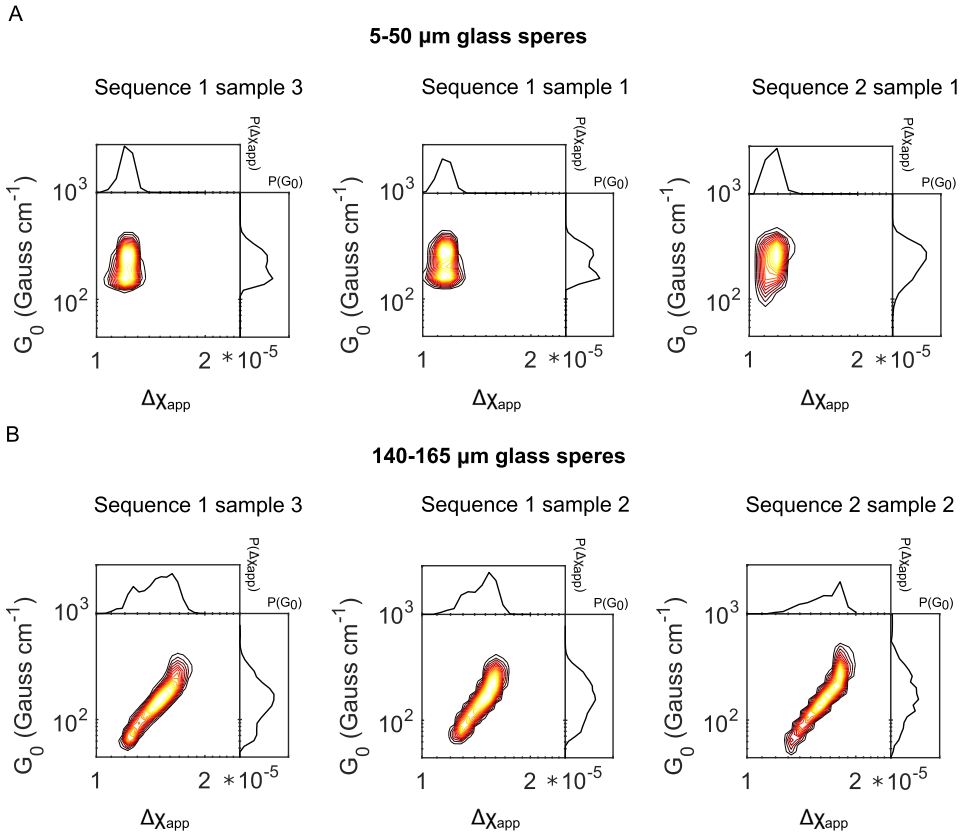

Fig. 8. $G_0 - \Delta\chi_{app}$ correlations from water saturated 5–50 μm (A) and 140–165 μm (B) glass spheres obtained from sequence 1 (in sample 1, 2 and 3) and sequence 2 (in sample 1 and 2).

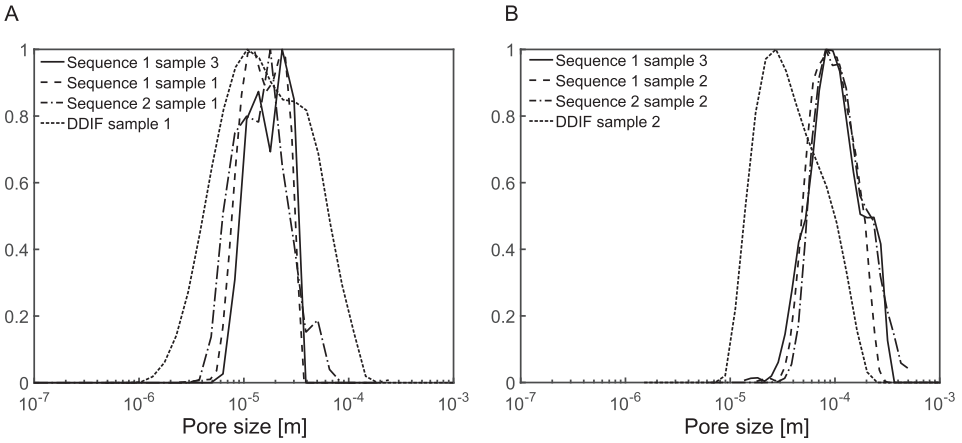

Fig. 9. Pore size distributions from the 5–50 μm glass spheres (A) and the 140–165 μm glass spheres (B) obtained from slice selective and non slice selective $G_0 - \Delta\chi_{app}$ correlations (sequence 1 and 2) as well as the DDIF method.

both sample 1 and 3 (top layer) seem to consistently omit the smallest pores in the 5–50 μm glass spheres (Fig. 9A). This is consistent with the loss of higher G_0 values, seen in Fig. 7A. The highest G_0 values originates from the smallest pores, which means that a loss in high G_0 values may also remove the smallest pores from the pore size distribution. Still, the median values from both of the selective as well as the non selective pore size distributions are approximately 20 μm. This is a reasonable value for the 5–50 μm glass spheres and is in good agreement with the median value from the DDIF method and from previous experiments with the same glass spheres [8]. In the 5–50 μm glass spheres, the DDIF method yielded a pore size ranging from 1 μm to 200 μm while sequence 1 and 2 produced ranges of 3 μm to 40 μm and 3 μm to 100 μm respectively. Since the largest glass spheres have a

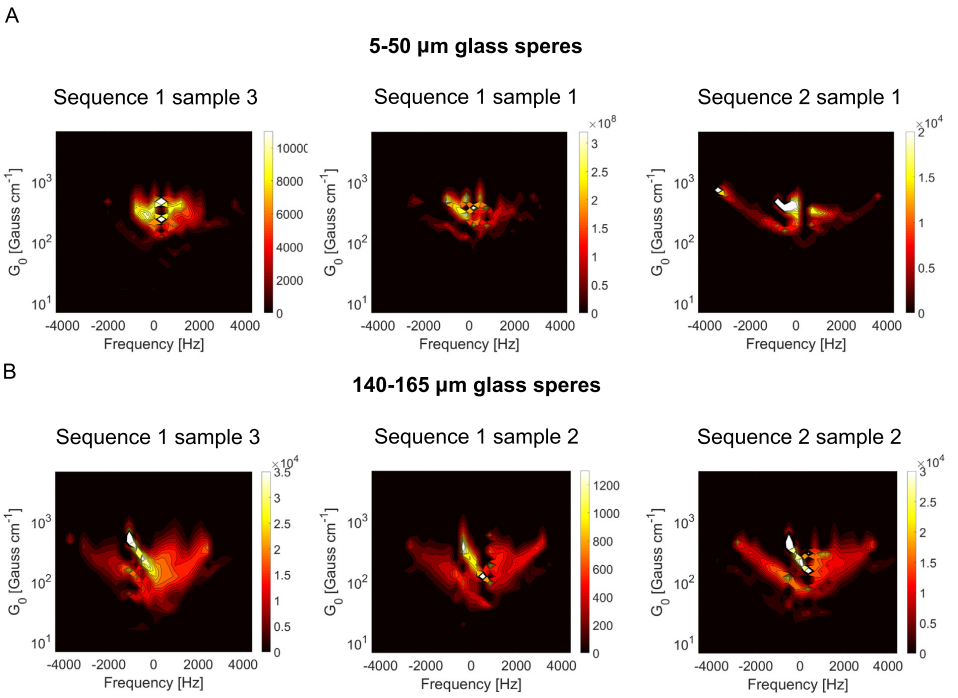

Fig. 10. $G_0 - \Delta\nu$ correlations from water saturated 5–50 μm (A) and 140–165 μm (B) glass spheres obtained from sequence 1 (in sample 1, 2 and 3) and 2 (in sample 1 and 2).

diameter of 50 μm, sequence 1 produced the most correct pore size range.

Fig. 9B shows a very good agreement between the pore size distributions from sequence 1 and sequence 2 in the 140–165 μm glass spheres regardless of sample. The marginal differences in $\Delta\chi_{app}$ (Fig. 6 B) and G_0 Fig. 7B) between the two methods does not seem to significantly affect the resulting pore size distributions. The good agreement between the two samples suggests that the packing of the 140–165 μm glass spheres was similar in samples 2 and 3. Compared to the 5–50 μm glass spheres, the particle size is more homogeneous in the 140–165 μm glass spheres, which means that packing related uncertainty becomes less of a factor in the 140–165 μm glass spheres.

All three distributions created from $G_0 - \Delta\chi_{app}$ correlations have a median value of approximately 100 μm, while the DDIF method provides a median value of approximately 40 μm. In the 140–165 glass spheres, the pore size distribution should have a median value of approximately 70 [27], meaning that the true pore size distribution lies somewhere between the distributions from the $G_0 - \Delta\chi_{app}$ correlations and the one from the DDIF method. In our method, based on $G_0 - \Delta\chi_{app}$ correlations, we assume that G_0 is constant across the length of a pore. In samples, where the pore size is large compared to the diffusion length, the molecules will not experience an average (constant) gradient. The molecules will then be more sensitive to local gradients which varies on a considerably smaller scale than the pore length. Molecules positioned in the middle of the pore, will then experience a gradient that is weaker than the average value across the pore. This effect will lead to an underestimation of G_0 and since G_0 is inversely proportional to the pore size, it will lead to an overestimation of the pore size. Further work should include repetition of these experiments at lower magnetic field strengths to ensure the FD regime and exclude disturbances from molecules in the LOC regime.

Fig. 10 shows the $G_0 - \Delta\nu$ correlations for both the 5–50 μm and the 140–165 μm glass spheres obtained from sequence 1 and 2 (in sample 1, 2 and 3). Burcaw and Callahan [14] suggested that correlations between high G_0 values and high absolute values of frequency are indications of homogeneous samples while a more full G_0 range at all frequencies indicates heterogeneity. The correlation between high G_0 values and high absolute values of frequency, seen in homogeneous samples, should amount to a pattern resembling butterfly wings. A butterfly pattern in the $G_0 - \Delta\nu$ correlation plot indicates a higher degree of homogeneity and these plots can thus be used to determine which of two samples has the most homogeneous/heterogeneous particle size range. In the $G_0 - \Delta\nu$ correlation plots, the butterfly pattern is more predominant for the 140–165 glass spheres (Fig. 10B). This suggest a higher degree of homogeneity in the 140–165 μm glass spheres, compared to the 5–50 μm glass spheres (Fig. 10A), which is reasonable as the 140–165 μm glass spheres has the most narrow particle size range. It is however, worth mentioning that a similar correlation between high G_0 values and high absolute values of frequency was also observed in the $G_0 - \Delta\nu$ correlation obtained from sequence 2 in the 5–50 μm glass spheres.

4. Conclusions

Spatially resolved pore size distributions and $G_0 - \Delta\nu$ correlation maps based on $G_0 - \Delta\chi_{app}$ correlations were successfully created with a slice selective 2D pulse sequence (sequence 1) in both 5–50 μm and 140–165 μm water saturated glass spheres. The results from sequence 1 were compared to results from non spatially resolved $G_0 - \Delta\chi_{app}$ correlations (sequence 2) performed on the same sample to eliminate the uncertainty associated with glass sphere packing. Sequence 1 was additionally applied to a separate two layer sample (sample 3) and the results from both layers were presented as well.

In sample 1 (5–50 μm glass spheres) there is a decent agreement between pore size distributions from sequence 1 and 2. The minor deviation between sequence 1 and 2 was attributed to loss of high value G_0 contributions in sequence 1 caused by the marginally longer length (+770 μs) of this sequence. This effect is only an issue for very small particle environments as it does not manifest itself in the 140–165 μm glass spheres. The distribution acquired using sequence 1 in the top layer (5–50 μm glass spheres) of sample 3 is also in decent agreement with the results from sample 1. The minor deviations between the results from sequence 1 in sample 1 and 3 are attributed to minor differences in glass sphere packing. All three pore size distributions produced a reasonable median value in the 5–50 μm glass spheres.

In sample 2 (140–165 μm glass spheres) the pore size distributions from sequence 1 and 2 are almost identical. The distribution acquired using sequence 1 in the bottom layer (140–165 μm glass spheres) of sample 3 is also in good agreement with the results from sample 2. This suggests that glass sphere packing is less of a factor in the 140–165 μm glass spheres. However, all three pore size distributions from the 140–165 μm glass spheres overestimated the pore size by small margin.

$G_0 - \Delta\nu$ correlation maps were presented and these maps correctly indicated a slightly higher degree of homogeneity in the 140–165 μm glass spheres. Such maps can thus be used to decide which of two samples have the most homogeneous/heterogeneous particle size. As an addition to pore size distributions, spatially resolved $G_0 - \Delta\nu$ correlations may be useful as an indication of heterogeneity.

At the magnetic field strength featured in this paper, the water molecules in both glass sphere environments were subject to a mixture of the LOC and the FD regime. Further work should include repetition of these experiment in low field NMR to ensure the FD regime.

Acknowledgements

The authors acknowledge The Research Council of Norway for support through the Norwegian NMR Platform, NNP (226244/F50) and Equinor ASA for funding the project "Wetting in porous media" through AKADEMIA.

References

[1] M.D. Hürlimann, Effective gradients in porous media due to susceptibility differences, J. Magn. Reson. 131 (2) (1998) 232–240.
[2] B. Sun, K.J. Dunn, Probing the internal field gradients of porous media, Phys. Rev. E 65 (2002) 1–7.
[3] Y. Zhang, B. Blümich, $g_{int}^2 d - t_2$ correlation nmr of porous media, J. Magn. Reson. 252 (2015) 176–186.
[4] J. Kärger, H. Pfeifer, S. Rudtsch, The influence of internal magnetic field gradients on nmr self-diffusion measurements of molecules adsorbed on microporous crystallites, J. Magn. Reson. (1969) 85 (2) (1989) 381–387.
[5] Q. Chen, A.E. Marble, B.G. Colpitts, B.J. Balcom, The internal magnetic field distribution, and single exponential magnetic resonance free induction decay, in rocks, J. Magn. Reson. 175 (2) (2005) 300–308.
[6] P.M. Singer, G. Leu, E.J. Fordham, P.N. Sen, Low magnetic fields for flow propagators in permeable rocks, J. Magn. Reson. 183 (2) (2006) 167–177.
[7] D. Bernin, D. Topgaard, Nmr diffusion and relaxation correlation methods: new insights in heterogeneous materials, Curr. Opin. Colloid Interface Sci. 18 (3) (2013) 166–172.
[8] R.T. Lewis, J.G. Seland, Characterization of pore geometry using correlations between magnetic field and internal gradient, Micropor. Mesopor. Mater. 269 (2018) 31–34.
[9] J. Mitchell, Rapid measurements of heterogeneity in sandstones using low-field nuclear magnetic resonance, J. Magn. Reson. 240 (2014) 52–60.
[10] Y.-Q. Song, Determining pore sizes using an internal magnetic field, J. Magn. Reson. 143 (2) (2000) 397–401.
[11] Y. Zhang, L. Xiao, G. Liao, Spatially resolved pore-size - t2 correlations for low-field nmr, Micropor. Mesopor. Mater. 269 (2018) 142–147.

[12] A. Sodickson, D.G. Cory, A generalized k-space formalism for treating the spatial aspects of a variety of nmr experiments, Prog. Nucl. Magn. Reson. Spectrosc. 33 (2) (1998) 77–108.
[13] B. Audoly, P. Sen, S. Ryu, Y.-Q. Song, Correlation functions for inhomogeneous magnetic field in random media with application to a dense random pack of spheres, J. Magn. Reson. 164 (1) (2003) 154–159.
[14] L.M. Burcaw, P.T. Callaghan, Correlation of the inhomogeneous field as a measure of sample heterogeneity, J. Magn. Reson. 216 (2012) 144–151.
[15] J.G. Seland, Dynamic correlations between inhomogeneous magnetic fields, internal gradients, diffusion and transverse relaxation, as a probe for pore geometry and heterogeneity, diffusion-fundamentals.org 22 (10) (2014) 1–5.
[16] J. Mitchell, T.C. Chandrasekera, M.L. Johns, L.F. Gladden, E.J. Fordham, Nuclear magnetic resonance relaxation and diffusion in the presence of internal gradients: the effect of magnetic field strength, Phys. Rev. E 81 (2010) 026101.
[17] R.T. Lewis, J.G. Seland, A multi-dimensional experiment for characterization of pore structure heterogeneity using nmr, J. Magn. Reson. 263 (2016) 19–32.
[18] M. Hurlimann, K. Helmer, T. Deswiet, P. Sen, Spin echoes in a constant gradient and in the presence of simple restriction.
[19] T.M. de Swiet, P.N. Sen, Decay of nuclear magnetization by bounded diffusion in a constant field gradient, J. Chem. Phys. 100 (8) (1994) 5597–5604.
[20] P. Le Doussal, P.N. Sen, Decay of nuclear magnetization by diffusion in a parabolic magnetic field: an exactly solvable model, Phys. Rev. B 46 (1992) 3465–3485.
[21] J. Mitchell, T.C. Chandrasekera, L.F. Gladden, Measurement of the true transverse nuclear magnetic resonance relaxation in the presence of field gradients, J. Chem. Phys. 139 (7) (2013) 074205.
[22] J. Mitchell, T.C. Chandrasekera, Understanding generalized inversions of nuclear magnetic resonance transverse relaxation time in porous media, J. Chem. Phys. 141 (22) (2014) 224201.
[23] J. Mitchell, T.C. Chandrasekera, L.F. Gladden, Obtaining true transverse relaxation time distributions in high-field nmr measurements of saturated porous media: removing the influence of internal gradients, J. Chem. Phys. 132 (24) (2010) 244705.
[24] Provided by courtesy of Professor Paul T. Callaghan.
[25] L. Venkataramanan, Y.-Q. Song, M.D. Hurlimann, Solving fredholm integrals of the first kind with tensor product structure in 2 and 2.5 dimensions, IEEE Trans. Signal Process. 50 (5) (2002) 1017–1026.
[26] B. Brattekås, T.L. Føyen, T. Vabø, H. Haugland, S.I. Reite, A.S. Saunes, M.A. Fernø, Dos and don'ts when developing a system to investigate spontaneous imbibition in unconsolidated porous media, in: The International Symposium of the Society of Core Analysts held in Trondheim, Norway, 27–30 August 2018.
[27] G.C. Barker, A. Mehta, Vibrated powders: structure, correlations, and dynamics, Phys. Rev. A 45 (1992) 3435–3446.

Paper 4

A fluid specific dimension of confinement as a measure of wettability in porous media

IV

Journal of Magnetic Resonance 310 (2020) 106663

Contents lists available at ScienceDirect

Journal of Magnetic Resonance

journal homepage: www.elsevier.com/locate/jmr

A fluid specific dimension of confinement as a measure of wettability in porous media

Henrik Nicolay Sørgård *, John Georg Seland

University of Bergen, Department of Chemistry, Realfagsbygget, AllÃígaten 41, N-5007 Bergen, Norway

ARTICLE INFO

Article history:
Received 7 October 2019
Revised 23 November 2019
Accepted 26 November 2019
Available online 2 December 2019

Keywords:
NMR spectroscopy
Pore geometry

ABSTRACT

The wettability of a reservoir rock is among the most important factors influencing oil recovery. This study presents how the application of a modified CPMG pulse sequence can determine the wettability of porous samples containing oil and water in the same pore network. This method can be applied as an average of the signal over the entire sample as well as with spatial resolution using slice selection. Correlations between dephasing in internal gradients (G_0^2D) and the spectral linewidth ($\Delta\nu$) were used to calculate a fluid specific dimension of confinement (DOC) distribution for oil and water separately during forced displacement experiments performed inside the bore of an NMR spectrometer. Two samples, one water-wet and one oil-wet, were investigated. Data averaged over the entire sample show oil and water distribution at endpoint saturations ($S_w = 1, S_{w,i}$ and S_{or}) while spatially resolved data show which pores are initially occupied by the displacing fluid as well as the displacing efficiency. Both the data averaged over the entire sample and the spatially resolved data can, by itself, indicate wettability. As opposed to relaxation times as an indirect indication of wettability, the DOC distributions provide a direct fluid dimension, which more carefully describes the distribution of oil and water in the pore network.

1. Introduction

The wettability of a surface describes the relative preference of the surface to be covered by one of several immiscible fluids [1–4]. In petroleum research, these fluids are typically oil and water. The wettability of the reservoir rock surface is one of the most important factors influencing the efficiency of oil recovery [2]. Correctly understanding the wetting conditions of a reservoir at an early stage is therefore of tremendous importance with regards to options for field-development. Incorrect estimations of wetting conditions may result in unexpected dynamic behaviour, incorrect oil-in-place estimates and thus an incorrect economic valuation of the reservoir [4]. It is generally accepted that water floods provide a more efficient sweep in water-wet reservoirs i.e. where water is the wetting phase and oil is located in the middle of the pores [1–3].

On smooth surfaces, wettability is usually determined with contact angle measurements where the angle created between a drop and the surface it rests upon, through the densest phase, determines the wettability of the surface [2]. In reservoir rock, wettability is commonly determined from laboratory experiments, performed on core samples from the reservoir of interest. These laboratory experiments usually involve spontaneous and forced displacement of one fluid by another. The Amott-test [1] and the USBM wettability method [5] are examples of procedures for determining wettability based on such displacement experiments.

Determining wettability using Nuclear Magnetic Resonance (NMR) was introduced in 1956 when Brown and Fatt [6] presented fractional wettability in sand packs as a function of longitudinal (T_1) relaxation times. Their experiments were based on the observation that relaxation times are affected by the surface of the porous media. Longitudinal (T_1) and transverse (T_2) relaxation times in porous media have since then been thoroughly researched using NMR with varying magnetic field strengths [7]. $T_2 - D$ and $T_1 - T_2$ correlations have recently been used as a measure of wettability in porous media saturated with both water and oil. Wang et al. [8] applied $T_2 - D$ and $T_1 - T_2$ correlations to introduce the concept of apparent contact angles in samples with heterogeneous wettability. Liang et al. [9,10] applied $T_2 - D$ and $T_1 - T_2$ correlations to show that the signal from the wetting fluid moves towards shorter T_2 relaxation times as the saturation of the wetting fluid decreases. The method proposed by Liang et al. [9,10] show a good correlation with benchmark results from the Amott method [1].

Introducing a fluid saturated porous sample to a homogeneous magnetic field (B_0) causes significant gradients to occur in the pore

* Corresponding author.
E-mail address: Henrik.Sorgard@uib.no (H.N. Sørgård).

https://doi.org/10.1016/j.jmr.2019.106663
1090-7807/

space. These gradients are commonly named internal gradients (G_0) and are induced by the difference in magnetic susceptibility ($\Delta\chi$) between the solid matrix and fluids occupying the pore space [11–15]. As a first order approximation, the internal gradient G_0 is related to the apparent magnetic susceptibility difference $\Delta\chi_{app}$ and the pore diameter a [11,16].

$$G_0 \approx \frac{B_0 \Delta\chi_{app}}{a}. \quad (1)$$

$\Delta\chi_{app}$ is defined as $\Delta\chi_{app} = C\Delta\chi$ where the dimensionless constant C corrects for large variations in the internal field [17,18]. Sun and Dunn [12] showed that a $G_0^2 D$ term can be measured by implementing a modified 2D CPMG sequence where the number of π-pulses in the echo train is varied over a constant time period. G_0 can thus be calculated if the diffusion coefficient (D) of the fluid is known.

Eq. (1) shows that $G_0 - \Delta\chi_{app}$ correlations may give insights into the pore geometry of porous samples saturated with one fluid. Our research group recently showed that $G_0 - \Delta\chi_{app}$ correlations can produce reliable pore size distributions in water saturated porous samples [19,20]. In those studies $\Delta\chi_{app}$ was calculated from the time constant (T_2^*) of the Free Induction Decay (FID).

$$\Delta\nu \approx \frac{1}{\pi T_2^*} \approx \frac{\gamma}{2\pi} B_0 \Delta\chi_{app}. \quad (2)$$

For a method to be applicable in wettability determination it must be able to indicate fluid distribution of both oil and water when oil and water are simultaneously present in the same pore space. The FID in such an instance will obviously contain signal from both the oil and water. Therefore, one cannot calculate the diameter a of the oil and water separately from the FID time constant (T_2^*) directly. Authors have still been able to separate the oil and water signal based on internal gradient. For instance, Zhang and Blümich were able to distinguish between oil and water in glass bead samples using $G_0^2 D - T_2$ maps [16].

Here, we consider Eq. (1) and Eq. (2), and show that the dimension of one fluid can be determined from a correlation between the spectral line broadening ($\Delta\nu$) and the internal gradient (G_0) (Eq. (3)). Since it is no longer a pore diameter (i.e. there are two fluids present in the pore space) we define it as a dimension of confinement (DOC). A wetting fluid will occupy the surface areas and the small pores, thus maintaining a lower DOC than a non-wetting fluid which will occupy the volume in the middle of large pores. The dimension of confinement provides a length scale as opposed to indirect interpretations of relaxation times or internal gradient measurements and is expressed as

$$DOC \approx \frac{2\pi\Delta\nu}{\gamma G_0}. \quad (3)$$

The spectral line broadening ($\Delta\nu$) is proportional to $\Delta\chi_{app}$ and B_0 (Eq. (2)). Paramagnetic impurities on the surface of a porous matrix may therefore strongly enhance line broadening in high field NMR [7,21].

The core sample models used in this study consists of pure quartz sand practically without paramagnetic impurities on the surface. The line broadening seen in these samples is therefore reduced and the oil and water signal can actually be distinguished based on chemical shift in a spectrometer with a magnetic field (B_0) of 11.7 T. Two model core samples were investigated, one water-wet and one oil-wet (silanized sand). Using correlations between $G_0^2 D$ and $\Delta\nu$, both in spatially resolved measurements and in global measurements averaged over the entire sample, we are able to determine sample wettability based on oil and water dimensions of confinement at various saturation stages during forced displacement experiments.

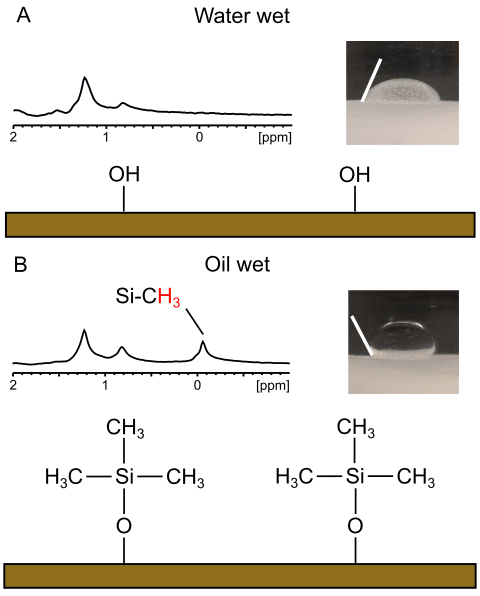

Fig. 1. Schematic of the quartz surface before (A) and after (B) silanization. The NMR spectra are solid state ^{1}H NMR spectra acquired with a MAS rate of 10 kHz. The images show a droplet of water in oil placed on oil saturated sand after 5 min.

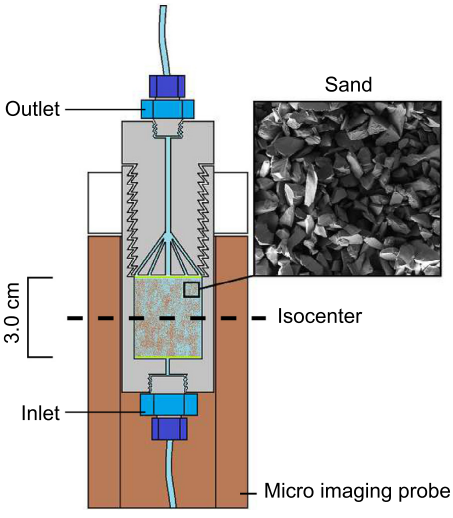

Fig. 2. Non-magnetic fiberglas flow cell created for performing forced displacement experiments inside the NMR spectrometer. The length and internal diameter of the cell are 3.0 and 2.1 cm respectively, which ensures a cell volume $\approx$ 10.4 cm^2 and a pore volume (PV) that depends on the individual sample porosity ϕ.

2. Materials and methods

2.1. Materials

In this study the oil and water phases consisted of a light mineral oil (Sigma Aldrich) and distilled water respectively. The sand used as the reservoir model was the NC4X high purity quartz sand (The Quartz Corp), which has a heterogeneous grain size with a diameter range of approximately 50–260 μm [22]. The ⩾99 puriss trimethylchlorosilane (Sigma Aldrich) and anhydrous, 99% heptane (Sigma Aldrich) was used for the silanization process.

2.2. Sample preparation

Two samples were analysed in this study and both consisted of sand, physically held together in a plexiglas cell. The first sample contained untreated sand and this is the water-wet (WW) sample. The second sample contained treated sand and this is the oil-wet (OW) sample. The oil-wet surface of the treated sand was achieved through a silanization process where the sand was placed in a mixture of trimethylchlorosilane (TMCS) in heptane (5% TMCS by volume) for 25 min at room temperature. The mixture was shaken up every five minutes to ensure that the entire sand surface was exposed to the solution. During this process the TMCS adsorbes to the OH-sites on the quarts surface as shown in Fig. 1. After being exposed to the silanization solution for 25 min, the sand was cleaned with heptane five times to remove excess TMCS and HCl (by product) and left to dry in an open container for 72 h.

The success of this method was evaluated with two methods. The first was solid state ^{1}H NMR of both the untreated and the treated sand. The presence of the strongly shielded methyl protons in TMCS should result in a peak in the vicinity of 0 ppm [23]. Fig. 1 shows that this peak is clearly only present on the treated sand.

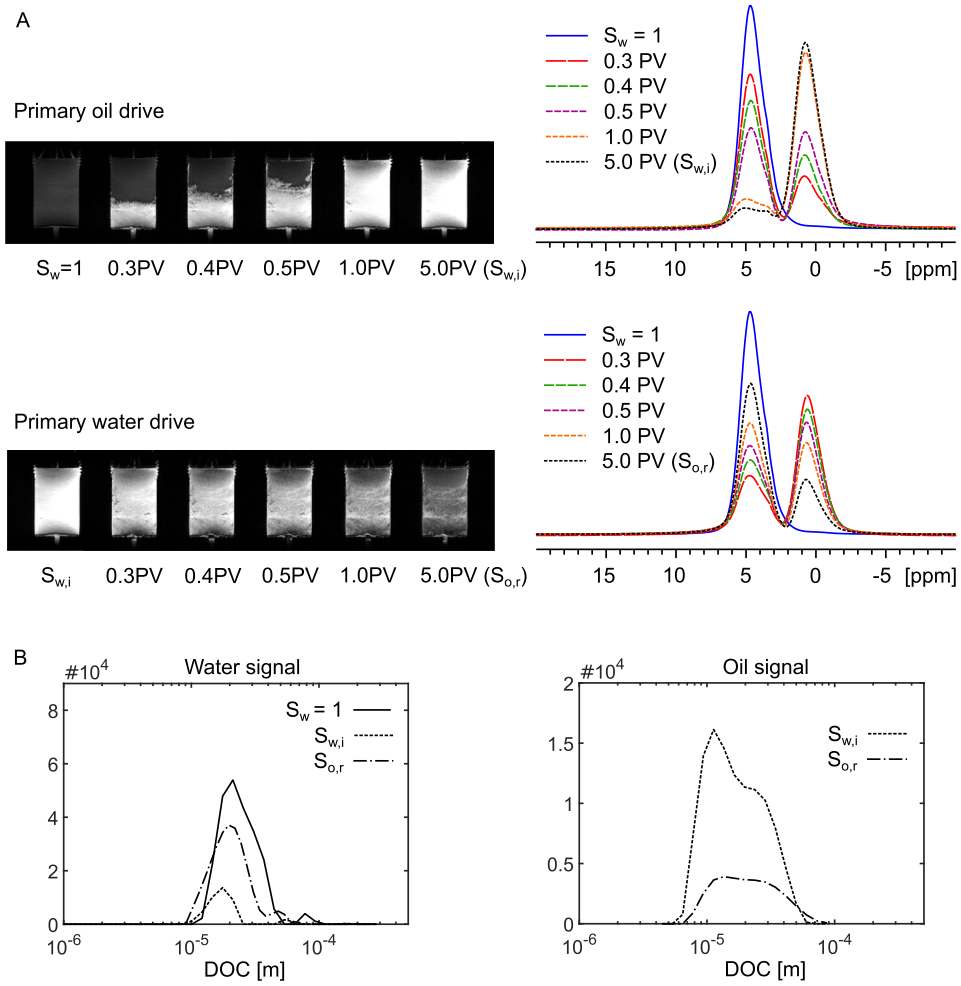

Fig. 3. T_1 weighted magnetic resonance images and global ^{1}H NMR spectra with clearly separated water (most downfield) and oil (most upfield) peaks at various saturation stages during primary oil drive and primary water drive in the water-wet sample (A). Separate global DOC distributions for the water and oil signal acquired at endpoint saturations in the water-wet sample (B).

The other method for evaluating the success of the silanization process was a crude spontaneous imbibition test. The immense water-wet nature of the untreated sand makes it impossible to perform contact angle measurements on the dry untreated sand, as the water droplet simply disappears into the sand. As this is sand, and not a smooth surface, a precise contact angle measurement is also impossible to obtain. Therefore, both sands were placed in separate containers and mineral oil was added to a level of 2 cm above the sand bed. A water droplet was then placed on the oil-saturated sands, thus creating a water in oil system. The water droplets were observed for 20 min. The water droplets in both containers started out with an obtuse contact angle through the densest phase (water) because of the oil present in the sand. However, after five minutes the water droplet on the untreated sand displayed an acute contact angle before it spontaneously imbibed into the sand. The water droplet placed on the treated sand did not change contact angle and showed no signs of spontaneous imbibition over the entire 20 min (Fig. 1). The solid state ^{1}H NMR spectra from the dry sands and the spontaneous imbibition test proves the more oil-wet nature of the treated sand.

The non-magnetic flooding cell, created from plastic and fiberglas, is depicted in Fig. 2. The two model core samples were created using the same packing procedure. The sand was placed in the cell and to avoid loss of sand during flooding, two filters (one paper and one plastic) were placed at the in- and outlet. The cell is designed to avoid loss of structural integrity in the pore network during flooding. This is achieved by screwing the outlet into the sand and thus compressing it with mechanical force. The porosity ϕ, was found to be 42% and 43% for the water-wet and oil-wet model core samples respectively. This suggest that there is a comparable pore network in the two samples.

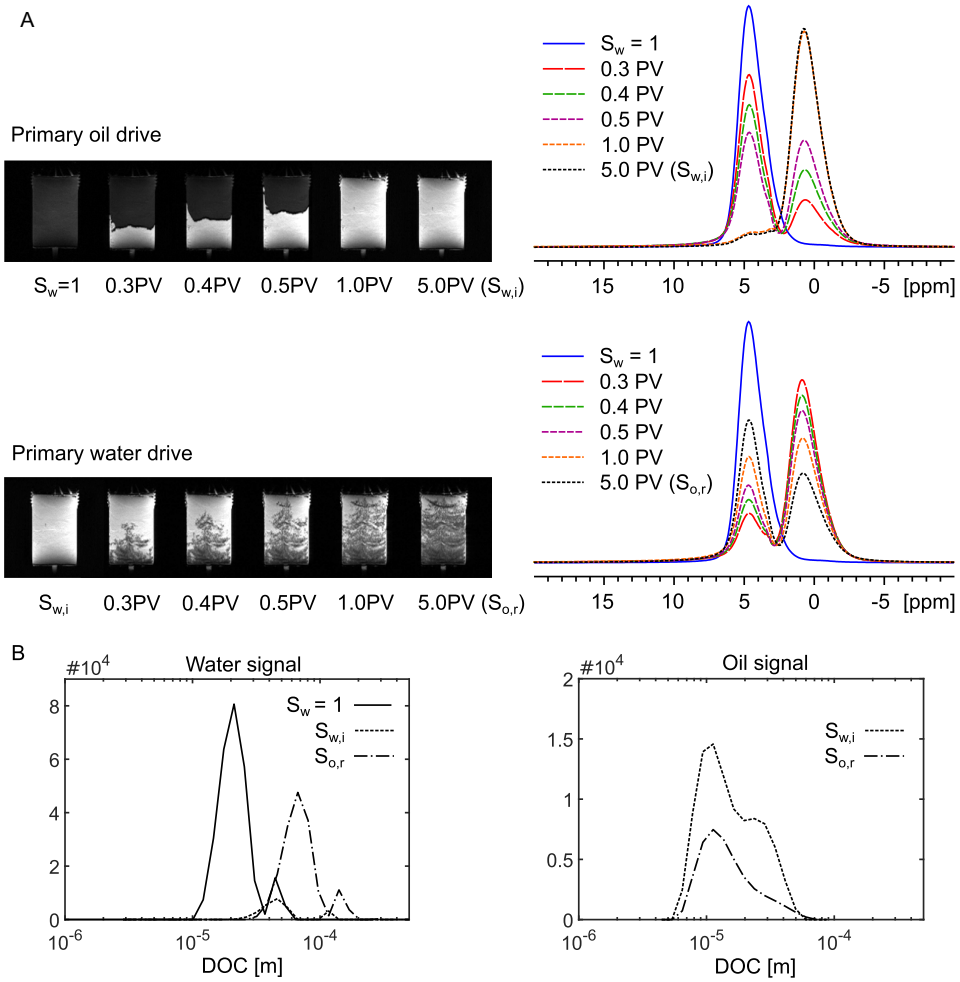

Fig. 4. T_1 weighted magnetic resonance images and global ^{1}H NMR spectra with clearly separated water (most downfield) and oil (most upfield) peaks at various saturation stages during primary oil drive and primary water drive in the oil-wet sample (A). Separate global DOC distributions for the water and oil signal acquired at endpoint saturations in the oil-wet sample (B).

2.3. Drainage and imbibition experiments

The drainage and imbibition experiments were performed inside the bore of the NMR spectrometer so that NMR data could be acquired without moving the sample at various saturation stages. The terms drainage and imbibition are defined as the displacement of the wetting and non-wetting phase respectively [24]. Thus, a primary displacement of water by oil in a 100% water saturated sample is a primary drainage for a water-wet sample, but it is a primary imbibition for an oil-wet sample. This can be confusing when comparing two samples with different wetting conditions and therefore this paper uses the terms oil drive and water drive for simplicity. During displacements experiments, the fluids were pumped through tubing and consequently through the core sample models with a Nexus 5000 syringe pump at a rate of 30 ml/h.

Both samples (WW and OW) went through a primary oil drive and a subsequent primary water drive. The displacement experiments began at 100% water saturated samples ($S_w = 1$). Then oil was injected until the samples were considered to be at immobile water saturation ($S_{w,i}$). Thereafter, water was injected until the samples were considered to be at residual oil saturation ($S_{o,r}$). $S_{w,i}$ and $S_{o,r}$ were determined to occur after five pore volumes of the displacing fluid had been injected. During all displacement experiments NMR data were acquired at several intermediate saturation stages (0.3PV, 0.4PV, 0.5PV and 1.0PV) in addition to at the endpoints ($S_w = 1, S_{w,i}$ and $S_{o,r}$).

This paper presents Magnetic Resonance Images (MRI) and non-spatially resolved (global) ^{1}H NMR spectra from selected saturation stages. Global DOC distributions are presented for endpoint saturations. Most importantly, the trajectory of the injection front have been investigated with spatially resolved DOC distributions at 0.4 pore volumes injected for both oil drives and both water drives.

2.4. NMR

All NMR acquisitions were recorded on a Bruker Biospin 500 WB Ultrashield spectrometer. Solid state ^{1}H NMR spectra were recorded with Magic Angle Spinning (MAS) using a solid-state probe head for 4 mm MAS rotors. All other NMR acquisitions were recorded using a commercial micWB40 micro imaging probe.

2.4.1. Magnetic resonance imaging (MRI)

All magnetic resonance images were recorded using a spin-echo acquisition (Rapid Acquisition with Relaxation Enhancement sequence with RARE factor = 1). The echo time was 2.9 ms, the field of view was 45 mm and the resolution was 128 by 128. The slice thickness was 1 mm and the repetition time was 1 s to ensure T_1 weighting.

2.4.2. The dimension of confinement (DOC)

Values for the magnetic susceptibility induced internal gradient term (G_0^2D) were recorded using a modified CPMG sequence [12,20] where the number (n) of π-pulses, over a constant decoding time T (50 ms), is varied from 32 to 1 in 32 steps. The decoding time T was set to 50 ms to completely cover the signal decay from both the water and the oil. Varying the number of π-pulses over a constant time interval leads to a variation in the time (τ') between the π-pulses and thus the echo time (T_E). The echo time is given by $T_E = 2\tau' + L_\pi$, where L_π is the pulse length of the π-pulse. Note that this means that the minimum echo time (at $n = 32$) is above 1 ms, which may eliminate signal with short T_2. The length of the hard $\frac{\pi}{2}$ and π pulses were calibrated to be 44 and 88 μs respectively.

This study presents global (averaged over the entire sample) and spatially resolved data. The recording of both the global and the spatially resolved values of the G_0^2D term was performed using both the regular and the spatially resolved version of a recently published pulse sequence [20]. In the spatially resolved version, the slice selective π pulse is a 3 lobe sinc pulse with bandwidth = 6300 Hz, pulse length = 719 μs and pulse power = 4.9 W. Along with a gradient strength = $1.4797 * 10^{-4}$ T m^{-1}, these parameters ensures a slice thickness of 1 mm. The slice positioning was set by keeping the Z-gradient constant and varying the center frequency of the slice selective π-pulse.

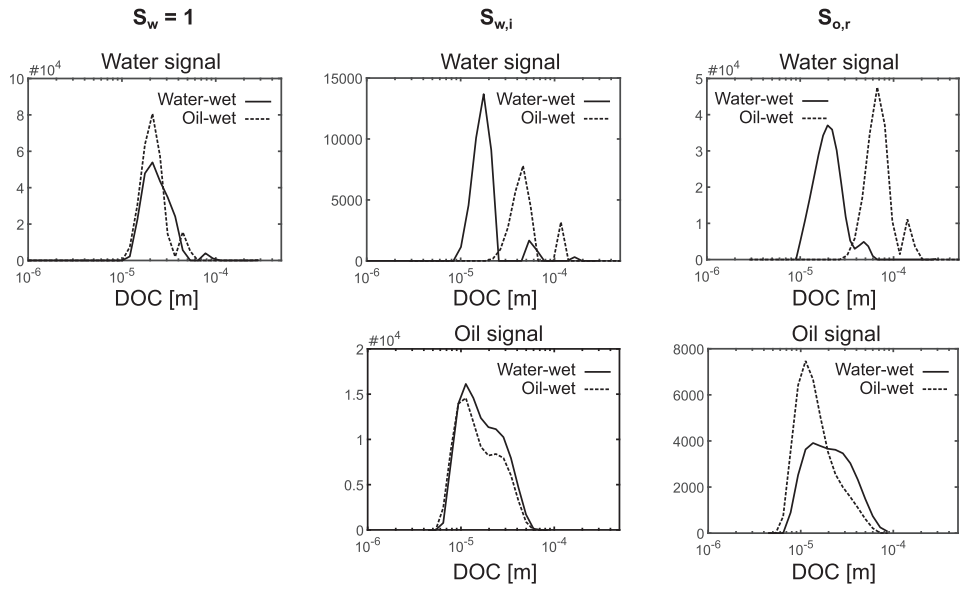

Fig. 5. Fluid specific inter sample comparisons of global DOC distributions at endpoint saturations.

In both the global and the spatially resolved case, the output of this sequence is a series of 32 spectra where the intensity is weighted with respect to G_0 and D. In general, this can be expressed as

$$I(\tau') = \int P(b) e^{-bn\tau'^k} db. \quad (4)$$

The analytical form of b and the value of k depends on the motional regime of the system. CPMG experiments performed with varying echo spacing, followed by the analysis suggested by Mitchell et al. [15,25], showed that the system is in between the Free Diffusion (FD) ($k = 3$) and the Localization (LOC) ($k = 1$) regimes, both for the water and oil signals. However, previous results on well characterized systems of glass beads [20] have shown that reliable values for G_0 and pore size distributions are obtained when the FD regime is assumed. In the analysis of the data we therefore assume that the system is in the FD regime, where the signal from a fluid decays according to Eq. 4 with $b = (\frac{1}{12})D\gamma^2 G_0^2$ and $k = 3$.

Fluid specific G_0 distributions were calculated from the $P(b)$ distributions and the diffusion coefficients for water and oil ($D_{H_2O} = 2.3 \cdot 10^{-5}$ cm^2 s^{-1} and $D_{Oil} = 4.5 \cdot 10^{-7}$ cm^2 s^{-1}). Diffusion coefficients were measured for both fluids at ambient temperature. DOC distributions were created with Eq. 3 where Δv was determined from the peaks in the obtained spectra.

3. Results and discussion

In the global experiments the saturation stages are visualized through MR images and ^{1}H NMR spectra. The global water and

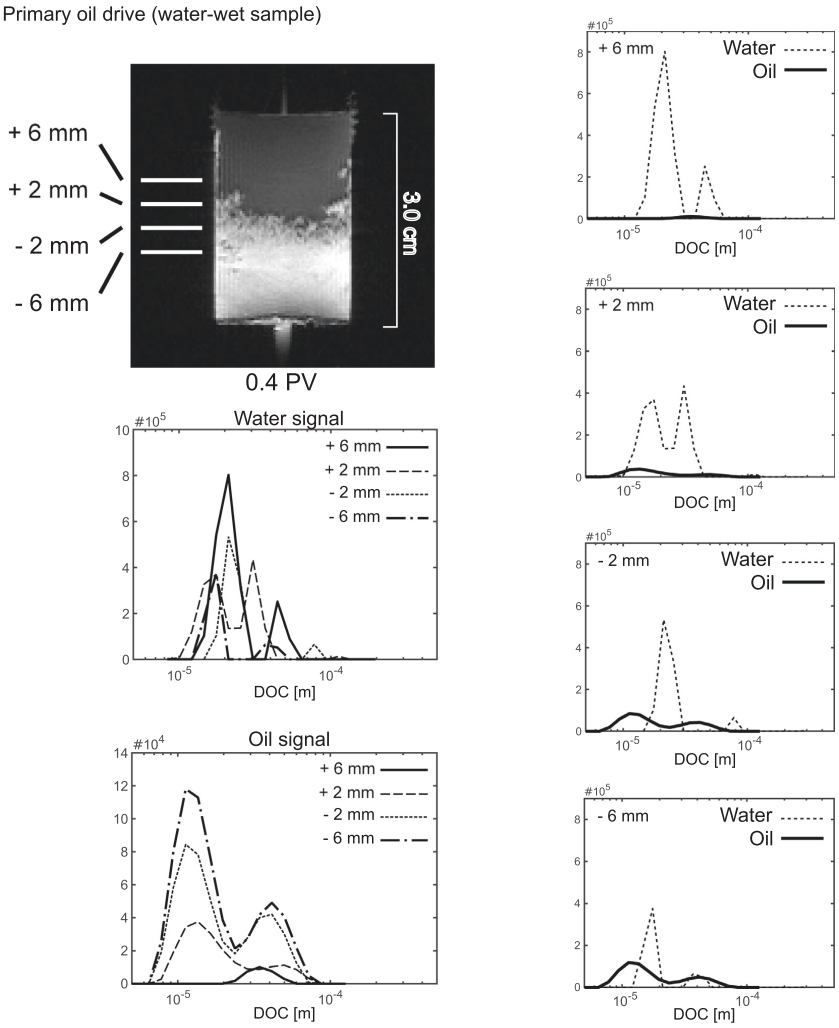

Fig. 6. Spatially resolved and fluid specific DOC distributions acquired in four different slices, positioned around the displacement front, after 0.4 pore volumes of oil has entered the water-wet sample during the primary oil drive.

oil dimensions of confinement provide information about how the fluids are distributed in the pore network across the entire sample at endpoint saturations ($S_w = 1, S_{w,i}$ and $S_{o,r}$).

In the spatially resolved experiments, acquisitions were made in four slices positioned around the displacing front after injection of 0.4 pore volumes of the displacing fluid. The spatially resolved water and oil dimensions of confinement therefore show how the displacing fluid enters the pore network and how it influences the geometry of the displaced fluid.

In a previous study [20] we used correlations between distributions of $\Delta\chi$ and G_0, where both dimensions scale with the distribution of pore sizes, according to Eq. (1). In the current study the determination of the distribution of DOC is based on correlations between an average value of v and a distribution of G_0, according to Eq. (3). All values in the distribution of G_0 is thus correlated with a single average value of v, where each specific DOC contribute with a signal with a characteristic line width. This can potentially lead to errors in the estimation of the distributions of DOC, compared to the results obtained in [20]. However, in order to separate signals from water and oil based on chemical shift differences, this is unavoidable. Furthermore, water have a higher diffusion coefficient than oil. Therefore, the spectral line-broadening will be averaged due to water motion over the DOC, but for oil a local value for the line-broadening will be obtained from a specific part of a specific DOC. This could potentially also have an additional impact on the determination of the DOC for oil.

3.1. Global dimension of confinement

The MR images shown in Fig. 3A show that, during the oil drive, the oil moves through the cell with a well defined front. These images are T_1-weighted and thus the most intense signal origi-

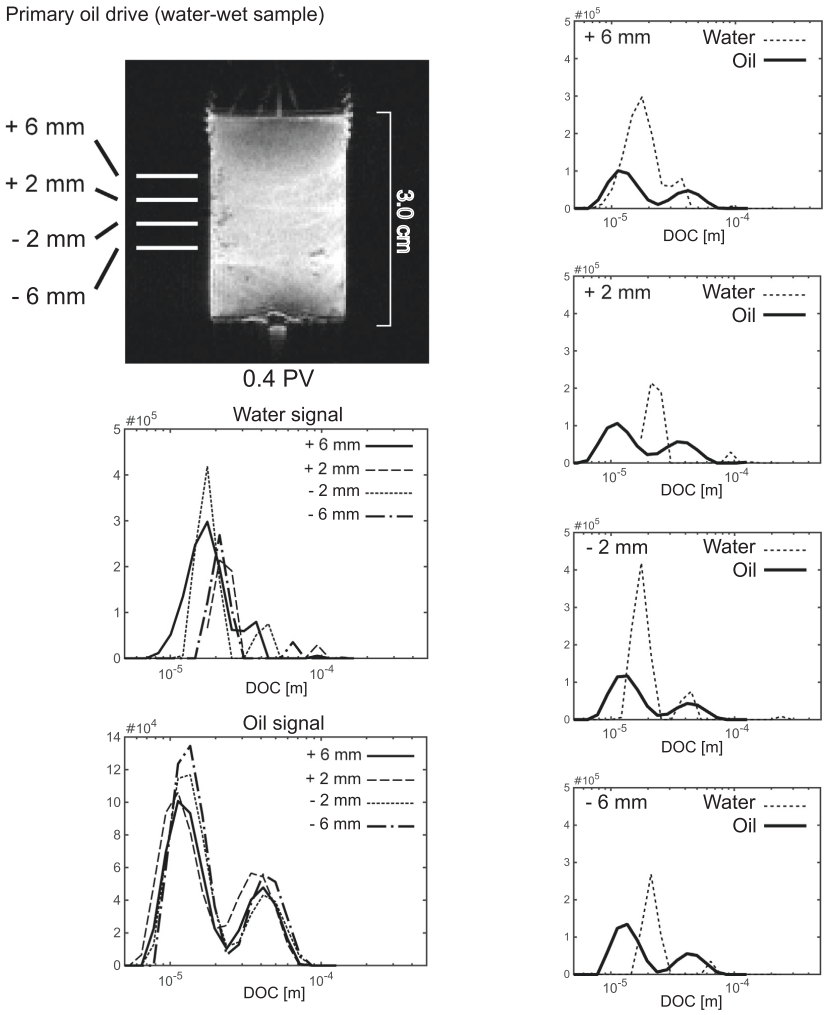

Fig. 7. Spatially resolved and fluid specific DOC distributions acquired in four different slices, positioned around the displacement front, after 0.4 pore volumes of water has entered the water-wet sample during the primary water drive.

nates from the oil ($T_1 \approx 0.5s$) and the least intense signal originates from the water ($T_1 \approx 3.0s$). The associated global ^{1}H NMR spectra show that the oil replaces the displaced water in a 1:1 ratio suggesting that the cell operates as intended, with no leakage. The primary water drive is harder to follow in the MR images as there is little or no fingering effects. However, the ^{1}H NMR spectra show that the oil is being displaced and that the residual oil saturation in the water wet sample is approximately 25%.

Fig. 3B shows the dimension of confinement for oil and water at the endpoint saturations in the water-wet sample. Note that the DOC distribution for water at $S_{w,i}$ ranges from approximately 10 to 100 μm, which is a reasonable interval for a pore size distribution in this sand. At $S_{w,i}$, the water only exerts a low DOC which corresponds to fluid close to the surface or in the smallest pores, which is expected in water wet samples. At residual oil saturation ($S_{o,r}$), the water has regained some of the larger pores, but not the largest, which is also as expected for the wetting fluid.

The DOC distributions for the oil show a corresponding behaviour, since being the non wetting fluid in the water-wet sample, it is forced out of a large portion of the smallest pores when moving from $S_{w,i}$ to $S_{o,r}$.

Fig. 4A shows the MR images and the corresponding global ^{1}H NMR spectra from all saturation stages in the oil-wet sample. It is apparent, from both the MR images and the ^{1}H NMR spectra, that the oil drive has a more efficient sweep than the oil drive in the WW sample (Fig. 3A). This is expected as, during the oil drive in the OW sample, the oil has surface contact and thus encompasses the water phase. In the WW sample the oil will flow through the middle of the pore, thus circumventing surface water and water in small pores.

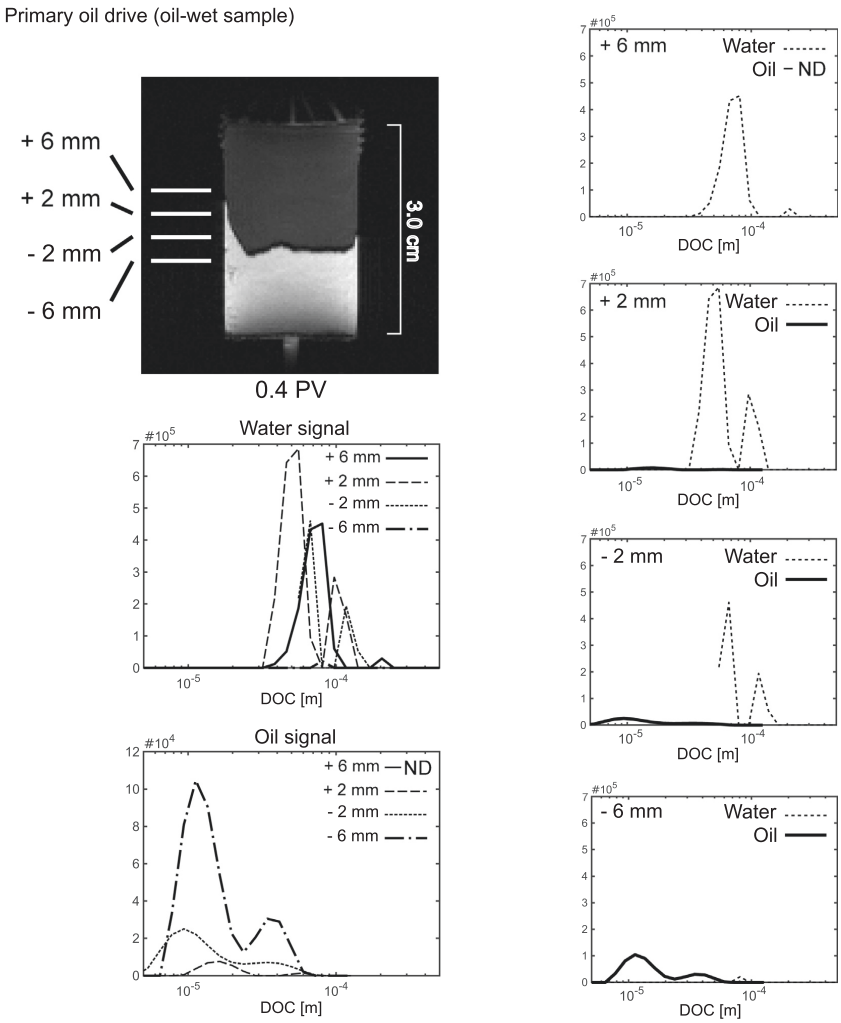

Fig. 8. Spatially resolved and fluid specific DOC distributions acquired in four different slices, positioned around the displacement front, after 0.4 pore volumes of oil has entered the oil-wet sample during the primary oil drive.

The MR images from the water drive (Fig. 4A) show a fingering effect as the non-wetting water moves through the sand. This is expected in the OW sample and so is the higher residual oil saturation seen in the ^{1}H NMR spectra from the OW sample compared to $S_{o,r}$ in the WW sample.

The DOC distributions from the endpoints, during the displacement experiments in the OW sample, are shown in Fig. 4B. The DOC distribution from water at $S_w = 1$ is comparable to the one seen for the WW sample (Fig. 3B). At $S_{w,i}$ however, all the remaining water is located in large pores and areas with no surface interactions. This is completely opposite from the same conditions in the WW sample and also as expected. At $S_{o,r}$ the water has moved through the largest pores, circumventing most of the oil in the small pores. This is also evident from the DOC distribution for the oil signal as most of the displaced oil, from $S_{w,i}$ to $S_{o,r}$, is displaced from the larger pores.

Fig. 5 shows the inter sample comparison of the DOC distributions at all the endpoints. The difference in wettability is especially apparent from the water signal. The water signal from the OW sample consistently originates from large pores and areas with no surface interactions. The oil signal has a consistently higher fraction of oil in surface areas and small pores in the OW sample compared to the WW sample. This is especially apparent at $S_{o,r}$ and these results agree with interpretations of T_2 relaxation measurements in sandstones with varying wettability performed by Freedman et al. [26].

3.2. Spatially resolved dimension of confinement

In this section we observe results from four slices positioned around the displacement front (+6 mm, +2 mm, −2 mm and −6 mm with respect to the iso center of the micro imaging probe). The data show which part of the pore network the displacing fluid

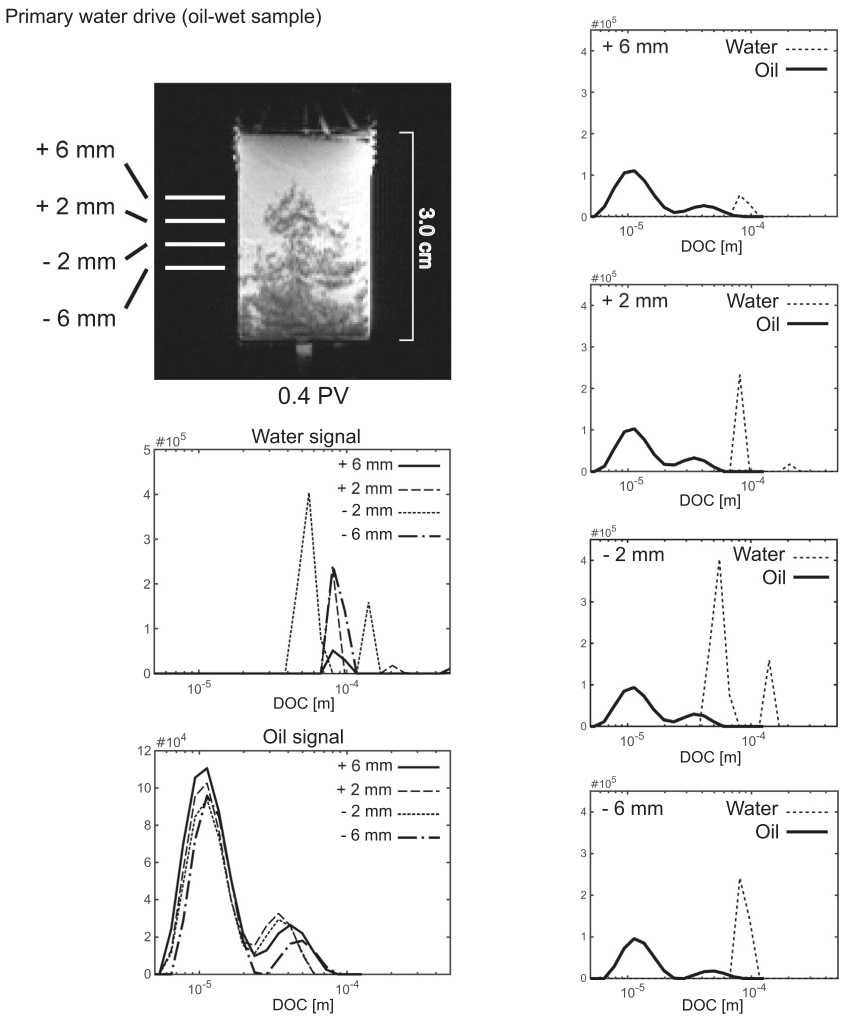

Fig. 9. Spatially resolved and fluid specific DOC distributions acquired in four different slices, positioned around the displacement front, after 0.4 pore volumes of water has entered the oil-wet sample during the primary water drive.

initially enters, and whether or not the local saturation changes as more displacing fluid is added. The top slices are positioned in an area that have barely been affected by the displacing fluid, while the bottom slices are positioned in areas that are clearly effected.

Fig. 6 shows the DOC distributions from water and oil signals around the oil front during the oil drive in the WW sample after 0.4 pore volumes injected. The oil first enters the largest pores. This is expected and can be observed in the oil DOC distributions from the slice located at +6 mm. When observing the results from the other slices it is apparent that as more oil enters, the water is forced into surface areas and small pores (slice located at −6 mm). This is expected as water is the wetting phase.

The results from the water drive in the WW sample are shown in Fig. 7. There are only minor changes in the DOC distributions as one moves down the slices. The reason is probably that the water has moved further through the sample after 0.4 pore volumes in the water drive than the oil had moved after 0.4 pore volumes during the oil drive. All four slices are therefore similarly affected by the displacement of oil by water.

As the oil enters the OW sample, during the oil drive, it initially occupies surface areas and the small pores. This is evident from the slice located at +2 mm in Fig. 8. In the bottom slice the oil has nearly completely displaced the water and the oil DOC distribution has a larger fraction of oil in surface areas and small pores than the oil DOC distribution for the same conditions in the WW sample. The remaining water is located in large pores and in areas without surface access.

It is apparent from Fig. 9 that during the water drive in the OW sample, the water displaces exclusively oil located in large pores. The water DOC distributions from all four slices are concentrated in the area representing large pores. The oil DOC distributions show little change as one observes all slices. However the fraction of oil in surface areas and small pores is larger in the OW sample during the water drive compared to the same situation in the WW sample (Fig. 7).

4. Conclusions

By investigating the dimension of confinement for oil and water during displacement experiments one can successfully determine the wettability of quartz sand sandstone models using high magnetic field strengths.

This method is based on G_0^2D weighted signal decay, recorded with a modified CPMG pulse sequence, which occurs faster than both T_1 and T_2 weighted signal decay. The acquisition itself is therefore relatively fast. Using correlations between dephasing in internal gradients (G_0^2D) and spectral linewidth ($\Delta\nu$) allow us to calculate a dimension of confinement (DOC) for oil and water in porous media as opposed to interpreting fluid distribution indirectly (i.e. through relaxation time distributions). The method is suitable for global, as well as spatially resolved investigations.

The data from global experiments provide fluid specific DOC distributions for oil and water at endpoint saturations ($S_w = 1, S_{w,i}$ and $S_{o,r}$). The spatially resolved data show which pores are initially occupied by the displacing fluids. The combined data from the global and the spatially resolved experiments provide a reliable wetting indication. However, both global and spatially resolved data determines the wetting state to a satisfactory degree as separate methods.

Declaration of Competing Interest

The authors declare that they have no known competing financial interests or personal relationships that could have appeared to influence the work reported in this paper.

Acknowledgements

The authors acknowledge The Research Council of Norway for support through the Norwegian NMR Platform, NNP (226244/F50) and Equinor ASA for funding the project "Wetting in porous media" through AKADEMIA.

References

[1] E. Amott, Observations relating to the wettability of porous rock, Petrol. Trans. AIME 216 (1959) 156–162.
[2] W.G. Anderson, Wettability literature survey - part1: rock/oil/brine interactions and the effects of core handling on wettability, J. Petrol. Technol. (1986) 1125–1144.
[3] W.G. Anderson, Wettability literature survey - part2: wettability measurement, J. Petrol. Technol. (1986) 1246–1262.
[4] W. Looyestijn, J. Hofman, Wettability-index determination by nuvlear magnetic resonance, Soc. Petrol. Eng. (2006) 146–153.
[5] E.C. Donaldson, R.D. Thomas, P.B. Lorenz, Wettability determination and its effect on recovery efficiency, Soc. Petrol. Eng. J. (1969) 13–20.
[6] R.J.S. Brown, I. Fatt, Measurements of fractional wettability of oil fields' rocks by the nuclear magnetic relaxation method, Soc. Petrol. Eng. (1956) 1–4.
[7] J. Mitchell, T.C. Chandrasekera, D.J. Holland, L.F. Gladden, E.J. Fordham, Magnetic resonance imaging in laboratory petrophysical core analysis, Phys. Rep. 526 (2013) 165–225.
[8] J. Wang, L. Xiao, G. Liao, Y. Zhang, L. Guo, C.H. Arns, Z. Sun, Theoretical investigation of heterogeneous wettability in porous media using nmr, Sci. Rep. 8 (2018) 13450.
[9] C. Liang, L. Xiao, C. Zhou, Y. Zhang, G. Liao, Z. Jia, Two-dimensional nuclear magnetic resonance method for wettability determination of tight sand, Magn. Reson. Imaging 56 (2019) 144–150.
[10] C. Liang, L. Xiao, C. Zhou, H. Wang, F. Hu, G. Liao, Z. Jia, Wettability characterization of low-permeability reservoirs using nuclear magnetic resonance: an experimental study, J. Petrol. Sci. Eng. 178 (2019) 121–132.
[11] M.D. Hürlimann, Effective gradients in porous media due to susceptibility differences, J. Magn. Reson. 131 (2) (1998) 232–240.
[12] B. Sun, K.J. Dunn, Probing the internal field gradients of porous media, Phys. Rev. E 65 (2002) 1–7.
[13] J. Mitchell, T.C. Chandrasekera, L.F. Gladden, Nuclear magnetic resonance relaxation and diffusion in the presence of internal gradients: the effect of magnetic field strength, Phys. Rev. E 81 (2010) 026101.
[14] J. Mitchell, T.C. Chandrasekera, L.F. Gladden, Obtaining true transverse relaxation time distributions in high-field nmr measurements of saturated porous media: removing the influence of internal gradients, J. Chem. Phys. 132 (2010) 244705.
[15] J. Mitchell, T.C. Chandrasekera, Understanding generalized inversions of nuclear magnetic resonance transverse relaxation time in porous media, J. Chem. Phys. 141 (2014) 224201.
[16] Y. Zhang, B. Blümich, $g_{int}^2 d - t_2$ correlation nmr of porous media, J. Magn. Reson. 252 (2015) 176–186.
[17] J. Mitchell, Rapid measurements of heterogeneity in sandstones using low-field nuclear magnetic resonance, J. Magn. Reson. 240 (2014) 52–60.
[18] Q. Chen, A.E. Marble, B.G. Colpitts, B.J. Balcom, The internal magnetic field distribution, and single exponential magnetic resonance free induction decay, in rocks, J. Magn. Reson. 175 (2) (2005) 300–308.
[19] R.T. Lewis, J.G. Seland, Characterization of pore geometry using correlations between magnetic field and internal gradient, Micropor. Mesopor. Mater. 269 (2018) 31–34.
[20] H.N. Sørgård, J.G. Seland, Investigating pore geometry in heterogeneous porous samples using spatially resolved $g_0 - \delta\chi_{app}$ and $g_0 - \delta\nu$ correlations, J. Magn. Reson. 301 (2019) 40–48.
[21] G.H. Sørland, H.W. Anthonsen, J.G. Seland, F. Antonsen, H.C. Widerøe, J. Krane, Exploring the separate nmr responses from crude oil and water in rock cores, Appl. Magn. Reson. 26 (2004) 417–425.
[22] H.N. Sørgård, C. Totland, W. Nerdal, J.G. Seland, Crude oil adsorbates on calcite and quartz surfaces investigated by nmr spectroscopy, J. Phys. Chem. (2017) 20892–20899.
[23] B.K. Hunter, L.W. Reeves, Chemical shifts for compounds of the group iv elements silicon[1] and tin[2], Can. J. Chem. 46 (1968) 1399–1414.
[24] N.R. Morrow, Wettability and its effect on oil recovery, J. Petrol. Technol. (1990) 1476–1484.
[25] J. Mitchell, T.C. Chandrasekera, L.F. Gladden, Measurement of the true transverse nuclear magnetic resonance relaxation in the presence of field gradients, J. Chem. Phys. 139 (2013) 074205.
[26] R. Freedman, N. Heaton, M. Flaum, G. Hirasaki, C. Flaum, M. Hurlimann, Wettability, saturation, and viscosity from nmr measurements, Soc. Petrol. Eng. 8 (2003) 317–327.

Graphic design: Communication Division, UiB / Print: Skipnes Kommunikasjon AS

uib.no

ISBN: 9788230846414 (print)
9788230848913 (PDF)